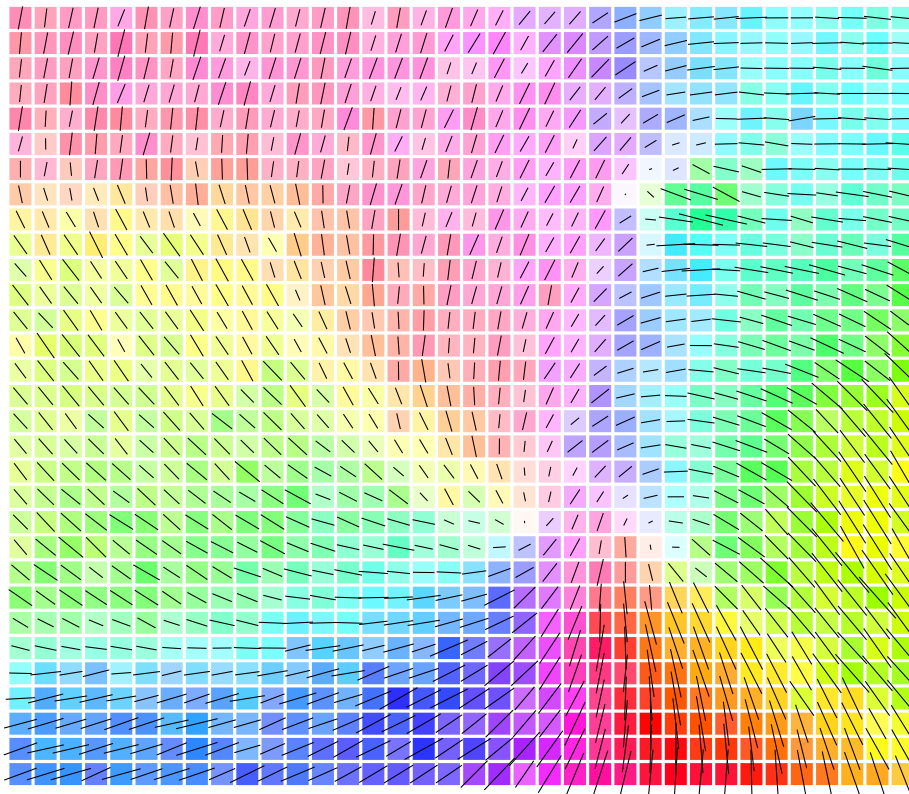# Digital image analysis of membrane domains measured with Fluorescence and Atomic Force Microscopy (AFM)

Master thesis

Henrik Skov Midtiby

Supervised by

Associate Professor Adam Cohen Simonsen, PhD

MEMPHYS – center for biomembrane physics
Department of Physics and Chemistry
University of Southern Denmark
March 2009

Digital image analysis of membrane domains measured with Fluorescence and Atomic Force Microscopy (AFM)

Master thesis

Henrik Skov Midtiby

Supervised by
Associate Professor Adam Cohen Simonsen, PhD

MEMPHYS – center for biomembrane physics
Department of Physics and Chemistry
University of Southern Denmark
March 2009

The illustration on the front page is a visualization of the observed fluorophore orientation in a gel domain. The color of each pixel is determined by the observed fluorophore orientation at that location. At each pixel a short black line indicates the fluorophore orientation. The image is $2\mu m$ wide. For more information see chapter 5.

Preface

This thesis covers the work done as part of my master education in physics and computer science at Memphys, University of Southern Denmark in the period spring 2008 – spring 2009.

The work have been done under the supervision of Associate Professor Adam Cohen Simonsen and in close collaboration with Uffe Bernchou and Jonathan Brewer who have helped with data acquisition and contributed with numerous image and ideas for how they could be analyzed.

I would like to thanks all the people at Memphys for practical help and technical discussions regarding my project. A special thank to John Hjort Ipsen and Per Lyngs Hansen for many interesting conversations.

I want to thank Linda Ahrenkiel, Philip Roland Jarnhus and Thorkild Skov Midtiby which have all helped me with numerous comments and proofreading.

Summary

We have investigated the membrane phase behavior of supported lipid bilayers. The domain formation during cooling of the bilayer were monitored with fluorescence microscopy. By equipping the fluorescence microscope with a linear polarization filter and acquiring several images of the sample with varying orientations of the linearly polarized light, the fluorophore anisotropy and orientation in a sample could be measured. This polarization fluorescence microscopy technique have been used to investigate how the two fluorophores Laurdan and DiI are aligned in fluid, gel and stripe domains. The random orientation of lipid molecules in fluid domains can be seen as very low values in the fluorophore anisotropy. The measured fluorophore anisotropy of gel and stripe domains indicates that the lipids in these domains are much more ordered. The examined gel domains are divided into several sub domains, where each sub domain have their fluorophore orientation. This division of gel domains is seen with both two and one photon microscopy and is visualized in figure 1 which is based on two photon microscopy. Investigations of the variations in fluorescence intensity as the polarization orientation is changed reveals that the distribution of orientation of the fluorophores cannot be wider
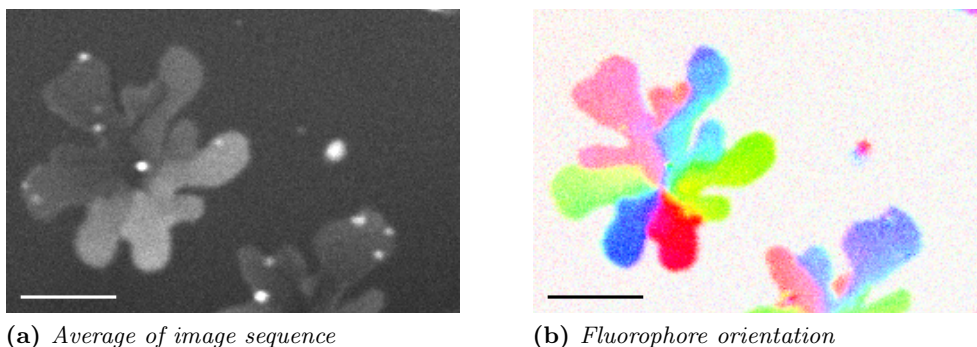
(a) *Average of image sequence*

(b) *Fluorophore orientation*

Figure 1: *Fluorophore orientation in gel domains visualized with two photon polarization fluorescence microscopy. The bilayer were composed of an equimolar mixture of DOPC and DPPC and were stained with Laurdan. $5\mu m$ scale bars.*

(a) *Average of image sequence*
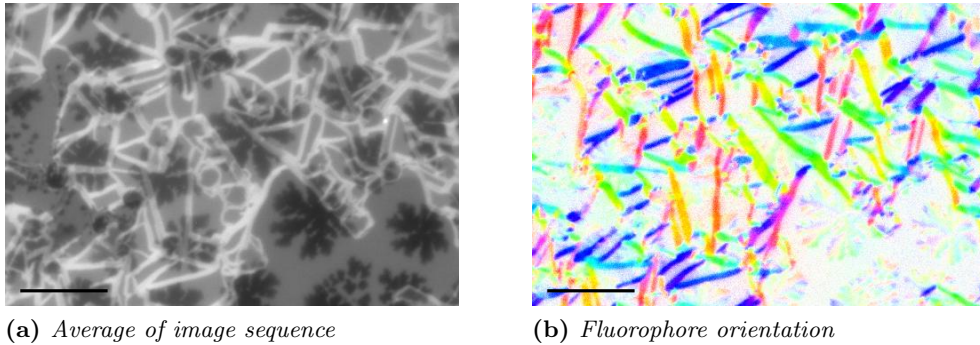

(b) *Fluorophore orientation*

Figure 2: *Fluorophore orientation in stripe domains visualized with one photon polarization fluorescence microscopy. Bilayer composed of an equimolar mixture of DPPC and POPC and stained with DiI. 20μm scale bars.*

than a normal distribution with standard deviation of $\sigma \sim 30°$.

The investigation of how DiI is aligned in stripe domains revealed that the fluorophore will be parallel with the stripe domains. This is visualized in figure 2. The study of fluorophore alignment in stripe domains revealed some systematic errors in the calculated fluorophore orientations. The source of the problems were determined to be the birefringent properties of mica, a material commonly used as support for supported lipid bilayers. With this knowledge it was possible to remove some of the observed errors.

Sammenfatning

Vi har undersøgt hvordan supporterede lipid dobbelt lag udviser fase overgange. Fluorescens mikroskopi er blevet benyttet til at optage billeder af domæne dannelse under nedkøling af lipid dobbelt laget. Ved at udstyre fluorescens mikroskopet med et linært polariserings filter og derefter optage en serie af billeder hvor orienteringen af det polariserede lys er ændret i små skridt mellem hvert billede, er det muligt at bestemme anisotropi og den rumlige orientering af det benyttede farvestof i prøven. Denne teknik med polariseret fluorescens mikroskopi er anvendt til at undersøge hvordan de to farvestoffer Laurdan og DiI er ordnet i flydende, gel og stribe fase domæner. Den tilfældige orientering af lipid molekylerne i den flydende fase kan observeres som meget lave værdier i den målte farvestof anisotropi. Farvestof anisotropien i gel og stribe domæner er væsentligt højere, hvilket antyder at lipiderne i disse domæner er meget mere ordnede. De undersøgte gel domæner er opdelt i flere under domæner, hvor det enkelte under domæne har den sammen farvestof orientering. Denne opdeling af gel domæner er observeret vha. både et og to foton mikroskopi. I figur 3 er de beregnede farvestof orienteringer vist vha. en farve kodning; billedet er baseret på målinger i et to foton mikroskop. Analyser af hvordan den målte fluorescens intensitet afhænger af orienteringen af det polariserede lys viser at fordelingen af farvestof orienteringer ikke kan være bredere end en normal fordeling med standard afvigelse på $\sigma \sim 30°$.

Undersøgelsen af hvordan DiI er orienteret i stribe domæner viste at farvestoffet vil lægge sig parallelt med stribe domæner. Dette er vist i figur 4. Studiet af farvestof orienteringer i stribe domæner henledte opmærksomheden på nogle systematiske fejl i de bestemte farvestof orienteringer. Kilden til problemerne blev lokaliseret til de dobbeltbrydende egenskaber af mica, et materiale der ofte bliver benyttet til at lave understøttede dobbelt lipid lag. Med denne viden blev det muligt at fjerne nogle af de observerede fejl.
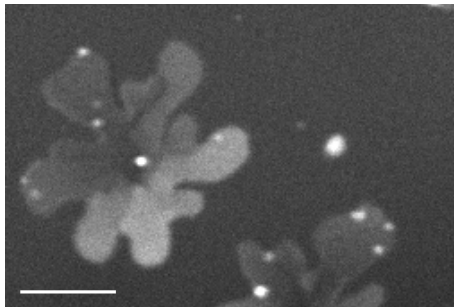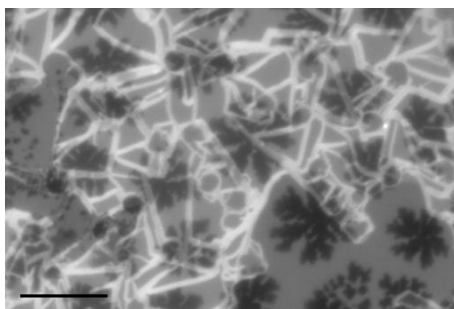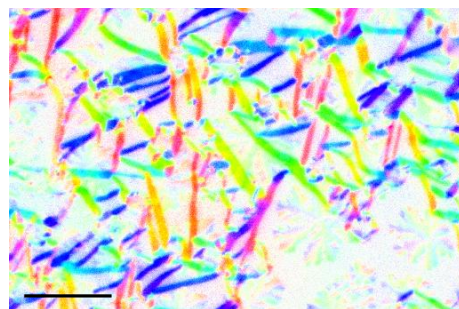
(a) *Gennemsnits intensitet af billed-sekvensen*
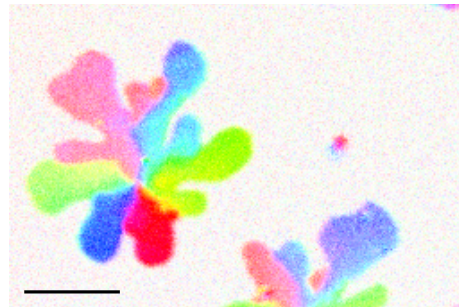
(b) *Farvestof orientering*

Figure 3: *Farvestof orientering i gel domæner visualiseret med to foton polariseret fluorescens mikroskopi. Det afbilledede lipid dobbeltlag består af en blanding af DOPC og DPPC i forholdet en til en og er farvet med Laurdan. 5µm skala linje.*

(a) *Gennemsnits intensitet af billedsekvens*

(b) *Farvestof orientering*

Figure 4: *Farvestof orientering i stribe domæner visualiseret med et foton polarisations fluorescens mikroskopi. Det afbilledede lipid dobbeltlag består af en blanding af DPPC og POPC i forholdet en til en og er farvet med DiI. 20µm skala linje.*

Abbreviations

Å   Ångstrom, $1\text{Å} = 10^{-10}m$, page 23

μL Micro liter. $1\mu L = 10^{-6}L$, page 14

Ω Fluorophore anisotropy, page 86

ϕ Azimuth angle. Angle between $\mathbf{E}$ and $\mathbf{p}$, page 52

ρ Tilt of acyl chains relative to $\mathbf{n}$., page 51

$\mathbf{E}$ Electrical field of excitation light, page 51

$\mathbf{n}$ Lipid bilayer normal., page 51

$\mathbf{p}$ Transition dipole, page 51

Θ Angle of incidence, page 33

a_h Area of head group, page 4

$I_n^{x,y}$ Pixel intensity at location x, y in the n'th image in an image sequence., page 57

l Length of acyl chains, page 4

N_s Surfactant parameter, page 4

nm Nanometer, $1nm = 10^{-9}m$, page 20

S_meas Measured sample shape, page 24

S_{esti} Estimated sample shape, page 24

S_{real} Real sample shape, page 24

T Tip shape, page 24

T_m Main transition temperature, page 5

v Hydrophobic volume, page 4

Abbreviations

F	Fluid phase, page 5
G	Gel phase, page 5
L_d	Liquid disordered, page 5
L_o	Liquid ordered, page 5
AFM	Atomic force microscopy, page 11
CCD	Charged coupled device, page 17
DiI	1.1'-dioctadecyl-3,3,3',3'–tetramethylindocarbocyanine, page 19
DLPC	1,2-dilauroyl-sn-glycero-3-phosphocholine, page 75
DMPC	Dimyristoylphosphatidylcholine, page 75
DMPE	1,2-dimyristoyl-sn-glycero-3-phosphoethanolamine, page 75
DOPC	1,2-dioleyl-sn-glycero-3-phosphocholine, page 51
DPPC	1,2-dipalmitoyl-sn-glycero-3-phosphocholine, page 6
DPPG	1,2-dipalmitoyl-sn-glycero-3-phosphoglycerol, page 21
DSC	Differential scanning calorimetry, page 6
DSC	Differential scanning calorimetry, page 11
DSPC	1,2-distearoyl-sn-glycero-3-phosphocholine, page 6
EDTA	ethylenediaminetetraacetic acid, page 28
FRAP	Fluorescence recovery after photobleaching, page 10
fs	Femtosecond. $1\text{fs} = 10^{-15}s$, page 17
GP	Generalized polarization, page 23
GUV	Giant unilammelar vesicle, page 11
HEPES	4-(2-hydroxyethyl)-1-piperazineethanesulfonic acid, page 28
Laurdan	6-lauroyl-2-dimethylaminopahthalene, page 21
MD	Molecular dynamics, page 77
mica	Muscovite mica, page 12
PC	Phosphocholine, page 3
PE	Phosphoethanolamine, page 3

PG   Phosphoglycerol, page 3

POPC   1-palmitoyl-2-oleoyl-sn-glycero-3-phosphocholine, page 3

POPG   1-palmitoyl-2-oleoyl-sn-glycero-3-phosphoglycerol, page 7

rpm   Rotations pr minute, page 14

SAXS   Small angle X-ray scattering, page 74

SAXS   Small angle x–ray scattering, page 11

SLB   Supported lipid bilayer, page 11

SNR   Signal to noise ratio, page 17

STM   Scanning Tunneling Microscopy, page 75

SUV   Small unilammelar vesicle, page 11

Contents

Chapter 1

Introduction

Lipids and lipid bilayers are an important ingredient in life. The boundary of cells, the plasma membrane, consists of a lipid bilayer. Since lipid bilayers are such a fundamental part of the life we know, the properties of lipid bilayers have been examined intensively in the recent years. Membranes formed by lipid bilayers are found in many locations inside an animal cell, see figure 1.1. The plasma membrane that defines what is inside or outside of the cell and the membranes around the organelles are all lipid bilayers. Biological membranes have many functions which includes: separation of the cell from the surroundings, facilitating transport of some molecules while hindering others to pass the membrane, building and maintenance of gradients over the membrane (pH, ions, . . .) which can be used for energy storage. The transport of molecules that cannot pass through the lipid bilayer are controlled by transport proteins embedded in the lipid bilayer.

In addition to the direct functions of lipid bilayers in the cell (compartmentalizing, controlling transportation over the membrane), the lipid bilayer structure have some properties that are needed in a rough environment. If a small hole is introduced in the lipid bilayer so that it effectively is punctured, the bilayer can "heal" itself and close the hole[3]. The ability to repair minor defects in the lipid bilayer, indicates that a lipid bilayer with no defects are an energetically favourable state of the bilayer and that it is self aggregating. Bangham and Horne confirmed this self aggregation of lipid bilayers when they studied how dried lipids reacted at exposure to water[4]. For understanding the self aggregation of the lipid bilayer lets take a closer look on the building blocks in the bilayer, the lipids.

1.1 Lipids

According to Wikipedia[5]: *lipids are broadly defined as any fat-soluble (lipophilic), naturally-occurring molecule.* Such a definition covers a large group of chemical compounds including the amphiphilic lipids that are found in the cellular

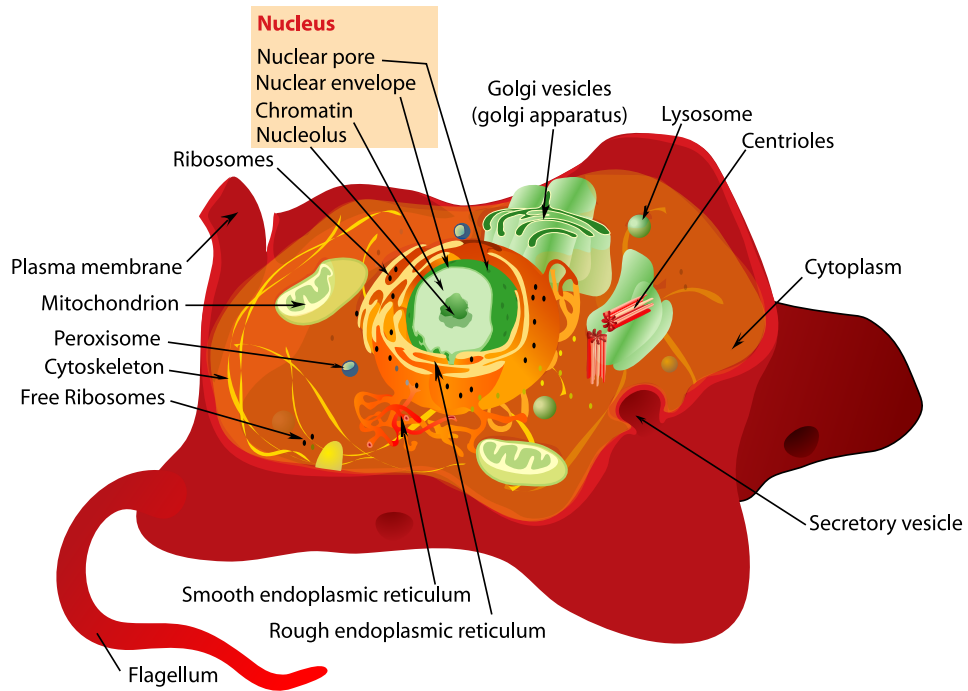**Figure 1.1:** *The structure of an animal cell. Image from Wikipedia [1].*

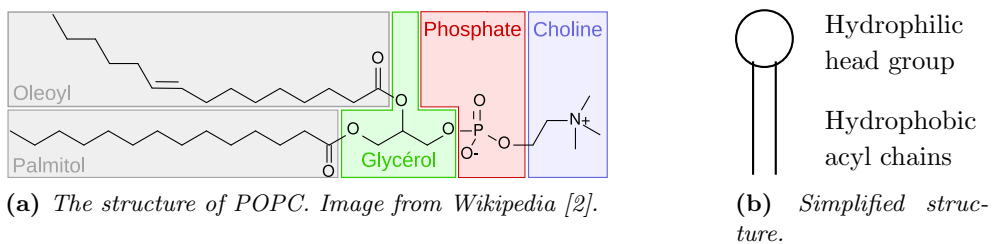**(a)** *The structure of POPC. Image from Wikipedia [2].*

(b) *Simplified structure.*

Figure 1.2: *The structure of a phospholipid and a schematic representation of a phospholipid.*

(a) *Phosphocholine (PC)* **(b)** *Phosphoethanolamine (PE)* **(c)** *Phosphoglycerol (PG)*
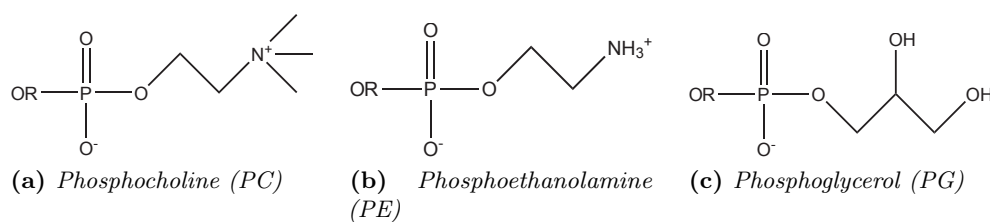
Figure 1.3: *Three different phospholipid head groups at physiological pH.*

membrane: phospholipids, glycolipids and sterols. Phospholipids belong to the group of triglycerides. A triglyceride molecule consists of a glycerol backbone linked to three acyl chains or other structures via ester bonds. In a phospholipid one of the three attached groups is a phosphate compound while the two remaining groups are acyl chains. Phospholipids represents 53% of the lipids in the plasma membrane of epidermal cells (skin) from humans[6]. 1-palmitoyl-2-oleoyl-sn-glycero-3-phosphocholine (POPC) is an example of a phospholipid, the molecular structure of POPC is shown in figure 1.2a. POPC consists of two fatty acids, Palmitic acid and Oleic acid, and a phosphocholine group attached to the glycerol backbone. The numbers 1, 2 and 3 in the name describes the location on the backbone where the functional groups are attached (palmitoyl in the first location, . . .). A schematic representation of phospholipids is shown in figure 1.2b, where the head group is shown by a circle and the two acyl chains by straight lines. The physical properties of a phospholipid depends on the two attached acyl chains and the head group. Instead of the common names for the fatty acids, the attached acyl chain can be described by the number of carbon atoms in the chain and the number of double bounds in the chain. Oleic acid that is based on a 18 carbon atom long acyl chain with one double bond will then be denoted $18:1^{\Delta 9}$, where the superscript describes that the location of the double bond is between the 9th and the 10th carbon atom counted from the carboxyl group. Palmitic acid are described by 16:0. The full structure of POPC can then be expressed as: 16:0, $18:1^{\Delta 9}$ PC.

The head group can either be zwitterionic or charged. Zwitterionic head groups have no net charge, but a separated positive and negative charge which induces a dipole moment. Phosphocholine (PC) and phosphoethanolamine (PE) are two zwitterionic head groups while phosphoglycerol (PG) is a negative charged (anionic) head group. The structure of the three head groups is shown in figure 1.3. The charged head group can easily form hydrogen bonds to nearby water molecules and is thus a hydrophilic group; the two acyl chains cannot form such hydrogen bonds and will therefore try to avoid contact with water molecules. Phospholipids contains both a hydrophilic head group and two hydrophobic acyl chains. Such a molecule with both hydrophilic and hydrophobic regions is called an amphiphilic molecule.

(a) Micelle

(b) Inverted micelle

(c) Lipid bilayer

(d) Vesicle
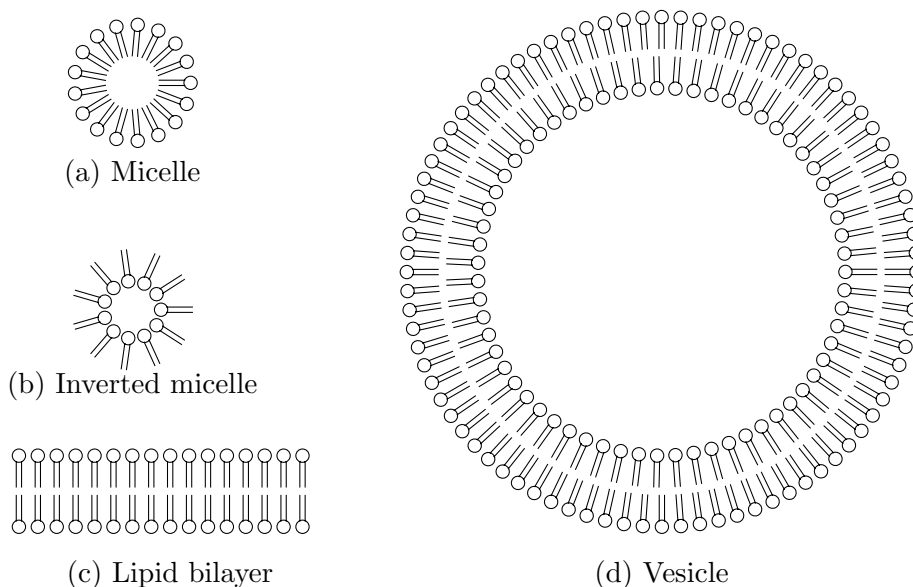
Figure 1.4: *How the hydrophobic or hydrophilic parts of amphiphilic molecules can avoid being in contact with the solvent.*

1.2 Self aggregation of lipids

It is not energetically favourable for amphiphilic molecules to be scattered randomly in an aqueous solution, as both the hydrophilic and hydrophobic regions will be exposed to the aqueous solution. For minimizing the free energy, the amphiphilic molecules will form suitable aggregates for avoiding direct contact between the hydrophobic regions and the aqueous solution. The shape of the formed aggregate depends on the surfactant parameter N_s of the amphiphilic molecules and the used solvent. N_s can be calculated from head group area a_h, acyl chain length l and hydrophobic volume v of the molecule using the formula[7]:

$$N_s = \frac{v}{la_h} \tag{1.1}$$

Four different types of such aggregates are shown in figure 1.4. If the head group is large compared to the acyl chains ($N_s < 1$), the amphiphilic molecules can form micelles. A micelle is an aggregate of amphiphilic molecules formed as a sphere, a cut through a micelle is shown in figure 1.4a. Inside the sphere there is an apolar region where the hydrophobic acyl chains are located and the surface of the sphere are formed by the hydrophilic head groups. This structure allows all the hydrophilic head groups to be in contact with an aqueous solvent, while all the hydrophobic acyl chains are shielded from the solvent. If the size of the head group and the acyl chains are comparable ($N_s \sim 1$) micelle

formation is no longer energetically favourable, as there is not sufficient space inside the micelle for all the acyl chains. For $N_s \sim 1$ the amphiphilic molecules will form a planar structure consisting of two lipid layers, this is the lipid bilayer which is shown in figure 1.4c. In a bilayer the amphiphilic molecules are ordered in two layers with the hydrophilic head groups oriented outwards. The acyl chains inside the bilayer forms a hydrophobic region, at the ends of the lipid bilayer, this hydrophobic region will be exposed to the aqueous solvent, for minimizing this energetically unfavourable state, the whole bilayer can bend such that the hydrophobic ends of the bilayer are connected and the whole bilayer forms a vesicle. The structure of a vesicle is shown in figure 1.4d.

A molecule that should go through a lipid bilayer, will have to pass two hydrophilic and one hydrophobic regions. As water soluble molecules are almost completely expelled from the hydrophobic region, it is very difficult for them to pass the lipid bilayer. Thus a lipid bilayer effectively works as a barrier for hydrophilic molecules.

1.3 Membrane phases

The organization of lipid molecules inside a lipid bilayer is if quite complex and depends on several factors. Attractive Van der Walls forces between the long acyl chains will try to straighten the acyl chains to obtain a closer packing of the lipid molecules. The lipid molecules are subject to thermal fluctuations with energies of order $k_B T$, these fluctuations will make the acyl chains crumble and let the lipids diffuse around between each other. Which type of force that dominates, thermal or Van der Walls, determines the general structure in the lipid bilayer.

At low temperatures, the attractive forces will dominate and the lipids will be arranged in a solid crystalline structure with ordered acyl chains, this is the socalled gel, G, phase. The close packed lipid structure in the G phase reduces the lipid mobility significantly. The thermal fluctuations will dominate at high temperatures, in this case the lipid molecules can float freely around, just like molecules in a fluid, this is the F phase. The fluid phase can be split in two distinct phases, the liquid ordered L_o and the liquid disordered L_d. In the L_o phase the lipids have ordered acyl chains whereas in the L_d phase the acyl chains are disordered[8]. The L_o phase are stabilized by cholesterol. The change from ordered to disordered acyl chains when a lipid bilayer leaves the G phase and enters the F phase can change the acyl chain length, l.

When the temperature of a lipid bilayer in the G phase is raised, the thermal fluctuations will increase. At a certain temperature, the main transition temperature (T_m), the thermal fluctuations of the lipid molecules will be large enough to break the ordered structure in the G phase. This is the main transition. The transition from the G phase to the F phase involves conformational changes in the lipid packing (the ordered structure is lost) and

(a) *DSC thermogram of a DPPC bilayer, image from Mouritsen [9].*

(b) *How the pre and main transition temperatures depend on acyl chain length. From Wack et. al [10]*
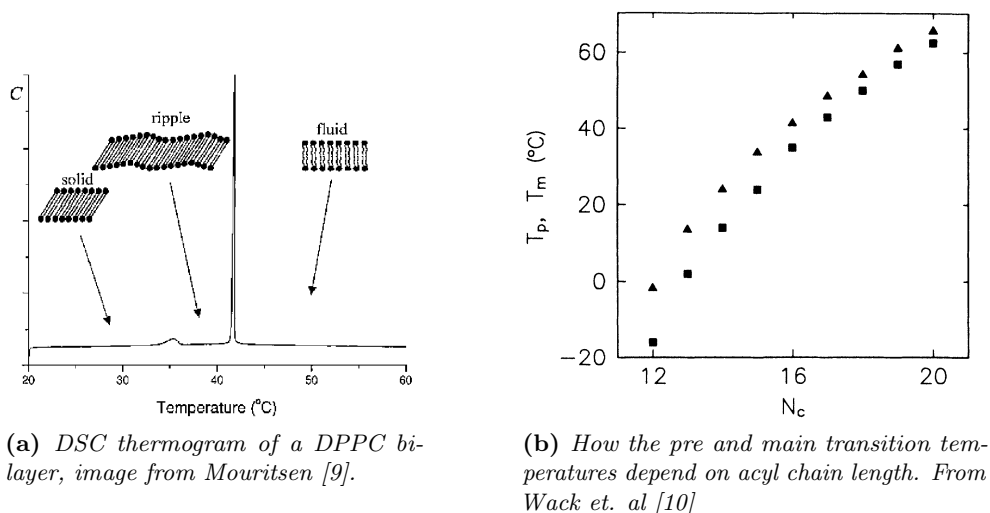
Figure 1.5: *Phase behavior analyzed with DSC and how the main phase transition temperature is related to the acyl chain length.*

the melting of the acyl chains. These conformational changes increases the entropy of the system and such changes requires energy. The main transition temperature of a lipid bilayer can be determined by measuring the energy required for the conformational changes.

Differential scanning calorimetry (DSC) is a method that can measure the heat capacity of a sample as a function of the temperature. The heat capacity is the energy required for increasing the temperature by one Kelvin. A DSC scan of bilayers of 1,2-dipalmitoyl-sn-glycero-3-phosphocholine (DPPC) is shown on figure 1.5a. The two peaks in the thermogram near $36°C$ and $42°C$ corresponds to phase transitions in the lipid bilayer. The large peak at $42°C$ are caused by the acyl chain melting at the main transition and the much smaller peak at $36°C$ is the pretransition. At temperatures between the pre and main transitions, the lipid bilayer will be in the ripple R phase. The ripple phase is characterized by periodic undulations, ripples, in the bilayer height[9]. The area below a peak in the DSC thermogram, the enthalpy, is a measure of how much energy the conformational changes required. The enthalpy of the main transition is $6.43kcal/mol$ and only $0.92kcal/mol$ for the pretransition[11]. The pretransition is not observed for all lipids, it is present in phosphatidylcholines but absent in phosphatidylethanolamines.

Larger acyl chains induces stronger attractive forces between the lipid molecules. In figure 1.5b temperatures for the pre and main transitions are plotted as a function of acyl chain length for lipids with two identical and saturated acyl chains. Lipids with longer acyl chains have higher phase transition temperatures. Unsaturated acyl chains have one or more double
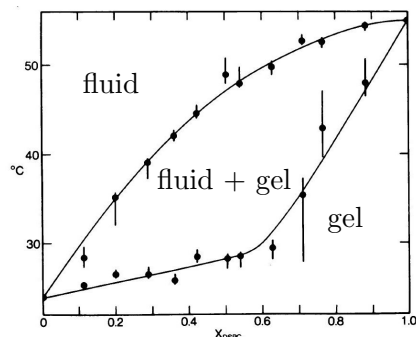
(a) *Phase diagram for DMPC / DSPC mixtures, image from [13].*
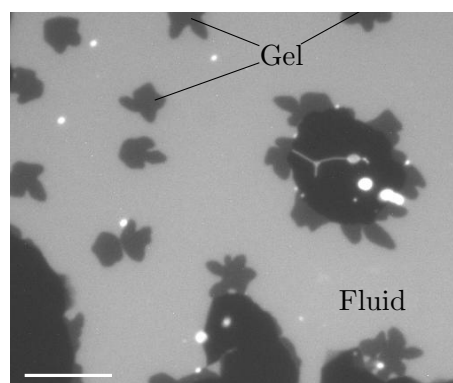
(b) *POPG / DPPC 7:3. Scale bar is $20\mu m$.*

Figure 1.6: *Phase behavior of binary lipid mixtures can be described by a phase diagram. The phase diagram tell us in which phase a system at a given temperature and with a known lipid composition will be.*

bonds which induces kinks in the acyl chains. Acyl chains with such kinks cannot pack as tight as saturated acyl chains. The loose packing between unsaturated acyl chains reduces the attractive Van der Walls interactions which again causes the phase transition temperatures to decrease significant. The phosphocholine with two 18 carbon long saturated acyl chains is 1,2-distearoyl-sn-glycero-3-phosphocholine (DSPC) which have a main transition temperature at $58°C$. The similar lipid with one double bond in the acyl chains is 1,2-dioleoyl-sn-glycero-3-phosphocholine (DOPC) which main transition temperature is $-22°C$[12].

Binary mixtures Lipid bilayers composed of a mixture of two or more lipid types have similar membrane phases. If two lipids with different main transition temperatures T_m^{low} and T_m^{high} are used to form a lipid bilayer, the whole bilayer will be in a fluid phase for temperatures above T_m^{high} and in a gel phase for temperatures below T_m^{low}. In the temperature range between T_m^{low} and T_m^{high} the mixture can be in the gel phase, fluid phase and in a phase with coexisting gel and fluid domains, which state that is observed depends on the molar fraction of the lipids and the sample temperature. By plotting the observed phase transition temperatures as a function of the molar fraction of the high temperature melting lipid, a phase diagram can be constructed. An excellent introduction to phase diagrams is given by Heimburg [14]. In figure 1.6a the phase diagram of a binary mixture of DMPC and DSPC is shown. For a given temperature T the binary lipid mixture will settle in one of three states (gel, fluid and coexisting) depending on the lipid mixture. In figure 1.6b, a lipid bilayer with coexisting fluid and gel domains are shown. The lipid mixture
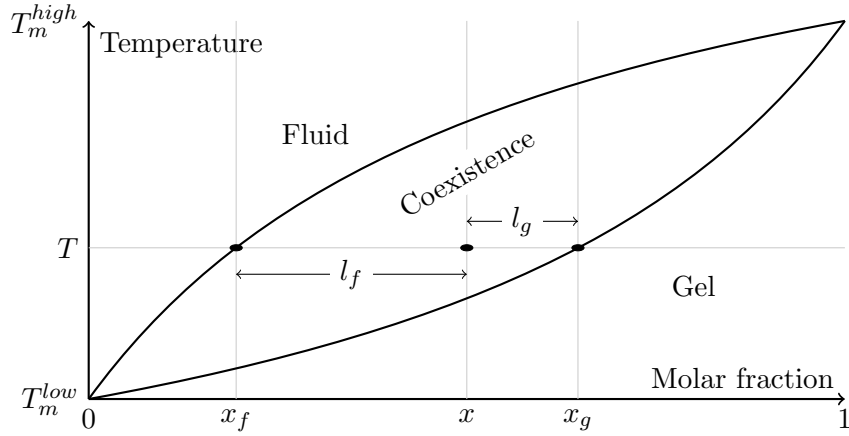
Figure 1.7: *How a binary lipid mixture with molar fraction x is divided into two coexisting phases is described the lever rule.*

in the bilayer consists of 1-palmitoyl-2-oleoyl-sn-glycero-3-phosphoglycerol (POPG) and DPPC.

The black regions are holes in the lipid bilayer, the dark gray regions are gel domains and the bright gray regions are fluid domains. We will now consider the case with coexisting fluid and gel domains. The lipid composition in the gel and fluid domains is determined by the phase boundaries between the fluid / coexistence phases and the coexistence / gel phases. The molar fraction of the high melting lipid inside fluid domains, x_f, is determined by the intersection of the temperature line and the fluid / coexistence phase boundaries in figure 1.7. If the molar fraction of the high melting lipid is increased the fluid phase will not be stable and gel domains with higher molar fractions will form. For gel domains the similar molar fraction x_g is determined by the temperature and the gel / coexistence phase boundaries. Let a denote the lipid fraction found in fluid domains, the remaining part of the lipids $(1 - a)$ will then be in gel domains. The average molar fraction x will then be a weighted average of these two values

$$x = ax_f + (1 - a)x_g \tag{1.2}$$

if x, the temperature and thus x_f and x_g are known, the fraction of the lipid molecules that will be in the fluid phase can de determined by

$$a = \frac{x_g - x}{x_g - x_f} = \frac{l_g}{l_f + l_g} \tag{1.3}$$

$$1 - a = \frac{l_f}{l_f + l_g} \tag{1.4}$$

Where $l_f = x - x_f$ and $l_g = x_g - x$. These two expressions for the lipid fraction in fluid and gel domains are known as the *lever* rule.

1.4   Membrane phases in biological systems

The physical properties of a lipid bilayer membrane is closely related to the membrane phase. Having a fluid membrane is essential for absorption of vesicles, lateral diffusion of lipids and proteins for ensuring an even distribution and finally cell division. A close packed lipid organization in a G membrane phase will effectively reduce all transport of molecules through the lipid bilayer compared to the more open structure in a F pase. The permeability of glucose in lipid bilayers composed of DMPC / DPPC 1:1 were examined by Clerc *et. al* [15]. They captured radioactive marked glucose molecules inside vesicles and measured how fast the radioactive material leaked from the vesicles. For lipid bilayers in the G domain the relaxation time were found to $t_{1/2} \sim 8 \cdot 10^5 s$, several orders of magnitude larger than the relaxation time for F domains $t_{1/2} \sim 6 \cdot 10^2 s$.

Organisms that are unable to regulate their own temperature, like bacteria, fungi and cold blooded animals, are often able to alter the lipid composition of their cellular membranes such that the fluidity of their cellular membranes is appropriate to the thermal environment. This adoption of the lipid composition in cellular membranes to the surrounding environments is known as Homeoviscous adaption. The homeoviscous adaption of E. Coli bacterias were examined by Sinensky in 1974[16]. The bacteria were grown at different temperatures ($15°C$, $30°C$ and $43°C$) and the fluidity of the membrane were measured at the growth temperature. The measured fluidity were independent on the growth temperature. In animal cells a similar temperature adoption occurs where the concentration of cholesterol is altered. At low temperature cholesterol will increase the fluidity of the lipid bilayer and at high temperatures it will decrease the fluidity[17].

1.5   Membrane models

To describe the function of cellular membranes some conceptual models have been developed. The purpose of such models is to explain known experimental results and to suggest new experiments. Singer and Nicholson presented the *fluid mosaic* model in 1972 [18]. The fluid mosaic model describes the cellular membrane as a two dimensional solvent containing oriented proteins which also acts like a permeability barrier. Proteins embedded in the lipid bilayer have usually both hydrophobic and hydrophilic regions. The protein will be located such that the hydrophobic region is inside the lipid bilayer and the hydrophilic regions can be outside the bilayer in the aqueous environment. The protein will maintain its orientation in the bilayer as the hydrophilic regions of the protein will avoid the apolar acyl tails inside the bilayer and thus prevent the protein from flipping. As the flipping rate for both lipids and proteins is extremely low, it is possible for living organisms to maintain an asymmetric

bilayer, where the lipid and protein composition can differ from one side to the other. In the fluid mosaic model the lipid bilayer is homogeneous and there is no large scale aggregation of proteins, as they are evenly distributed in the lipid bilayer. The mobility of proteins embedded in the cellular membrane can be measured using fluorescence recovery after photobleaching (FRAP). The diffusive motion of a protein in the cellular membrane can be described by the equation

$$S = \sqrt{4Dt} \tag{1.5}$$

where S is the average displacement after t seconds of diffusion and D is the diffusion constant. FRAP studies reveals diffusion constants for membrane proteins in the range $10^{-4} \rightarrow 0.4 \mu m^2/s$. The diffusion constant for lipids in the bilayer are approximately $1 \mu m^2/s$ [12]. Another model of the cellular membrane is the raft hypothesis proposed by Simons and Ikonen in 1997[19]. Raft domains are microscopic cholesterol rich membrane domains in the L_o phase, the purpose of the rafts might be to group related proteins for improving signalling processes[20]. Some proteins are highly concentrated in lipid rafts, one explanation of this preferential behavior can be that the proteins are equipped with an "address" consisting of a lipid shell[21].

1.6 Outline of the thesis

The used experimental techniques are described in chapter 2. The chapter covers both the preparation of supported lipid bilayers and how they can be investigated with fluorescence and atomic force microscopy. One of the techniques polarization fluorescence microscopy is based on linearly polarized light. The use of polarized light can be problematic as one of the materials, mica, used for supported lipid bilayers are birefringent and birefringent materials alter the polarization state of transmitted polarized light. Polarized light and how it is affected by birefringent materials are described in chapter 3. A short introduction to common image processing techniques is given in chapter 4. The fluorophore orientation in gel domains in a supported lipid bilayer have been examined with two photon fluorescence microscopy and the results are presented in chapter 5. Similar investigations of the fluorophore orientation have been conducted using one photon fluorescence microscopy. The obtained knowledge on fluorophore orientation in both gel and stripe domains are described in chapter 6, which also includes some observations on phase behaviour in supported bilayers. In chapter 7 the conducted work have been summarized in a conclusion.

Chapter 2

Experimental methods

In this project several experimental techniques have been applied to investigate the membrane phase behavior of lipid bilayers. The experimental goals were to gain information regarding lipid organization and orientation, membrane phase transitions and coexisting membrane phases. To study membrane phase domain formation and how they depend on the composition of the lipid membrane, methods for preparing and characterization of the membrane model systems are required. Phase transitions and domain growth were examined using fluorescence microscopy. Polarization fluorescence microscopy were used to infer knowledge on fluorophore orientation. Atomic force microscopy (AFM) have been used to visualize details of domain structures and boundaries.

2.1   Lipid bilayer model systems

When lipids are exposed to an aqueous solution they spontaneously form vesicles[4]. Vesicles consists of a lipid bilayer, that is bended into a sphere for avoiding contact between the aqueous solution and the hydrophobic lipid tails. The free floating lipid bilayers in vesicles may be the lipid bilayer model that best mimics the lipid bilayer in a biological membrane. Vesicles can be produced in various sizes: Small unilammelar vesicles (SUV) are less than $200nm$ in diameter and can be produced in large quantities and are used in methods such as differential scanning calorimetry (DSC) and small angle x–ray scattering (SAXS) for determining phase transition temperatures and lattice constants. SUVs are not suitable for any methods, based on optical microscopy, as the wavelength of visual light exceeds the SUV size, rendering it impossible to resolve features in SUVs. Features in giant unilammelar vesicles (GUVs), that can be larger than $10\mu m$, can be visualized by optical microscopy. Phase coexistence and domain formation in GUVs have been examined using confocal microscopy[22].

For resolving features, smaller than possible, with optical microscopic techniques, scanning probe microscopy techniques must be used. For examining

lipid bilayers at physiological conditions in aqueous solutions, methods that require vacuum cannot be used as the low pressure would cause the aqueous solution to boil. In AFM a probe interacts mechanically with the surface of the sample. If the sample that should be examined floats freely around in the solution, the mechanical interaction will cause a movement in the sample and such movements removes the possibility of acquiring images with AFM of freely floating lipid bilayers. By fixing lipid bilayers to a solid support, movements of the bilayer can be prevented; this is known as a supported lipid bilayer (SLB). SLBs can be examined using AFM. The flat geometry of planar supported lipid bilayers simplifies an eventual later analysis of the acquired images.

2.2 Materials for membrane support

SLBs consists of a lipid bilayer on top of a solid support, the physical properties of SLBs depends on both the composition of the lipid bilayer, the used solid support and the interactions between the lipid bilayer and the support. The influence of the support on the measurements leads to some requirements for a suitable solid support. If an optical microscope is used to examine SLBs the sample, and thus the support, must be transparent, as light is transmitted through the solid support. The goal of the solid support is to fixate the lipid bilayer spatially and therefore it must be mechanically stable. For keeping the lipid bilayer attached to the solid support, the bilayer must be attracted to the support. If the forces between the lipid bilayer and the support are strong, the ordering of lipids inside the bilayer can be perturbed. Height variations in the surface of the solid support can also perturb the bilayer. The requirements for a solid support can thus be summarized as

- mechanically stable

- flat surface

- optically transparent (only required for optical microscopy)

In the experiments two different materials have been used as solid support: glass and muscovite mica. Solid supports of glass slices have good optical properties as they are transparent to light and the mechanical stability of glass are not a problem but the surface roughness of glass causes troubles. A glass surface can have height variations in the order of $1nm - 3nm$ at length scales shorter than $50nm$, the size of these height variations are comparable to the thickness of a single lipid bilayer $\sim 5nm$[23].

Muscovite mica (mica) is a naturally occurring mineral with the chemical composition $KAl_2(AlSi_3O_{10})(FOH)_2$. A mica crystal consists of atomically flat layers which are stacked on top of each other. A piece of mica can be cleaved along such a flat layer, the surface of cleaved mica have $0.2nm$ height variations, which is an order of magnitude lower than glass[23]. A cleaved mica surface

exposed to an aqueous solution with neutral pH will have a surface charge of $-0.0025C/m^2$[24], this surface charge will induce repulsive forces between anionic lipids and the solid support, these forces will increase the distance between the solid support and the lipid bilayer, this reduces perturbations in the lipid bilayer caused by the solid support. The optical properties of mica are inferior to the properties of glass, as mica samples are only semitransparent at optical wavelengths.

In addition is mica a birefringent material[25], this property can cause problems when working with polarized light, for a detailed description see chapter 3. By decreasing the thickness of the mica slice, the issues caused by the optical properties can be reduced. When the thickness of the solid support is reduced, the mechanical stability of the solid support is significantly decreased and it must be stabilized. Mica glued to a glass cover slip with an optically transparent glue can be a solution[26], see figure 2.1. In the present work the most frequently used solid support was a sandwich composed of a glass cover slip and a $8mm \times 8mm$ piece of mica glued together with the transparent elastomer Nusil MED-6215.
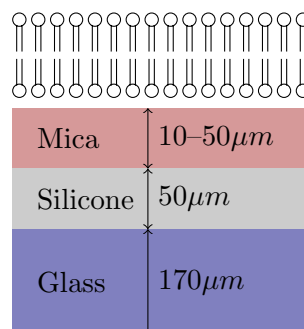

Figure 2.1: *Mica / glass sandwich.*

2.3 Preparation of supported lipid bilayers

There exist several methods for preparing SLBs, for a summary see [23]. The methods can be divided into three major groups (1) sequential deposition of monolayers on the solid support, (2) adsorption and fusion of SUVs to the solid support and (3) spincoating.

Lipid monolayers can be prepared by spreading lipid molecules in a volatile organic solvent on an water surface. After the organic solvent have evaporated the lipid molecules are left on the air / water interface. By reducing the area at which the lipid molecules are located, the lipid density can be increased until the surface tension reaches a given value. At this point a tightly packed lipid mono layer have been formed at the air / water interface. Langmuir studied how lipid molecules packed in a lipid mono layer using this technique[27]. Blodgett and Schaefer discovered methods for transferring lipid monolayers to a solid support by moving the solid support through the air / water interface[28]. Langmuir–Blodgett deposition corresponds to moving a vertically oriented solid support through the air / water interface; in Langmuir–Schaefer deposition the solid support are oriented horizontally. The deposition of monolayers on a solid support, allow the preparation of lipid bilayers with asymmetric lipid compositions.
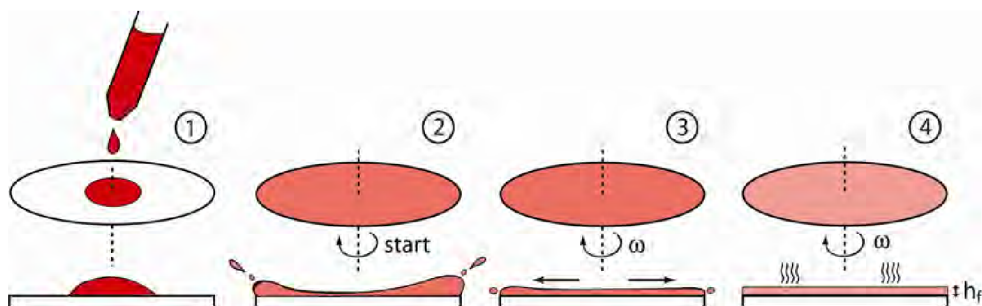
Figure 2.2: *The spin coating process, (1) coating solution is applied, (2) spinning is initiated and the excess amount of coating solution is cast away, (3) the remaining part of the coating solution is spread as a thin homogeneous layer and (4) the solvent in the coating solution evaporates. Image from Simonsen [23].*

Instead of transferring one lipid mono layer at a time to the solid support, it is possible to let SUVs adsorb to the solid support. SUVs can be prepared by adding lipids to an aqueous solution, in which vesicles will form spontaneously[29]. By pushing the vesicles through a grid with an appropriate hole size, the spontaneously formed vesicles can be split into SUVs with diameters comparable to the size of the grid holes. When a hydrophilic solid support is exposed to the solution of SUVs, the SUVs spontaneously fuse and form a single lipid bilayer on top of the solid support. Vesicle fusion cannot be used to prepare supported lipid bilayers containing more than 20% anionic lipids[30].

Spin coating Spin coating is a new technique for preparing SLBs, that is able to produce defect free SLBs for large areas[31]. The spin coating technique can be used for applying a thin uniform layer (a coating) to a surface. SLBs can be prepared using the spin coating technique, this was described by Mennicke *et. al* [32] and later characterized by Simonsen *et. al* [31]. For spin coating a surface with a given lipid mixture, the lipid mixture should be in a volatile solvent which wets the solid support. For preparing SLBs with glass or mica, as solid support, a solvent mixture composed of 60% isopropanol, 20% hexane and 20% water can be used, as it can dissolve most lipids and it wets the glass / mica surface. The solid support is placed in the spin coater (Chemat Technology Spin–Coater KW–4A), $30\mu L$ of the lipid solution is applied to the support and immediately hereafter the surface is spun at 3000 rpm for 40 seconds. The spin coating process is visualized in figure 2.2. During spinning the applied solution is spread evenly over the surface, as centripetal and adhesive forces are applied. The centrifugal forces will force the solution to flow away from the center of rotation, this flow will continue until a thin layer is left, which

will be kept in place by adhesive forces until the spinning is stopped. After spinning the surface is covered by a mixture of some remaining solvent and the deposited lipid bilayers. To ensure that all the solvent is removed from the sample, it is placed in a desiccator under vacuum.

The thickness of the final lipid coating can be controlled by varying lipid concentration c (mass fraction units) and angular frequency ω. The coating thickness also depends on some parameters for the used solvent, that is the evaporation rate (decrease of thickness in m/s) and the initial kinematic viscosity of the coating solution v_0 (m^2/s). Meyerhofer suggested the following semi–empirical expression for estimating the final film thickness h_f[33].

$$h_f = \left(\frac{3}{2}\right)^{1/3} c_0(1-c_0)^{-1/3}\omega^{-2/3}v_0^{1/3}e^{1/3} \qquad (2.1)$$

For low lipid concentrations the thickness of the final coating scales linear with the lipid concentration.

How the lipid molecules in the formed thin layer are organized depends on the used solid support. The lipid organization on a hydrophilic support is shown in figure 2.3a. After the evaporation of the solvent, the lipid molecules are organized in layers, which we will denote leaflets; in one leaflet all the lipid molecules are oriented similar. In the leaflet closest to the solid support (L1), the polar lipid head groups are attracted to the hydrophilic support. The leaflet closest to the hydrophilic support will thus be aligned with the polar lipid head groups near the support and the apolar lipid tails pointing away from the support. In the next leaflet (L2), the lipid tails are directed downwards, as they are attracted to the lipid tails of the lipids in the first leaflet. The coverage of the lipid leaflets is related to the lipid concentration in the solution; higher lipid contents increases the leaflet coverage. If enough lipid is applied, additional lipid leaflets can be deposited. The last leaflet of lipid molecules will have the lipid tails directed upwards[23] towards air / vacuum which is apolar. The next step in the formation of a spin coated SLB is the addition of an aqueous buffer solution. The lipid organization after addition of the aqueous solution is shown on figure 2.3b. During hydration the hydrophobic acyl chains of the upper lipid leaflet (the leaflet that were earlier in contact with air) will be exposed to the aqueous buffer; this is not energetically favourable and as a consequence the upper lipid leaflet will be flushed away. In the remaining leaflets the acyl chains in one leaflet, are shielded from the aqueous solution by another matching lipid leaflet. Such two matching lipid leaflets forms a lipid bilayer. In figure 2.3b the lipid leaflets L1 and L2 forms the lipid bilayer M1. Whereas the lowest lipid bilayer M1 can be significantly perturbed by interactions with the solid support, the next bilayer M2 is almost completely shielded from these interactions and will float freely[34, 26].
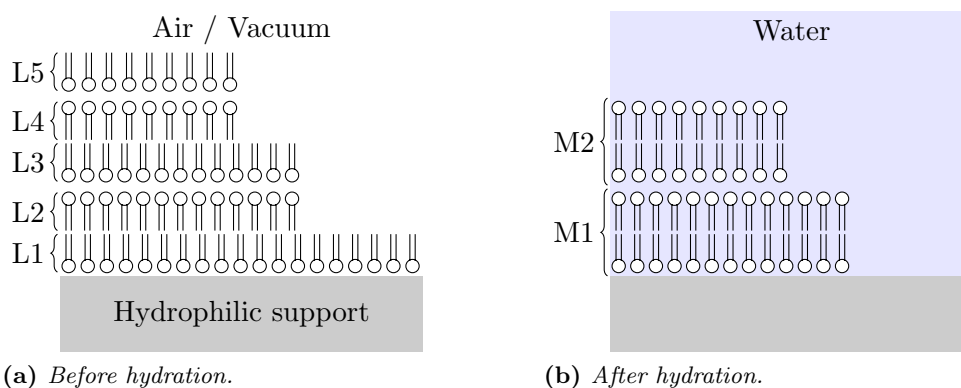
Air / Vacuum

Water

L5 {
L4 {
L3 {
L2 {
L1 {

M2 {
M1 {

Hydrophilic support

(a) *Before hydration.*

(b) *After hydration.*

Figure 2.3: *Lipid layers after spincoating. During hydration the lipids with unshielded acyl chains will leave the sample.*

2.4 Fluorescence microscopy

An attempt of visualizing the membrane phase domains in the formed bilayers using an optical microscope will fail, as the optical microscope cannot produce enough contrast to create an image of the membrane phase domains. By staining the lipid bilayer with a fluorescent probe that prefers one membrane phase compared to a different membrane phase more contrast can be generated. For exciting the fluorophore the sample is illuminated by light at a specific wavelength that matches the chosen fluorophore. By limiting the acquired light to a narrow range of wavelengths near the emission wavelength of the fluorophore, the contrast can be increased further. The pixel intensity in a fluorescent image is related to the concentration of the fluorescent probe at the corresponding location in the sample.

In an epifluorescence microscope the excitatory light is guided towards the sample through the same objective that is used for collecting the light from the fluorophore in the sample. The structure of such a microscope is shown in figure 2.4. Light is guided from the light source through an excitation filter and are reflected by a dichroic mirror, after the mirror the light is focused by the objective on the sample where it excites the fluorophore molecules. The light emitted from the fluorophore is via the objective guided through the dichroic mirror and a fluorescent filter before it is focused and the image is formed. The dichroic mirror is chosen such that the excitatory light is reflected and the emission light is passed through. Finally the image is formed by counting the number of photons that are collected from a specific region of the sample during the exposure time. The excitation filter determines which light that will excite the fluorophore. By inserting a linear polarization filter before the excitation filter, the fluorophore will be illuminated with linearly polarized light. As the fluorescence intensity of a fluorophore depends on the orientation
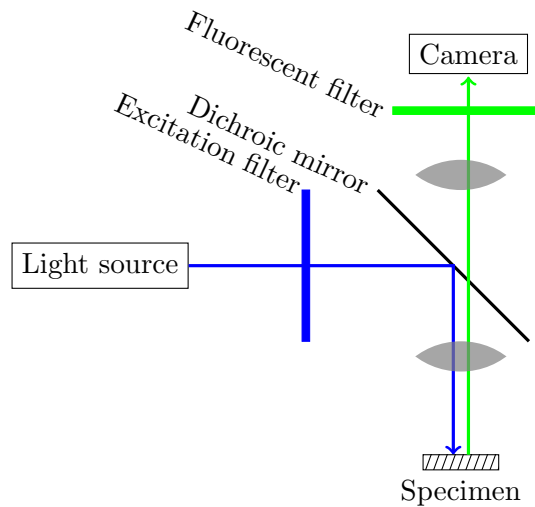
Figure 2.4: *General setup of a epifluorescence microscope*

of the electrical field in the illuminating light, some information regarding the fluorophore orientation can be obtained. For more details see chapter 5.

The signal to noise ratio (SNR) in the acquired image depends on the number of photon counts belonging to each pixel. As the emission of light from a fluorophore is a random event, the number of counted photons can be described by a Poisson distribution. The SNR from a Poisson process are given by $\sqrt{\lambda}$ where λ is the expected number of events. As λ scales linearly with the exposure time, the SNR and thus the quality of the formed image can be increased by increasing the exposure time. This is only true if a static sample is being imaged. If the sample moves, changes shape or grows during the exposure time, it will lead to a blurred image.

2.4.1 One–photon and two–photon microscopy

In one photon fluorescent microscopy, the fluorophore is excited by a single photon. As the absorption process involves one photon the fluorescence intensity scales linearly with the intensity of the excitatory light. In the microscope the area of the sample that should be examined is homogeneous illuminated by the excitation light, the photons emitted from the sample are collected by a charge coupled device (CCD). A computer can then collect data from the CCD and forms a fluorescent image. An issue with one photon fluorescent microscopy is that the fluorophores are exposed to the excitatory light for longer periods of time during image acquisition, that causes the fluorophore to photo bleach. The fluorophore is also bleached outside the focal area, as shown in figure 2.5. Fluorophores used in one photon fluorescent microscopy should in general be very photo stable.
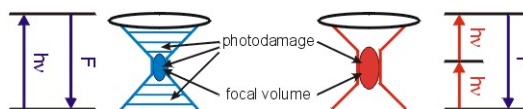
Figure 2.5: *Comparison of the focal and photo damage volume of one and two–photon microscopy. Image from Gensch [35].*

Maria Göppert-Mayer predicted in 1931 the possibility of fluorophore excitation by simultaneous absorption of two photons[36]. As two photons are involved in the absorption process, it scales quadratic with the light intensity. This prediction was confirmed experimentally by Abella in 1962, where he was able to excite Cs atoms by two photon absorption [37]. The time between the absorption of the two photons must not exceed ~ 0.1fs, thus very high photon densities are required for obtaining a significant number of two photon excitations. In two photon microscopes the excitation light is generated by lasers. The required light intensity is so high that it is not possible to illuminate larger parts of the sample simultaneously. Instead of illuminating the entire sample, the excitatory light is scanned over the area that is to be imagined. At each location the number of photons emitted from the sample are counted using photon multipliers. When the laser beam is focused on the sample, mainly the area inside the focal volume contributes to the fluorescent intensity, see figure 2.5. The size of the focal volume is determined by the diffraction limit. Outside the focal volume the photon density is to low to cause significant photo bleaching. An advantage of two–photon excitation is that only a tiny fraction of the sample is illuminated, which reduces the problems caused by photo bleaching and allows the use of a wider variety of fluorescent dyes.

The used one photon microscope is a Nikon Eclipse TE2000–U epifluorescence microscope equipped with a G–2A filter cube and a 40X long range working distance objective. A PCO Sensicam 682KX CCD camera is used for acquiring images. The light source is a Polychrome V Xenon arc lamp from Till Photonics. A linear polarizing filter that can be rotated is inserted between the light source and the filter cube. The used two–photon microscope is custom built by Jonathan Brewer (MEMPHYS SDU) based on an Olympus IX70 microscope. For exciting the fluorophore a femtosecond Ti:Sa laser (Broadband Mai Tai XF W25) is used.

2.4.2 Fluorescent dyes

Basically a fluorescent dye is a molecule that can absorb one or more photons, the absorption should place the molecule in an electronically excited state from which a photon can be emitted. The ability to absorb and emit photons is not sufficient for making a good fluorescent dye, a good performing dye must be sufficiently resistant to photo bleaching and absorb and emit photons at

wavelengths that can be controlled and measured by the used microscope.

A molecule can be in different electronic and vibrational states, each state have an associated energy level. When a fluorophore absorbs one or more photons, it will enter an excited stated. The energy difference between the initial state of the fluorophore and the excited state are the total energy of the absorbed photons. Before absorption we assume that the fluorophore is in the state with lowest energy, the ground state. The photon absorption takes all the energy from the exciting photon(s) and stores it in the fluorophore by exciting it to higher electronic and vibrational states. The probability of absorption depends on the wavelength of the excitation illumination and the direction of the electrical field in the excitation illumination. For exciting the fluorophore electronically the electron configuration in the fluorophore must be altered. How the electrical field $\mathbf{E}$ of the illuminating light interacts with the fluorophore is described by the transition dipole $\mathbf{p}$. The probability of absorbing a photon is maximally when $\mathbf{p}$ and $\mathbf{E}$ are parallel and minimal when they are orthogonal.

In a one photon epifluorescence microscope the light that is collected from the sample consists of both emitted (fluorescent) and reflected illumination light. During the image acquisition the signal of interest consists of the fluorescent emitted light. The scattered light contain no information on the fluorophore distribution and will only decrease the achievable contrast. Fortunately the excitation and emission spectre of a fluorophore will in general have peaks located at different wavelength, the distance between the two peaks is the *Stokes shift* of the fluorophore. By using appropriate filters the Stokes shift can be used to split the fluorescent emitted light from the scattered illuminating light. After photon absorption the absorbed energy is stored in excited electronic and vibrational states. During collisions with surrounding molecules the fluorophore can dissipate the energy stored in the vibrational states and afterwards the energy remaining in the excited electronic stated can be emitted as a photon. The Stokes shift is caused by the energy that is lost during these collisions.

The properties of the fluorescent probe determines which features of the sample that can generate contrast. For examining the membrane phase behavior of lipid bilayers fluorophores, that can be embedded in the bilayer, are required. There exist several fluorophores that mimic the structure of lipids (long acyl chains and polar head groups) and thus can be embedded in a lipid bilayer. For generating contrast between two distinct membrane phases the fluorophore must either have a preference for one of the distinct membrane phases or the excitation / emission spectre of the fluorophore should depend on the membrane phase.

DiI

1.1'-dioctadecyl-3,3,3',3'–tetramethylindocarbocyanine (DiI) is an amphiphilic molecule with fluorescent properties, consisting of a polar "head" structure
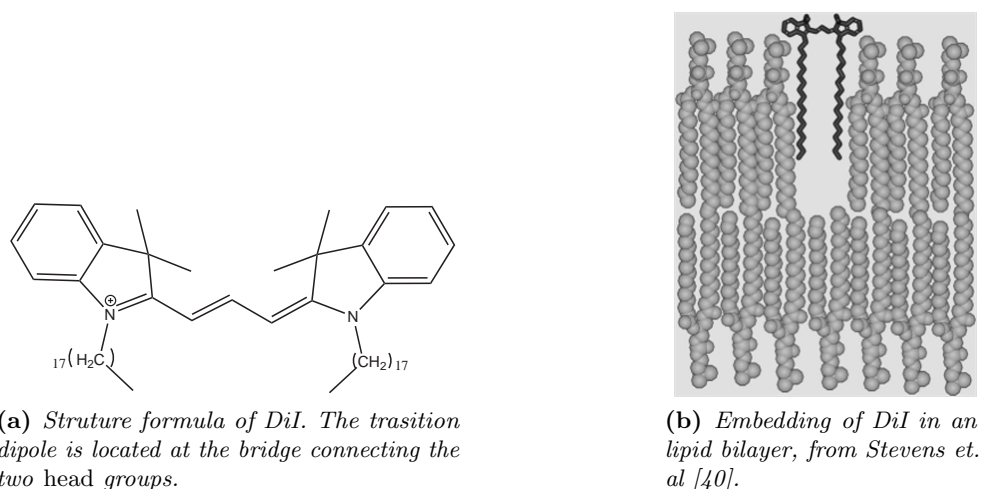
(a) *Struture formula of DiI. The trasition dipole is located at the bridge connecting the two* head *groups.*

(b) *Embedding of DiI in an lipid bilayer, from Stevens et. al [40].*

Figure 2.6: *The structure of DiI and how it embeds in a lipid bilayer. The transition dipole of DiI will lie in the plane of the lipid bilayer.*
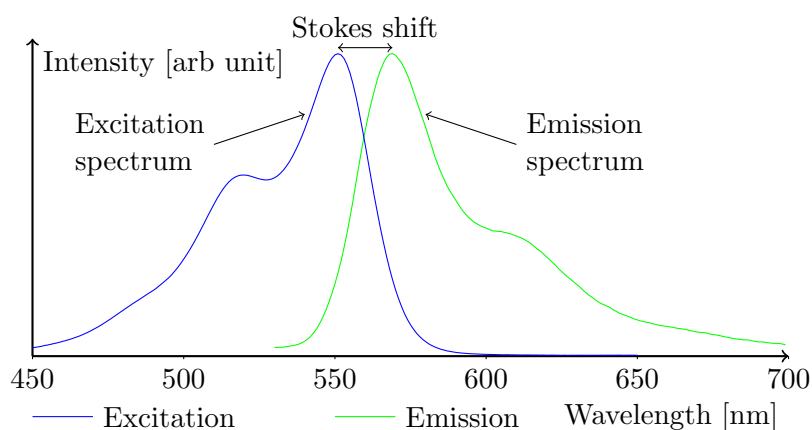
Figure 2.7: *DiI–C18 excitation and emission spectrum. Data from Invitrogen [41].*

with two attached fatty acids. DiI is suitable as fluorophore in single photon microscopy, as it is bleached slowly. The fluorophore is embedded in the lipid bilayer as shown in figure 2.6. The transition dipole of DiI lies in the plane of the membrane [38, 39]. The excitation peak of DiI is at $551nm$ and the emission peak is at $569nm$, the full excitation and emission of DiI is shown in figure 2.7.

As DiI prefer to be in some membrane phases rather than others it is often used to distinguish domains with different phases. Which phase that appears the brightest in a membrane depends on the lipid composition. In

(a) *POPG/DPPC (1:1)* **(b)** *POPC/DPPG (1:1)*

Figure 2.8: *How the gel, ripple and fluid domains appear in two samples stained with DiI. In both samples are the stripe / ripple domains the brightest. The relative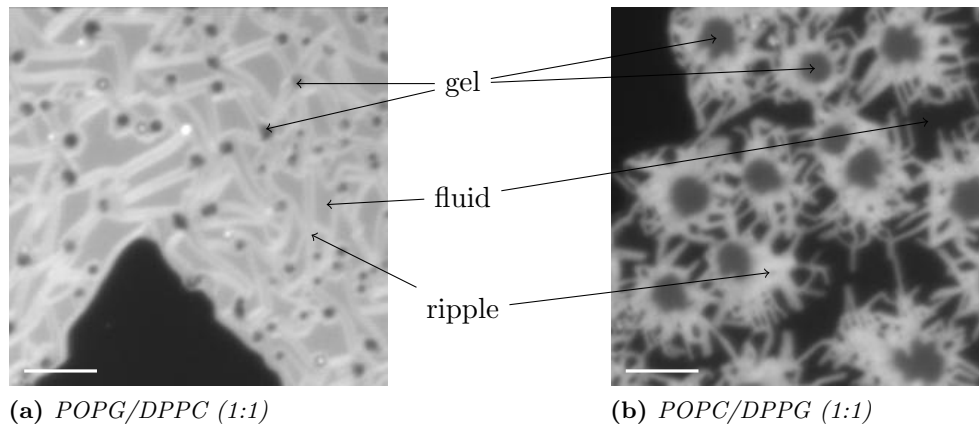 brightness between the gel and fluid phases depends on the lipid composition, in this case the attraction of the positive charged DiI to the phase rich in the anionic PG lipid can explain the change in brightness. $10\mu m$ scale bars.*

lipid bilayers composed of DPPC / POPC DiI prefers the fluid phase[31]. As DiI is positive charged, it is attracted by anionic lipids like POPG and 1,2-dipalmitoyl-sn-glycero-3-phosphoglycerol (DPPG) (both phosphoglycerols), this causes membrane phases rich in anionic lipids to appear more bright. On figure 2.8 two images of membrane domains in mixtures of POPG / DPPC and POPC / DPPG is shown. Each image contain the three membrane phases: fluid, stripe and gel. The stripe phase is more bright than both the gel and fluid phase in both mixtures, indicating that DiI has a preference for the stripe phase. In the POPG / DPPC mixture, the fluid phase is brighter than the gel phase, this contrast is explained by the higher concentration of anionic lipids in the fluid phase. The opposite is the case in the POPC / DPPG mixture, where the gel domains are brighter than the fluid domains.

The fluorescence intensity of DiI embedded in a fluid membrane domain depends on the temperature of the sample. In figure 2.9 the fluorescence intensity of DiI in various lipid composition are shown as a function of the temperature. When the temperature is lowered, the fluorescent intensity increases. Such temperature dependences are observed for several other fluorophores[42].

Laurdan

6-lauroyl-2-dimethylaminopahthalene (Laurdan) can be used as a fluorescent probe for two photon microscopy; the probe is not suitable for one photon microscopy as it bleaches very fast (in a matter of seconds). When added to a
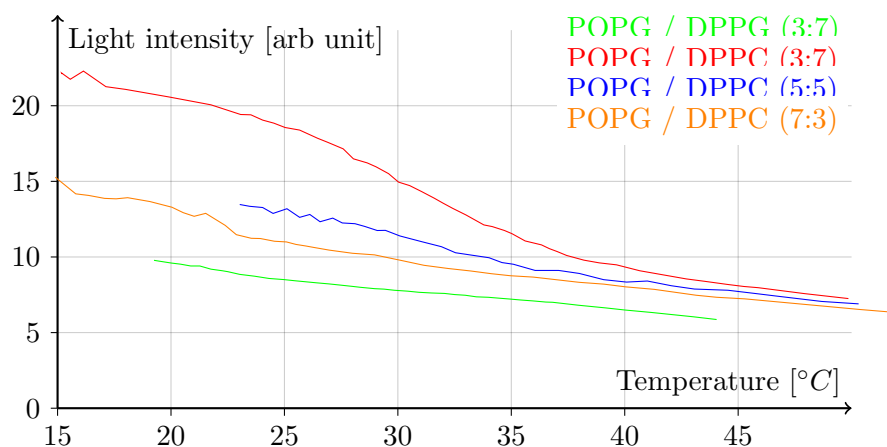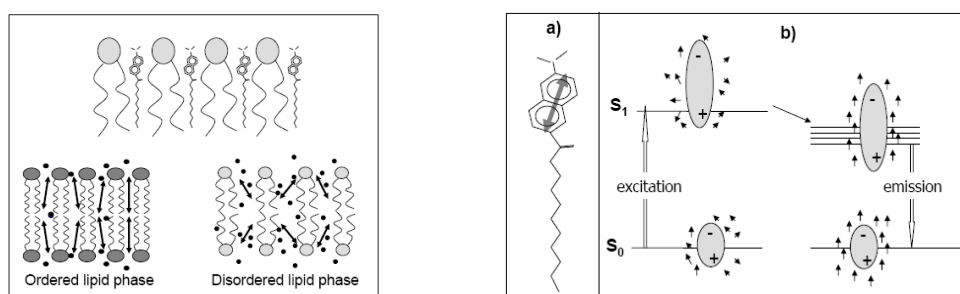
Figure 2.9: *Measured light intensity of bilayers stained with DiI. Each curve is scaled independently, so do not conclude that DiI is brighter in a POPG / DPPC (3:7) bilayer compared to a POPG / DPPG (3:7) bilayer.*

(a) *Laurdan orientation in a gel and fluid membrane.*

(b) *The emission spectre of Laurdan is red shifted in polar solvents, as some of the energy stored in the electrical excited stated is used to align the polar molecules in the solvent.*

Figure 2.10: *Laurdan in a lipid bilayer. In an ordered lipid phase like the gel phase water (the black dots) is unable to get near the fluorophore, in a disordered lipid phase water can get near the fluorophore thus changing the environmental polarity of the fluorophore which results in a changed emission spectre. Images from Sanchez et. al[43].*

lipid bilayer, Laurdan will be located in the apolar region and aligned with the fatty acid chains from the lipids [43]. The molecular structure and how Laurdan is embedded in a lipid bilayer is shown in figure 2.10a. Laurdan has no preferred phase and will thus be evenly distributed across membrane phase domains. In a gel / ordered phase Laurdan will be parallel to the lipid acyl chains with small oriental fluctuations. The oriental fluctuations will be much
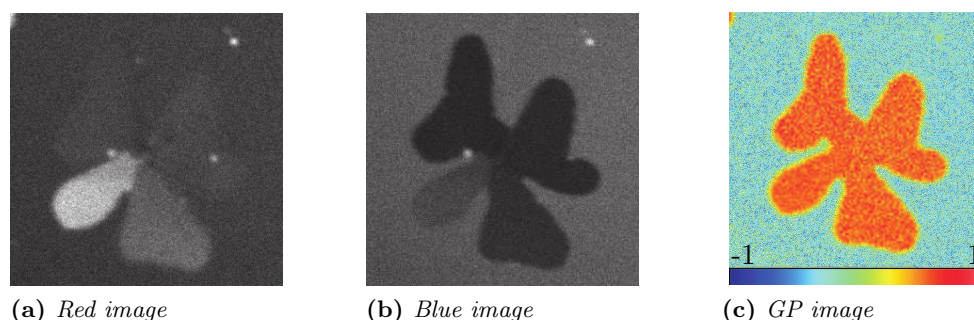
(a) *Red image* **(b)** *Blue image* **(c)** *GP image*

Figure 2.11: *Generalized polarization image of a gel domain.*

larger when the lipid bilayer is in a fluid / disordered phase. The transition dipole of Laurdan will be parallel to the acyl chains.

What makes Laurdan ideal for investigating membrane phase behavior is that the emission spectre reflects the membrane phase. After excitation Laurdan will have a large dipole moment, in which the energy from the absorbed photons is stored. In the dipole the energy is stored in the surrounding electrical field. If water molecules (or other dipoles) are present, some of the energy stored in the electrical field will be used to align the water molecules along the electrical field, this is shown in figure 2.10b. Fluid domains where water molecules can get near Laurdan will have red shifted spectre and gel domains where water molecules cannot get near Laurdan will have blue shifted spectre. By simultaneously acquisition of images from the red and blue part of the spectre (see figure 2.11a and 2.11b) the generalized polarization function (GP) can be used for visualizing membrane phases. GP is defined as

$$GP = \frac{I_{440} - I_{490}}{I_{440} + I_{490}} \tag{2.2}$$

where I_{440} is the blue image and I_{490} is the red image. In figure 2.11c a gel domain in a DPPC / DOPC SLB is visualized using the GP values.

2.5 Atomic force microscopy

When small features of a sample should be examined, fluorescence and optical microscopy techniques are no longer an option, as they cannot resolve features smaller than the wavelength of the used light[44]. While optical methods probe the sample structure by using photons, the sample structure can be measured using other techniques. Scanning probe microscopy (SPM) is a class of microscopy techniques where a probe is scanned over the sample. At each location that should be examined the probe is moved in direction of the sample until some criteria is fulfilled. By repeating such measurements, an image of the height variations in the sample can be generated. AFM is one of the SPM
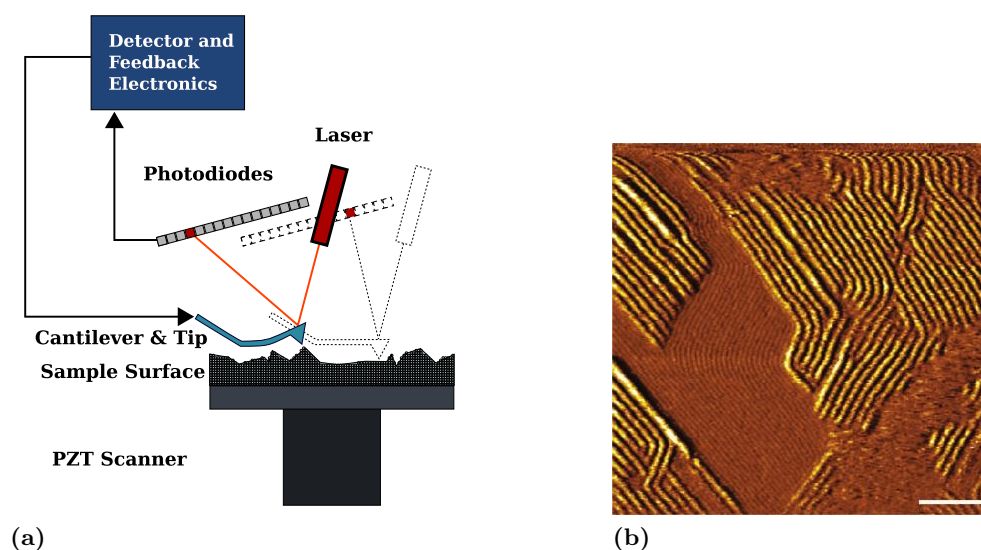
Figure 2.12: *(a) Principle of the AFM microscope. Image from wikipedia.org. (b) AFM image of a supported double bilayer composed of an equimolar mixtures of DMPC and DSPC. The scale bar is* $200nm$. *Image from Leidy et. al [46].*

techniques, it was invented by Binnig, Quate and Gerber in 1986[45]. In AFM interactions between a very sharp tip and the sample are used as the probing method, this principle is sketched in figure 2.12. The tip is placed on a flexible cantilever that is moved towards the sample, when the tip touches the sample, the cantilever will be bended. The bending of the cantilever can be measured by reflecting a laser beam on the backside of the cantilever and measure the deflection by a quadrant photodiode. The tip and cantilever system is able to measure height differences in the Å scale[47]. The lateral resolution can be better than $1nm$, but is effective limited by the used cantilever tip and its shape[48]. A blunt tip will not be able to get into cavities in the sample that are smaller than the tip, thus an AFM microscope with a blunt tip will not have the same resolving power as an AFM with a sharp tip. A sharp tip can end in a single atom, and it will let the AFM resolve features on the atomic scale. The effect of using a blunt tip to resolve small features is visualized on figure 2.13. In the figure a parabola shaped tip is used to examine a sample with features sizes smaller than or comparable to the tip curvature. The red line is the measured height of the sample, if the cantilever tip is placed on the red line it will touch the sample at least in one place. For structures larger than the tip, the measured sample shape will be nearly similar to the real sample shape. The measured shape near structures that are smaller than the tip are significantly distorted and the measured shape will be an inverted image of the tip. Mathematically the relation between the real sample shape S_{real}, the tip shape T and the measured sample shape S_{meas} can be expressed as a
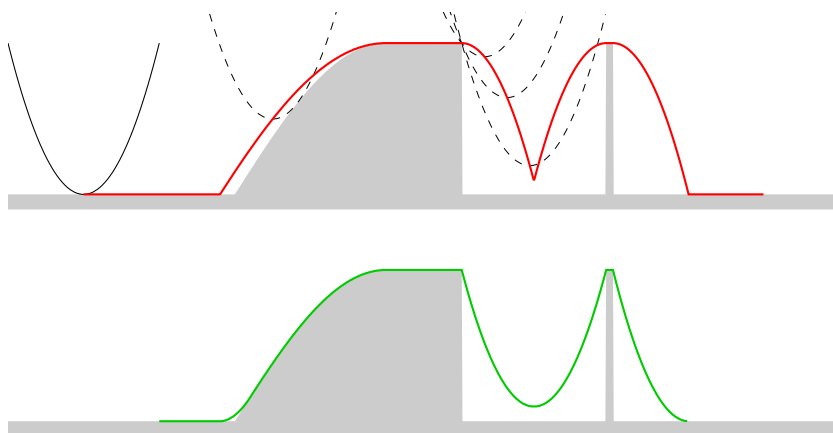
Figure 2.13: *How the real sample is characterised using a round cantilever tip. Red line is the measured sample hight and the gray box is the real sample height. If the tip shape is known, some of the distortions caused by the tip can be removed by erosion, this is shown in green.*

dilation[48].

$$S_{\mathrm{meas}} = S_{\mathrm{real}} \oplus T \tag{2.3}$$

If the tip shape is known, it is possible to estimate the real sample shape from the measured shape, this is done using an erosion:

$$S_{\mathrm{esti}} = S_{\mathrm{meas}} \ominus T \tag{2.4}$$

The dilation $\oplus$ and erosion $\ominus$ operations are defined in section 4.2. In figure 2.13 the green line represents the estimated sample shape. For features larger than the tip, the estimated sample shape will be identical with the sample and for smaller features some artifacts from the tip shape will still be present. It is not possible to get rid of these artifacts, as the details in these areas have never been in touch with the cantilever tip. Usually the tip shape is unknown, but sometimes it is possible to get an estimate of the tip shape. This tip estimate can then be used to remove artifacts induced by the tip shape[48].

As AFM interacts mechanical with the sample, no staining of the sample is needed. The used AFM is a JPK NanoWizard which can be combined with the one photon fluorescent microscope mentioned in section 2.4.

2.6   Sample holder and temperature control

The SLBs have been examined while they were submerged in the aqueous buffer solution used to hydrate the sample. The buffer solution were kept in place by a sample holder, which consisted of buffer container where bottom consisted of
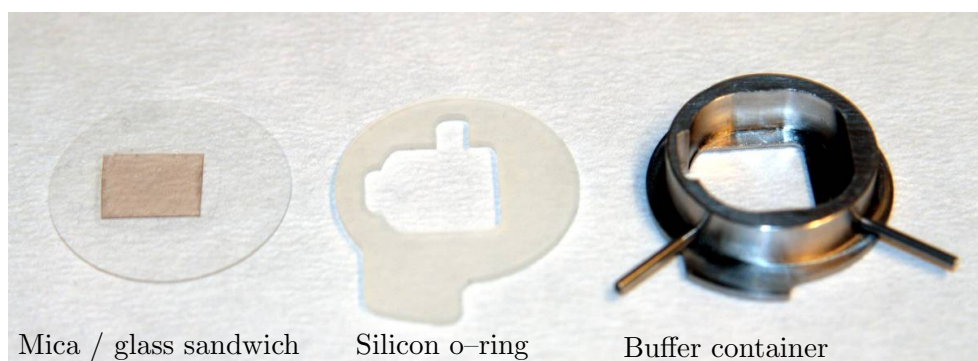
(a) *Sample container*

(b) *JPK Biocell*

(c) *Temperature controller*

Figure 2.14: *The used sample holder and temperature control.*

a cover glass on which a thin slice of mica were glued. The prepared SLB were located on the mica surface. For avoiding leakage from the sample holder an o–ring made of silicon is inserted between the cover slip and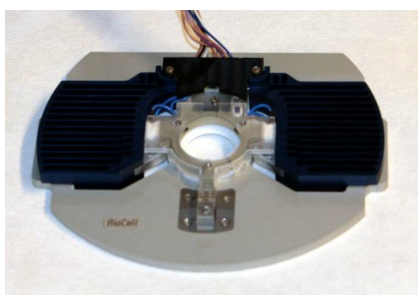 the sides of the buffer container. All the elements of the sample holder are shown on figure 2.14a. The sample holder fits inside a JPK Biocell, shown on figure 2.14b. The used JPK Biocell is equipped with a thermometer and Peltier elements for controlling the temperature inside the buffer container. The Peltier elements are controlled by an Eurotherm 2408 temperature controller. The temperature controller can be programmed to keep the sample at a given temperature or to change the temperature gradually following a "temperature ramp". Sample temperatures in the range $15°C$ to $55°C$ can be maintained.

For documenting the temperature history of a sample, a temperature logger have been used. The temperature logger is based on a K–type thermocouple connected to a computer via an interface from National Instruments (NI-USB9162 and NI-9211). During an experiment, the thermocouple is submerged in the buffer inside the sample holder. The temperature is not constant throughout the sample holder, as the temperature of the sample holder is influenced by the surrounding air at room temperature and the Peltier elements which try to keep the sample at a given temperature. Ideally the sample
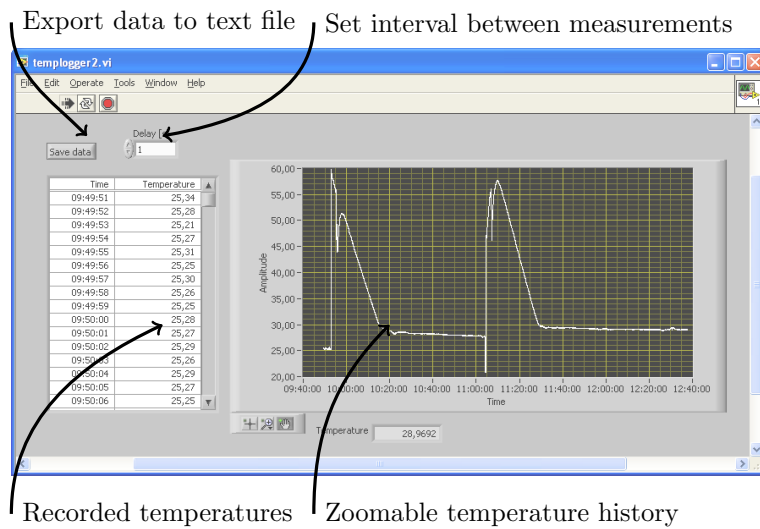
Figure 2.15: *Screenshot of the temperature logger program*

temperature should be measured at the image acquisition location, if the thermocouple is placed at a different location it could cause a systematic error in the measured temperature. A LavVIEW program have been developed for performing the actual data acquisition, a screen shot of the program is shown in figure 2.15. The main purpose of the program is to acquire the current temperature measured by the thermocouple every second. After acquisition the measured temperatures can be exported to a plain text file where each line contains corresponding time and measured temperature values in the format:

```
11:08:35    56,33
11:08:36    56,32
11:08:37    56,38
11:08:38    56,36
11:08:39    56,45
```

In addition to the record and save to file functions, the program allows the user to zoom and pan in the acquired thermal history.

The software used for image acquisition, TILLvisION, can save some additional information about the acquired images to an external file. Using this information, it is possible to equip all images with time acquisition and the corresponding sample temperature. A typical temperature sequence consists of an equilibrating phase in which the sample is kept at temperatures above the main transition of the components in the lipid bilayer and then cooled at a fixed rate until a target temperature is reached. Such a temperature cooling sequence is shown in figure 2.16.
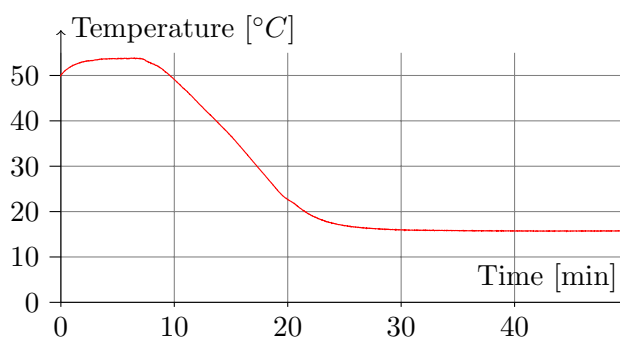
Figure 2.16: *Logged temperature over time during a cooling ramp.*

2.7 Protocols

Several different samples have been prepared. All the used lipids and some of the characteristics is shown in table 2.1. The sample preparation consisted of solubing lipids in a specific solvent composed of water, hexane and isopropanol, see fractions in table 2.2a. The buffer used for the experiments contained salt at physiological concentrations in addition to 4-(2-hydroxyethyl)-1-piperazineethanesulfonic acid (HEPES), Ca^{2+} and ethylenediaminetetraacetic acid (EDTA). The concentrations are given in table 2.2b.

A typical experiment is described below

1. Lipid suspension is spincoated on a mica plate.

2. Place sample in exicator for at least 45 min

3. Hydrate sample with buffer

4. Place hydrated sample in 55° oven for 30 min.

5. Start to examine the sample with the one photon microscope

6. Exchange buffer until only the lowest one or two layers remains bound to the support

7. The sample is cooled at a steady rate

8. Images are acquired to determine how the fluorescence intensity is change during the cooling ramp

9. When a set temperature is reached, the cooling ramp is terminated.

10. The sample is allowed to rest for at least 10 min

11. A sequence of images with altering polarizations is acquired

Lipid	Chains	Molecular weight $[g/mol]$	T_m	Source
DLPC	12:0 12:0 PC	721.840	$-0.4°C$	[49]
DOPC	18:1 18:1 PC	786.150	$-40.3°C$	[50]
DPPC	16:0 16:0 PC	734.050	$42.7°C$	[51]
DPPG	16:0 16:0 PG	744.960	$41.5°C$	[52]
POPC	16:0 18:1 PC	760.090	$-3.4°C$	[53]
POPG	16:0 18:1 PG	771.000	$1°C$	[51]

Table 2.1: *Some properties of the phospholipids used in the conducted experiments.*

Species	Volume fraction
Isopropanol	60%
Hexane	20%
Water	20%

(a) *Solvent used for dry lipids.*

Species	Concentration $[mM]$
NaCl	$150mM$
HEPES	$10mM$
Ca^{2+}	$30mM$
EDTA	$10mM$

(b) *Used buffer for the experiments.*

Table 2.2: *Contents of the solvent used for solutions of lipids and contents of buffer use in the experiments.*

Chapter 3

Use of polarized light to determine membrane structure

Polarized light is a vital part of polarized fluorescence microscopy as described in section 2.4. Using polarized fluorescence microscopy it is possible to gain knowledge about the orientation of a fluorophore in a given sample. The polarization state of a light beam can be altered when the beam is reflected or transmitted through a birefringent material. Mica, one of the materials that can be used as support for SLBs, have birefringent properties, this is visualized in figure 3.1. The figure show a LCD display with a piece of $0.2mm$ thick
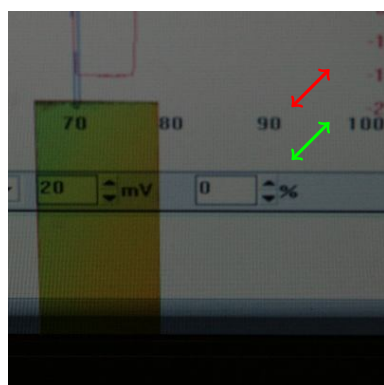
(a) *Parallel polarizers*
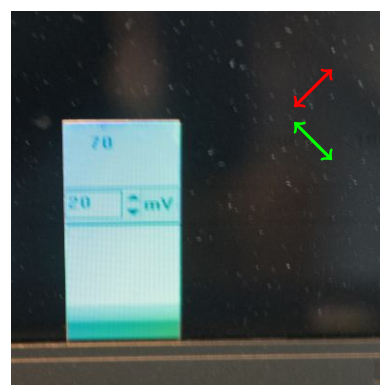
(b) *Crossed polarizers*

Figure 3.1: *How mica distorts the polarization of light. The green arrow indicates the orientation of the electrical field in the light emitted from the LCD display. The red arrow is the direction of the electrical field that the used polarization filter transmits.*

$$\phi = 0 \qquad \phi = \pm\pi/2 \qquad \phi = \pi/6$$

Figure 3.2: *Different polarization states of light. From the left: linear, circular and ellipsoid polarized light.*

mica in front of part of the display. The light emitted from the LCD display is linearly polarized in the direction indicated by the red arrow. In figure 3.1a the LDC display is viewed through a linear polarization filter. The polarization filter is oriented such that light polarized in the direction marked by the green arrow is allowed to pass. It is seen that the light transmitted through mica is attenuated. In figure 3.1b the polarization filter have been turned 90°, now the linear polarized light emitted from the LCD display cannot pass the polarization filter and the LCD display appea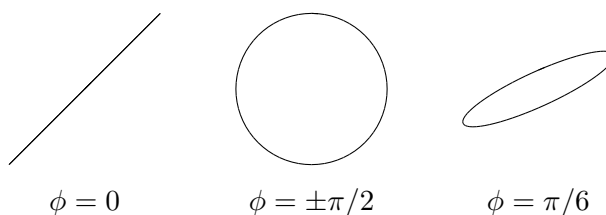rs dark. But the light from the LCD display that were transmitted through mica can now pass the polarization filter, thus mica must alter the polarization state of the transmitted light. This chapter describes the properties of polarized light and how polarized light is affected by birefringent materials. Finally some experimental implications are described.

3.1 Properties of Polarized light

Light consists of electromagnetic waves. The electric field of a harmonic oscillating wave can be described by how the electrical field in the x and y direction changes over time. Mathematically it can be written as

$$E_x(t) = E_x^0 \cdot \sin\left(\omega \cdot t\right)$$
$$E_y(t) = E_y^0 \cdot \sin\left(\omega \cdot t + \phi\right)$$

where E_x^0 and E_y^0 are the amplitude of the oscillation in the x and y plane and ϕ is the phase offset between these oscillations. The polarization state can be visualized by drawing the time evolution of $\vec{E}(t) = E_x(t)\vec{x} + E_y(t)\vec{y}$ through one oscillation. On figure 3.2 the time evolution of the electric field is shown for three different values of ϕ. When the two electric fields oscillate with no phase offset ($\phi = 0$), the trace of the electric field is a line, this is denoted linearly polarized light. If the phase offset equals $\pm\pi/2$ and the oscillation amplitude in each direction is equal ($E_x^0 = E_y^0$), the light is circular polarized. All polarization states can be described as an ellipsoid (lines and circles are degenerate ellipsoids), by their semimajor and semiminor axis and the angle
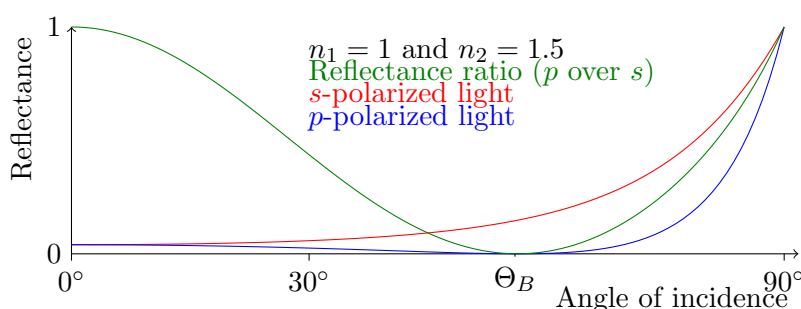
Figure 3.3: *Reflection of s and p polarized light as a function of the incidence angle, the ratio of reflected p and s polarized light is shown in green. The used indices of refraction corresponds to air and glass.*

between the semimajor axis and the x–axis. A small phase offset corresponds to an elongated ellipse. Not all light is polarized. Light where the orientation of the electrical field varies randomly is not polarized and is denoted apolar[54].

Generating linearly polarized light Light emitted as thermal (blackbody) radiation is apolar, as there is no system in how the photons are emitted. Apolar light can be (partially) polarized using either reflection or polarization filters. In a reflection process light is reflected from a boundary between two optically different materials. The intensity of the reflected light depends on the polarization of the incident beam, the angle of incidence Θ and the refractive indices of the two involved materials. Light polarized in the plane of incidence is denoted p polarized light and light polarized perpendicular is denoted s polarized light. The amount of reflected light at the boundary between two dielectric materials, are expressed in terms of the Fresnel coefficients. The coefficients (r_{12s} and r_{12p} describes which fraction of the electrical field that are reflected at the boundary; the intensity of the reflected beam is given by the coefficients squared. [55, p. 449].

$$r_{12s} = \frac{n_1 \cos\Theta_1 - n_2 \cos\Theta_2}{n_1 \cos\Theta_1 + n_2 \cos\Theta_2} = \frac{\sin(\Theta_2 - \Theta_1)}{\sin(\Theta_2 + \Theta_1)}$$

$$r_{12p} = \frac{n_2 \cos\Theta_1 - n_1 \cos\Theta_2}{n_2 \cos\Theta_1 + n_1 \cos\Theta_2} = \frac{\tan(\Theta_2 - \Theta_1)}{\tan(\Theta_2 + \Theta_1)}$$

where n_1 and n_2 is the indices of refraction for the first and second material, Θ_1 and Θ_2 are the angles of incidence of the incoming and the refracted ray. On figure 3.3 the reflectance of s and p polarized light is plotted against the angle of incidence. Notice the higher reflectance of s-polarized light compared to p-polarized light. At the Brewster angle, indicated by Θ_B in the figure, no p-polarized light is reflected, and the reflected light is linearly polarized in a direction orthogonal to the plane of incidence. The green line in figure

3.3 is the ratio of the p and s reflectance. When linearly polarized light is reflected from a surface, the difference in reflectance for p and s polarized light will change the direction of the linear polarization state slightly, but it will still be linearly polarized. The other method for polarizing light is to use a polarization filter, which only allow variations in the E-field in one direction. Application of such a filter results in linearly polarized light.

Changing polarization state   The polarization of a light ray can be altered by passing through an optically active or a birefringent material. An optically active material will rotate the direction of polarization, while maintaining the elongated shape of the polarization signature.

In birefringent materials like *Iceland spar* and *mica* a refracted ray is divided into two rays (hence the name birefringent) each with linearly polarized light. An optical axis of the crystal is the direction in which linearly polarized light can pass through the crystal without being split into two beams. The two rays will propagate through the material with different velocities corresponding to two different indices of refraction. The difference of the two indices of refraction is the birefringence Δn of the crystal, due to dispersion this number depends on the wavelength of the passing light.

The incoming light is projected onto the two optical directions of the crystal s and p. Assuming that the light is polarized, it can be described by

$$E_p^{\text{in}}(t) = E_p^0 \cdot \sin\left(\omega \cdot t\right)$$
$$E_s^{\text{in}}(t) = E_s^0 \cdot \sin\left(\omega \cdot t + \phi\right)$$

As both rays do not use the same time to pass the birefringent material, a phase offset θ is introduced. The electrical field of the exiting light will then be

$$E_p^{\text{out}}(t) = E_p^0 \cdot \sin\left(\omega \cdot t\right)$$
$$E_s^{\text{out}}(t) = E_s^0 \cdot \sin\left(\omega \cdot t + \phi + \theta\right)$$

The induced phase offset will change the polarization state of the passed light. Sending polarized light through a half wave plate (offset π) will alter the polarization state of the light. As $\sin(x+\pi) = -\sin(x)$, this corresponds to a reflection of the electrical field along one of the optical axes.

$$E_s^{\text{out}}(t) = E_s^0 \cdot \sin\left(\omega \cdot t + \phi + \pi\right)$$
$$= -E_s^0 \cdot \sin\left(\omega \cdot t + \phi\right) = -E_s^{\text{in}}(t)$$

Figure 3.4 visualizes the effect of a half wave plate on linearly polarized light; gray dashed lines indicate the polarization state of the incoming light (parametric plot of $E_p^{\text{in}}(t)$ vs. $E_s^{\text{in}}(t)$), the red ellipse is
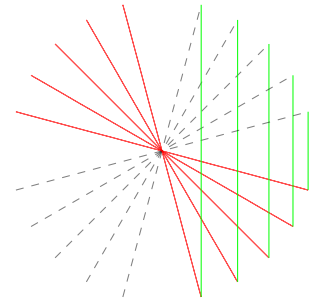

Figure 3.4: *Effect of a half wave plate on linearly polarized light.*

the polarization state of the transmitted light (parametric plot of $E_p^{\text{out}}(t)$ vs $E_s^{\text{out}}(t)$). On the figure five such polarizations is visualized, for matching the corresponding polarization states the green arrows indicate how the major axis of the ellipse is changed. Notice that the polarization of the incoming light is reflected about the x-axis, and that the light is still linearly polarized.

Quarter wave plate How linearly polarized light is affected by a quarter wave plate (offset $\pi/2$) is more complicated. On figure 3.5 the effect of a quarter wave plate on linearly polarized light is visualized. The blue lines on the figure show the major axis of the shown polarization ellipses (red). From the figure two observations on how linearly polarized light is affected by a quarter wave plate can be made: (1) If the incoming linearly polarized light has a polarization axis at a 45° angle to the optical axis of the quarter wave plate, the transmitted light will be circular polarized. (2) At all other polarization angles the major axis of the transmitted light is aligned with the optical axis that are closest. Optical filters which induce a phase offset of $\pi/2$ are denoted quarter

Figure 3.5: *Effect of a quarter wave plate on linearly polarized light.*

ter wave plates and is routinely used to convert linearly polarized light to circularly polarized light and vice versa.

The effect of different phase offsets on linearly polarized light is visualized on figure 3.6. From the figure the following can be concluded:

- For offsets in the range 0° to 60°, the transmitted light is elliptic polarized with a very elongated shape; this light can be used to determine orientation of fluorescent probes.

- When the phase offset approaches 90° the polarization of the transmitted light will be more directed along the optical axes. This result in only two different polarization directions of the illuminating light, which will prevent further analysis of the orientation of the fluorophores.

- Offsets in the range 120° to 180° will have their direction of polarization reflected along one of the optical axes in the crystal. This induces a change in angular direction of the illuminating light, such that a clock wise rotation of the incoming light will be converted to a counter clock wise rotation of the illuminating light.

In general if the incoming light is linearly polarized along one of the optical axes in the birefringent crystal, there is only one polarization of light that passes through the crystal leaving no change in polarization.
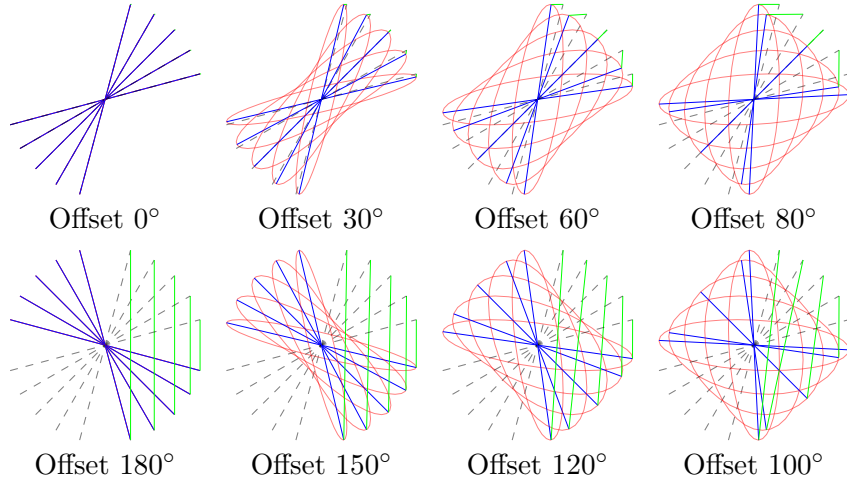
Figure 3.6: *How linearly polarized light is transmitted through a birefringent crystal with a thickness corresponding to a given phase offset. Black lines: original polarization. Red: polarization ellipse of transmitted light. Blue lines: major polarization axis of the transmitted light. Green arrows: Change in major axis of the polarization ellipse.*

3.2 Experimental implications

In the experiments with supported lipid bilayers, the substrate consisted of a slice of mica with unknown thickness. During one experiment the slice thickness is unchanged, but from one experiment to the next the thickness may be changed. As mica is birefringent, variations in slice thickness will alter how the polarization state of the illuminating light is changed during transmission. The induced phase offset δ depends on the thickness d, birefringence $\Delta n(\lambda)$ of mica and the wavelength λ of transmitted light.

$$\delta = \frac{2\pi d \Delta n(\lambda)}{\lambda} \tag{3.1}$$

For mica the dispersion of the two indices of refraction have been measured by Özder *et. al* [25] and are approximated in the interval $500nm$ to $800nm$ by Cauchy's formula. The birefringent wavelength dependence of mica can then be expressed as

$$\Delta n(\lambda) = n_o(\lambda) - n_e(\lambda)$$
$$= 0.006 - 3.983 \cdot 10^3 nm^2/\lambda^2 + 1.0585 \cdot 10^9 nm^4/\lambda^4$$

and is shown on figure 3.7. The polarization of linearly polarized light is seen to be highly distorted by phase offsets near $90°$ (figure 3.6); but how thick a slice of mica does this corresponds to? In a quarter wave plate made of
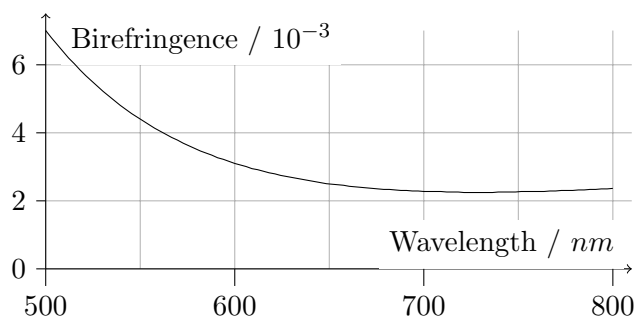
Figure 3.7: *Birefringence of mica.*

mica that works near $540nm$ (excitation wavelength used in the one photon microscope), the thickness of the mica slice can be calculated using formula (3.1) inserting $\delta = \pi/2$. The thickness must then be

$$d_{\lambda=540nm} = 28.2\mu m$$

If the similar thickness is calculated for wavelengths near $780nm$ (excitation wavelength used in the two photon microscope), we get

$$d_{\lambda=780nm} = 84.4\mu m$$

The required thickness of a quarter wave plate is increased by a factor 3 when the wavelength is increased from $540nm$ to $780nm$. The sheets of mica that are used for the experiments are $200\mu m$ thick before they are cleaved; after cleaving the thickness will probably be below $50\mu m$ (an educated guess, as the thickness cannot be measured directly). If a piece of mica is $50\mu m$ thick, it will reflect the polarization direction in the one photon microscope (act like a half wave plate) but will only have a minor distorting effect on polarization in the two photon microscope.

In section 6.5 two observations are commented, they are both caused by the birefringent properties of mica. This kind of distortions of the polarized light have only been observed on the one photon fluorescence microscope.

Chapter 4

Standard image analysis techniques

The subject image analysis covers a set of methods for enhancing images for visual inspection and extracting qualitative and quantitative information from images. The used image processing / analysis methods used in this project are standard methods. Image processing have been used for

- Noise reduction

- background estimation

- image segmentation and

- feature location

The analyzed images are all raster images. A raster image is a set of $n \times m$ locations (pixels) arranged as an array. A value (color) is attached to each of the pixels. Each pixel corresponds to a location in the examined sample and the attached value is a quantity measured at that location. For AFM images the measured quantity is the height of the sample at that location and for fluorescence images the measured quantity is the fluorescence response. A raster image is basically a huge number of measurements performed at a set of discrete locations. In the following the image intensity (the measured value) of location (x, y) will be denoted

$$I(x, y) = \text{Measured value at location } x, y$$

When viewing an image, the measured value should be presented as a color. A color map is a mapping from measured values to colors. For images where only one value are attached to each pixel, a gray scale color map is often used. In a gray scale image bright pixels usually corresponds to high values whereas dark pixels have low values. An example of a gray scale image is shown in figure 4.1a. Programs like Matlab and Mathematica are designed to allow easy access

(a) *Raw image*   **(b)** *Inverted image*   **(c)** *Thresholded image*
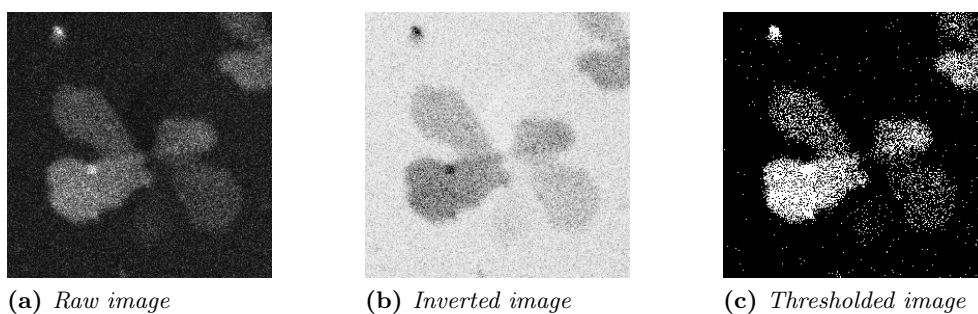
Figure 4.1: *Some point wise image transforms*

to advanced image analysis techniques like edge detection and morphological filters.

Point wise image transforms   The methods in image processing are in principle functions that takes one or more images as input and from the input a new image. The simplest group of image transformations are the point wise image transformations. In a point wise image transform formed image have the same size as the input image(s) and the value of each pixel is determined from the values in the input images at the same pixel. The operations belonging to the point wise transforms includes thresholding and image arithmetics. Image inversion, where dark pixel values are mapped to bright values is an example of a point wise transform and an example is shown in figure 4.1b. Some details may be easier to examine in an inverted image. A GP image, like figure 2.10a, is a more elaborate example of image arithmetics. Another operation is thresholding, in figure 4.1c all the pixels brighter than a specified value are set to one and the rest are set to zero. Point wise image transformations are not able to detect edges, blur areas and similar operations that involves values of neighbor pixels.

4.1   Neighborhood image transformations

By using information from nearby pixels more complex image transforms can be implemented. The neighborhood transformations can be divided into two groups, linear and non linear transformations. A linear transform could be an averaging filter, which blurs an image. Linear transformations can be expressed as spatial convolutions between an image and a suitable kernel. If we denote the image f and the kernel g, the spatial convolution is defined as

$$[f * g](\mathbf{x}) = \sum_{\mathbf{b} \in D_g} f(\mathbf{x} - \mathbf{b}) \cdot g(\mathbf{b})$$

where D_g is the definition domain of g. Usually the origin of g is in the center of the image. Given an arbitrary image and a kernel, the spatial convolution can be computed efficiently using the Fast Fourier Transform. Using the definition of the spatial convolution, all linear filters can now be expressed in terms their kernel.

A kernel for a uniform smoothing filter is shown below. The new pixel value is set to the average value of the 25 pixels in the 5×5 window centered above the pixel. In figure 4.2a the result of applying this filter to the raw image (figure 4.1a) is shown.

$$g_{\text{uniform}} = \frac{1}{25} \begin{pmatrix} 1 & 1 & 1 & 1 & 1 \\ 1 & 1 & 1 & 1 & 1 \\ 1 & 1 & 1 & 1 & 1 \\ 1 & 1 & 1 & 1 & 1 \\ 1 & 1 & 1 & 1 & 1 \end{pmatrix}$$

Unfortunately the effect of this filter depends on the orientation of the feature that should be smoothed, a better solution is to use Gaussian smoothing where the kernel is an approximation of a two dimensional Gaussian distribution, as this will be invariant under rotations. A 5×5 gauss kernel with $\sigma = 1$ is shown below (result visualized in figure 4.2b).

$$g_{\text{gauss}} = \begin{pmatrix} 0.0030 & 0.0133 & 0.0219 & 0.0133 & 0.0030 \\ 0.0133 & 0.0596 & 0.0983 & 0.0596 & 0.0133 \\ 0.0219 & 0.0983 & 0.1621 & 0.0983 & 0.0219 \\ 0.0133 & 0.0596 & 0.0983 & 0.0596 & 0.0133 \\ 0.0030 & 0.0133 & 0.0219 & 0.0133 & 0.0030 \end{pmatrix}$$

In Matlab uniform smoothing and gaussian blurring can be applied using the two commands

```
uniformblur = filter2(ones(5), img);
gausskernel = fspecial('gaussian', 5, 1);
gaussblur = filter2(gausskernel, img);
```

Linear filters can also be used for locating edges in images. The Sobel edge detector is based on the two kernels shown below

$$g_{\text{sobel}}^{\text{vert}} = \begin{pmatrix} -1 & 0 & 1 \\ -2 & 0 & 2 \\ -1 & 0 & 1 \end{pmatrix} \qquad g_{\text{sobel}}^{\text{horz}} = \begin{pmatrix} -1 & -2 & -1 \\ 0 & 0 & 0 \\ 1 & 2 & 1 \end{pmatrix}$$

Where $g_{\text{sobel}}^{\text{vert}}$ estimates the vertical edge strength by approximating the derivative of the image intensity in the horizontal direction and $g_{\text{sobel}}^{\text{horz}}$ locates horizontal edges using a similar approach. In this case the Sobel edge detector is applied to an image blurred with a wide gaussian kernel $\sigma = 5$ (figure 4.2c),

(a) *Uniform 5×5 average*

(b) *Gaussian blur with $\sigma = 1$.*

(c) *Gaussian blur with $\sigma = 5$.*

(d) *Sobel vertical edges.*

(e) *Sobel horizontal edges.*

(f) *Sobel edge strength.*
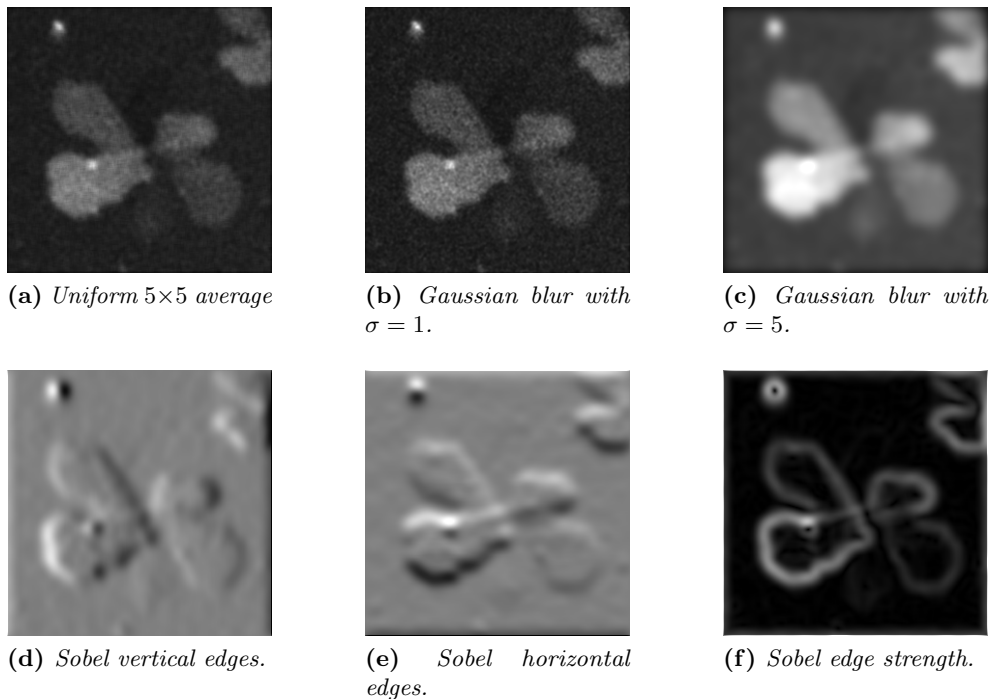
Figure 4.2: *Some neighborhood image transforms*

and the effect of the Sobel filter is shown in figure 4.2d for vertical images and in figure 4.2e for horizontal edges. In Matlab the Sobel filters can be applied to the image `img` using the code shown below.

```
sobelvert = filter2([-1, 0, 1; -2, 0, 2; -1, 0, 1], img);
sobelhorz = filter2([-1, 0, 1; -2, 0, 2; -1, 0, 1]', img);
```

By adding the squared horizontal edge strength to the squared vertical edge strength and taking the square root to the sum the edge strength, of all the pixels in the image, can be determined. The edge strength is shown in figure 4.2f and have been calculated like shown below.

```
sobeledgestrength = sqrt(sobelvert.^2+sobelhorz.^2);
```

Nonlinear image transformations While the linear filters is a useful class of filters, there are many filters that does not belong to the class. The Sobel edge strength is an example of a nonlinear image transformation, other nonlinear transformations include median filtering The median filter takes all image values in a $n \times m$ window, orders them numerically and selects the value in the middle. A median filter preserves the edge location and removes a large fraction of the noise in the image. Median filters with small window sizes

(a) 5×5 *window* **(b)** 10×10 *window* **(c)** 15×15 *window*

Figure 4.3: *Median filters with varying window sizes*

1	1	1
1	**1**	1
1	1	1

(a) 3×3
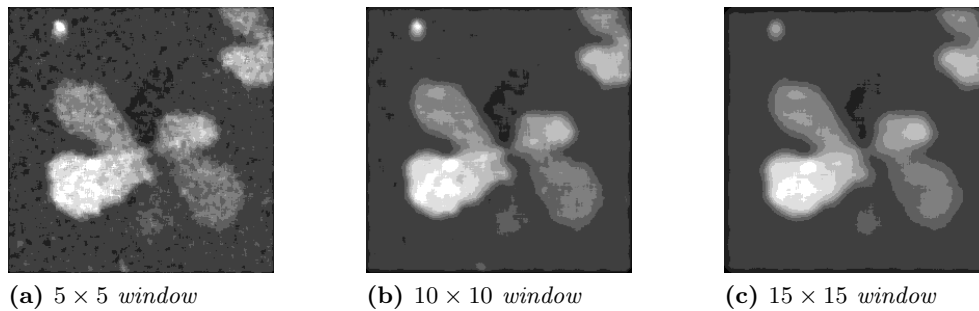*square*

0	1	0
1	**1**	1
0	1	0

(b) 3×3
cross

1	1	1	1	1
1	1	1	1	1
1	1	**1**	1	1
1	1	1	1	1
1	1	1	1	1

(c) 5×5 *square*

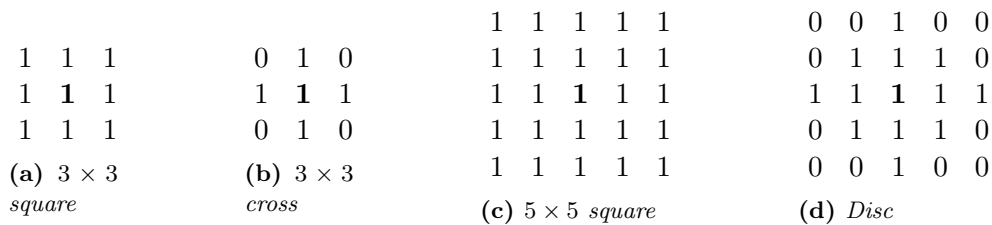|				
0	0	1	0	0
0	1	1	1	0
1	1	**1**	1	1
0	1	1	1	0
0	0	1	0	0

(d) *Disc*

Figure 4.4: *Some structuring elements.*

are often used to remove salt and pepper noise (randomly scattered bright and dark pixels), while median filters with larger windows can be used for background estimation.

4.2 Morphological image processing

Morphological image processing covers a group of nonlinear image filters which are able to use and extract information about structures (morphology) in images[1]. The basic goal of morphological operations is to examine how a structuring elements fits in a certain part of the original image. A structure element is a spatial structure often represented as a binary pattern in a $n \times n$ matrix. Some common structuring elements are shown on figure 4.4.

A basic morphological process is to erode an image with a given structuring element. The erosion process is based on iterative examination of each pixel in the original image, if the structuring element aligned over a specific pixel fits inside objects in the original image it is set to a foreground pixel (white), otherwise is it set as a background pixel (black). Erosion of the image A by the structuring element B is written

$$A \ominus B$$

---

[1]This introduction is based on [56, 57]

(a) *Original*   **(b)** *Erosion*   **(c)** *Dilation*   **(d)** *Morphological*   **(e)** *Closing*
                                                                        gradient

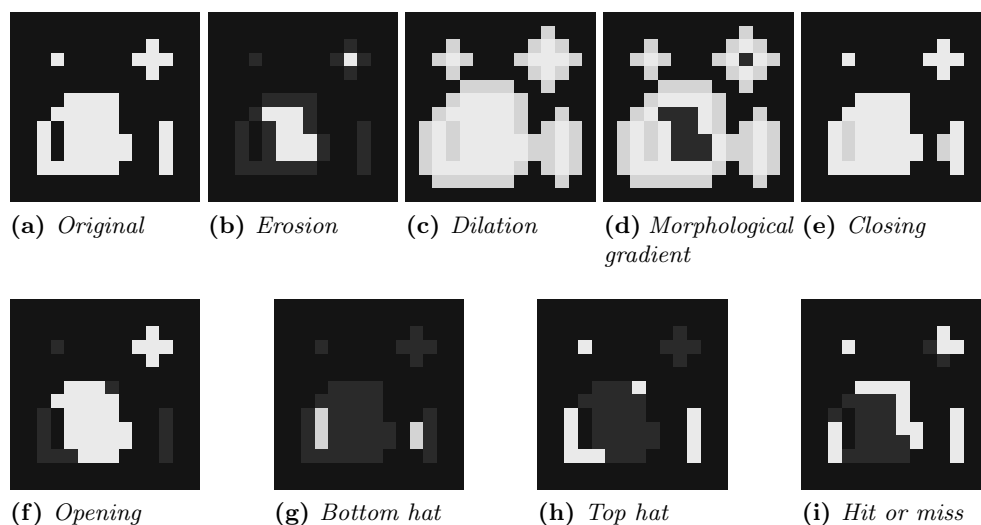**(f)** *Opening*   **(g)** *Bottom hat*   **(h)** *Top hat*   **(i)** *Hit or miss*

Figure 4.5: *Effect of several morphological operations. In all sub figures the original image is shown as a dim shadow with the result of the operations superimposed. A 3×3 cross have been used as the structuring element for all the operations, except for the hit or miss transform.*

The effect of eroding the image in 4.5a with a 3×3 cross shaped structuring element is shown on figure 4.5b. The erosion removes features in the original image that does not fit the structuring element completely, and reduces the area of the bright regions. In general will erosion shrink the object regions and let the background grow.

For all morphological operations, there exists a dual operation. The dual operation Ψ^* can be expressed in terms of the original operation Ψ as shown below

$$\Psi^*(A) = \Psi(A^c)^c$$

For calculating the dual operation to a given operation, the operation should be applied to the complementary image A^c and the result of the operation should then be complemented.

The dual operation to erosion is dilation; a process where the background regions is shrunk and the objects grow. Dilation of image A by the structuring element B is denoted

$$A \oplus B$$

The effect of dilation is shown on figure 4.5c.

Several other morphological operations can be defined using erosion and dilation combined with set operations such as union and intersection. Pixels

that are near the boundary of objects can be found by calculating the *morphological gradient*, which is the difference between the dilated and the eroded image. The morphological gradient image contains these locations where the structuring element does not fit entirely inside the object or the background.

Closing fills holes smaller than the structuring element, but other wise keeps the shape of the original image, and the dual operation *opening* removes objects smaller than the structuring element. Opening $\circ$ and closing $\bullet$ are defined as

$$A \circ B = (A \ominus B) \oplus B$$
$$A \bullet B = (A \oplus (-B)) \ominus (-B)$$

The notation $-B$ means that the structuring element must be reflected around the origin, otherwise opening and closing will not be dual operations for nonsymmetric structuring elements.

Directly related to the morphological operations opening and closing, are the top / bottom hat transforms. The top hat transform is the difference between the original image and the opened image. The top hat transform of an image contains the objects / features that are smaller than the structuring element; similarly does the bottom hat transform contain the holes that are filled during a closing operation and thus are smaller than the structuring element. Examples of the effect of bottom hat and top transforms are shown on figure 4.5g and 4.5h.

For pattern recognition the *hit or miss transform* can be applied. The transform is based on two structuring elements, E for object pixels and F for background pixels and is defined as

$$A \circledast (E, F) = (A \ominus E) \cap (A^c \ominus F)$$

Where $\cap$ is the intersection of two images (the set of pixels that are object pixels in both images). The hit or miss transform locates pixels where the object structuring element E matches object pixels and the background structuring element F matches background pixels. If we want to locate all white pixels with a black pixel as the nearest north east neighbor, the structuring element should be:

$$E = \begin{pmatrix} 0 & 0 & 0 \\ 0 & 1 & 0 \\ 0 & 0 & 0 \end{pmatrix} \qquad\qquad F = \begin{pmatrix} 0 & 0 & 1 \\ 0 & 0 & 0 \\ 0 & 0 & 0 \end{pmatrix}$$

The result of this hit or miss transform is shown in figure 4.5i. By careful selection of the structuring elements, the hit or miss transform can be used to *thin* objects in an image. In the thinning process each object in an image is reduced to a thin line. The thinning operation is applied to figure 4.6a gaining the image shown in figure 4.6b. Thinning can be used to locating center lines
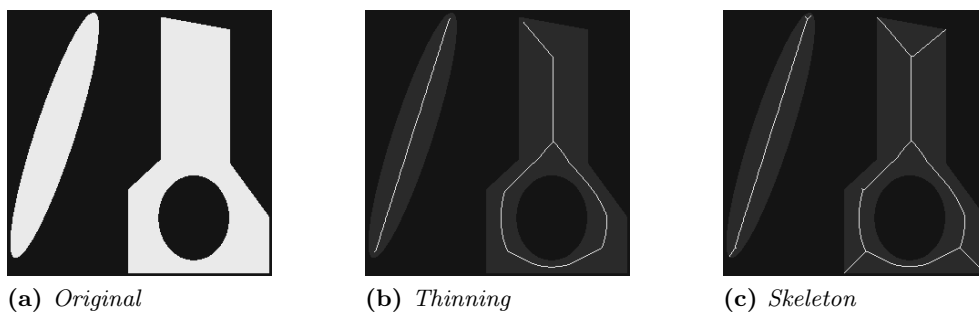
(a) *Original* **(b)** *Thinning* **(c)** *Skeleton*

Figure 4.6: *Effect of the thinning and skeleton morphological operations.*

of elongated objects. After thinning, the hit or miss transform can be used to locating line endpoints. A transform which is closely related to the thinning is skeletonization / medial axis transform.

The described morphological operations are all implemented in the Matlab Image Processing Toolbox and accessible via the `bwmorph` command.

Gray scale morphological transforms The dilate and erode operations defined on binary images can also be applied to gray scale images. For the flat structuring element B, gray scale dilation and erosion are defined by

$$[\delta_B(f)](\mathbf{x}) = \max_{\mathbf{b} \in D_B} f(\mathbf{x} + \mathbf{b})$$

$$[\varepsilon_B(f)](\mathbf{x}) = \min_{\mathbf{b} \in D_B} f(\mathbf{x} + \mathbf{b})$$

Gray scale erosion sets the pixel value of a given location to the minimal pixel value which are located inside the structuring element; dilation takes the maximal value inside the structuring element. The effect of erosion is that the size of bright areas are reduced and that darker areas grow; the effect of dilation is the opposite. On figure 4.7b and 4.7c the effect of gray scale erosion and dilation are shown. Notice that small bright objects are removed during erosion, this effect can be used to estimate the background in a gray scale image.

Gray scale dilation and erosion are also defined for the non flat structuring element B_v:

$$[\delta_{B_v}(f)](\mathbf{x}) = \max_{\mathbf{b} \in D_{B_v}} \{f(\mathbf{x} + \mathbf{b}) + B_v(\mathbf{b})\}$$

$$[\varepsilon_{B_v}(f)](\mathbf{x}) = \min_{\mathbf{b} \in D_{B_v}} \{f(\mathbf{x} + \mathbf{b}) - B_v(\mathbf{b})\}$$

Gray scale dilation and erosion can be used for simulation or removal of artifacts caused by blunt AFM tips, see section 2.5. Otherwise these morphological transformations are seldom used.
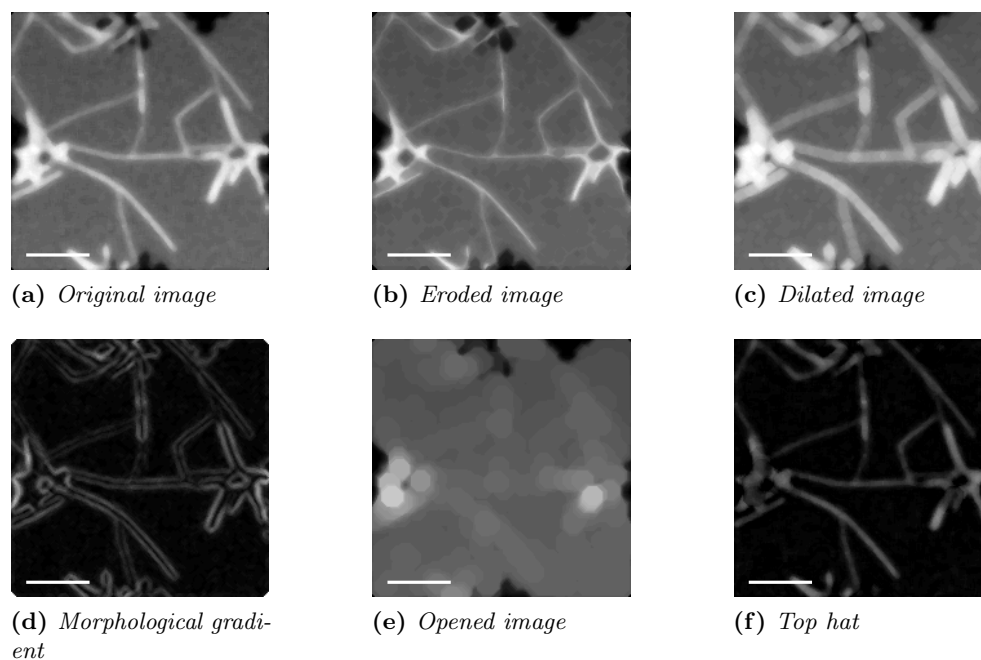
(a) *Original image*

(b) *Eroded image*

(c) *Dilated image*

(d) *Morphological gradient*

(e) *Opened image*

(f) *Top hat*

Figure 4.7: *Some gray scale morphological transforms. For performing erosion, dilation and morphological gradient a disk shaped structuring element with radius 2 have been used; for the opening and the top hat transform a disk with radius 8 were used. $10\mu m$ scale bar inserted.*

By opening a gray scale image with a (large) structuring element, bright features smaller than the structuring element are removed from the image leaving an estimate of the background (figure 4.7e), if the background estimate is subtracted from the original image only the bright features smaller than the structuring element will survive (figure 4.7f), this is the gray scale version of the top hat transformation.

4.3 End point tracking

In section 6.8 the growth of stripe phase domains are examined. For extracting information on the growth velocity of stripe domains, the location of domain endpoints should be tracked over time. The tracking algorithm consists of first locating all end points in the available images and thereafter locate corresponding end points. The algorithm for locating end points is described below, and the intermediate results are shown in figure 4.8. The algorithm proceeds as follows:

1. Load image to analyze

```
img = imread('filename.tif');
```

2. Apply a 3×3 median filter. The purpose of this filter is to remove noise.

```
imgtt = medfilt2(imgt);
```

3. Blur the image using a gaussian kernel.

```
gaussfone = fspecial('gaussian', 9, 1);
imgttt = filter2(gaussfone, imgtt);
```

4. Open the image using a large $(30px)$ structuring element. This gives an estimate of the image background.

```
imgtttopened = imopen(imgttt, strel('disk', 30));
```

5. Correct the illumination of the blurred image by subtraction of the opened image. The result is a top hat transform, where the small features of the image are kept while larger features have been removed.

```
hat = imgttt - imgtttopened;
```

6. Pixels with a value larger than a threshold are set to object pixels. Several threshold values have been tested, but the best results were obtained for values near 4, which is used here.

```
bw = hat > 4;
```

7. The skeleton of the object regions is calculated. The end points of the skeleton is the located end points.

```
skel = bwmorph(bw, 'skel', 'inf');
```

The algorithm is able to reliably locate end points of thin and bright regions. For thin and elongated regions the deviation from located end points to the real end points will be below 3 pixels. For thicker regions the located end points are not as precisely located.
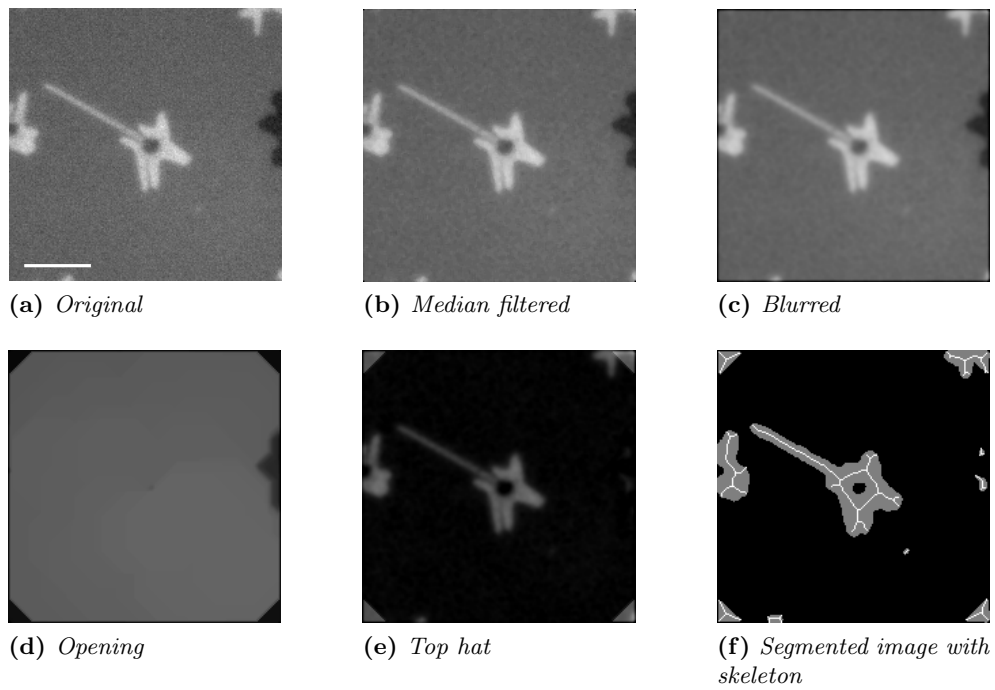
(a) *Original*

(b) *Median filtered*

(c) *Blurred*

(d) *Opening*

(e) *Top hat*

(f) *Segmented image with skeleton*

Figure 4.8: *How endpoints are located.* 10μm *scale bar.*

Chapter 5

Lipid orientation in membrane gel domains

Inside a lipid bilayer the lipid molecules can be more or less ordered. If the temperature of the bilayer are above the main phase transition and thus in the fluid phase, each lipid molecule will on average be oriented along the bilayer normal **n**, this direction is subject to thermal fluctuations. When the temperature is decreased to below the main phase transition and the bilayer is in the gel phase, the acyl chains of the lipid molecules will be stretched. The lipid molecules form a hexagonal close packed structure where the acyl chains are tilted by an angle ρ relative to **n**[58].

In lipid bilayers composed of only a single lipid type, coexisting domains occurs only at narrow temperature ranges. By mixing two diacylphosphatidyl-cholines with different acyl chain lengths or saturation the phase coexistence region is broadened significantly, this broadening can be observed using calorimetry[13]. Coexisting membrane phases are seen in both GUV's and cell membranes. The shape of such domains have been investigated using two–photon microscopy[59, 60]. But no investigation of the orientation of lipid molecules inside these phase domains were conducted. This chapter investigates the possibility of differences in the lipid orientation (texture) inside gel domains.

For examining this experimentally microscopic methods that can detect changes in lipid orientation must be applied. As the interaction between linearly polarized light and an oriented fluorophore depends on the angle between the electrical field **E** and the transition dipole **p** of the fluorophore, microscopic methods based on polarized light can generate contrast based on the orientation of lipid molecules. Two–photon polarization microscopy have been used for examining the gel domains in supported lipid bilayers composed of DOPC and DPPC in an equimolar ratio. The lipid bilayers have been stained with Laurdan. Laurdan have no preference for the gel or fluid phase and partitions equally in the two phases; hence coexisting phase

domains cannot be discriminated using only the fluorescence intensity. Phase domains can be visualized by examining the spectrum of the emitted light, as the emission spectrum of Laurdan depends on the water concentration near the fluorophore[43]. Laurdan molecules in gel domains have a blue shifted emission spectrum compared to Laurdan molecules in the fluid phase which have a red shifted emission spectre.

By using linearly polarized light, orientation of the transition dipole in the fluorophore can be measured. A Laurdan molecule embedded in a lipid bilayer have the transition dipole aligned parallel to the acyl chains in the lipid bilayer. The angle between $\mathbf{E}$ and $\mathbf{p}$ is denoted the *azimuth* angle ϕ. By rotating the direction of the polarization plane of the excitation light, the ϕ can be varied. As the fluorescence intensity varies as $\propto \cos(\phi)^4$, changes in the fluorophore orientation can be detected by intensity changes inside the gel domain.

In the used experimental setup, the excitation light propagates parallel to the lipid bilayer normal $\mathbf{n}$ and the electrical field of the linearly polarized light is perpendicular to $\mathbf{n}$. In the acquired images the orientation of $\mathbf{E}$ is described by the angle θ; $\theta = 0°$ corresponds to the up/down direction in the image and for increasing values of θ the polarization orientation are rotated counter clockwise as indicated in figure 5.1.

Figure 5.1: *How electrical field orientation are described.*

For measuring variations in the fluorescent intensity, a sequence of images were acquired. From one image to the next in the sequence the polarization orientation were increased by a fixed amount, such that a full rotation of the polarization orientation were achieved.

In the fluid phase, the lipid acyl chains orientation fluctuates isotropically resulting in a fluorescent signal independent of the polarization angle. This is not the case in the gel phase, where the lipid acyl chains are ordered. The strength of the fluorescent signal from a fluorophore embedded in the gel phase depends on the tilt angle ρ and the azimuth angle ϕ

$$I(\rho, \phi) \propto \sin(\rho)^4 \cos(\phi)^4 \tag{5.1}$$

If the transition dipole of the fluorophore is oriented parallel to the bilayer normal ($\rho \simeq 0°$) the probability of exciting Laurdan will be near zero resulting in no expected fluorescence. In the gel phase of an equimolar DOPC / DPPC mixture the lipid acyl chains will be tilted by $\rho = 17°$ relative to $\mathbf{n}$ [61]. This tilt angle should be sufficient to ensure a non zero fluorescence signal from the gel phase of the bilayer, and this signal is now highly sensitive to changes in the polarization angle.
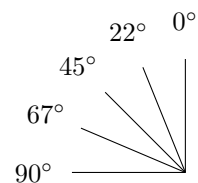
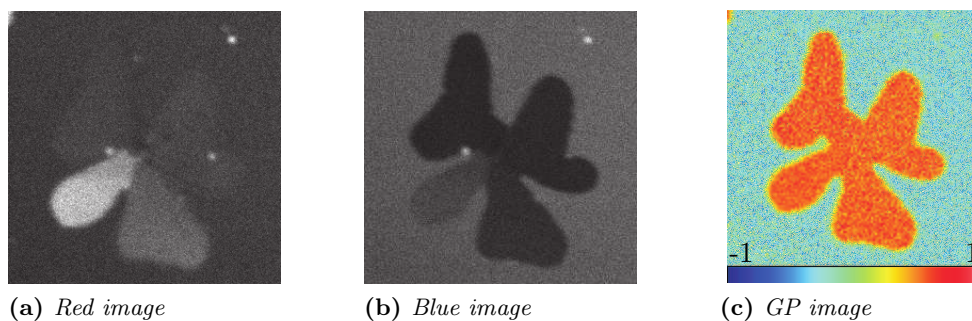**(a)** *Red image* **(b)** *Blue image* **(c)** *GP image*

Figure 5.2: *Generalized polarization image of a gel domain.*

5.1   Qualitative observations

The investigation of lipid orientation in membrane gel domains have been conducted in collaboration with Uffe Bernchou and Jonathan Brewer. Initially the phase coexistence of gel and fluid phases are examined using the spectral properties of Laurdan. The emission spectrum of Laurdan depends on the amount of water near the fluorophore, Laurdan embedded in a fluid phase are more exposed to water compared to Laurdan embedded in a gel phase. This results in a red shift of the emission for Laurdan in the fluid phase. See section 2.4.2 for more information on Laurdan. The general polarization GP is a measure of the ratio of red to blue light introduced by [62]. The GP function is defined as

$$GP = \frac{I_B - I_R}{I_B + I_R} \tag{5.2}$$

In figure 5.2a and 5.2b the images acquired from the red and blue channels respectively are shown. From these two image the GP image can be constructed using equation (5.2). The GP image and the related intensity histogram are also shown in figure 5.2. High values of the GP function corresponds to membrane regions with a solid character and low values corresponds to a liquid character. In figure 5.2 it is evident that only two distinct environments are experienced by the fluorescent probe. The images in figure 5.2 were acquired using linearly polarized light, this have no effect on the fluorescent intensity in the fluid domain but variations in the fluorescent intensity inside the ordered gel domain can be observed. These intensity variations are interpreted as a difference in the molecular fluorophore orientation within the domain. As the fluorophore orientation and the tilt orientation are nearly identical in the gel phase, this interpretation means that differences in the tilt orientation are observed. Changes in the fluorophore orientation will change the azimuth angle ϕ thus altering the fluorescent intensity as described by equation (5.1). The combination of polarization two photon microscopy and the GP image makes
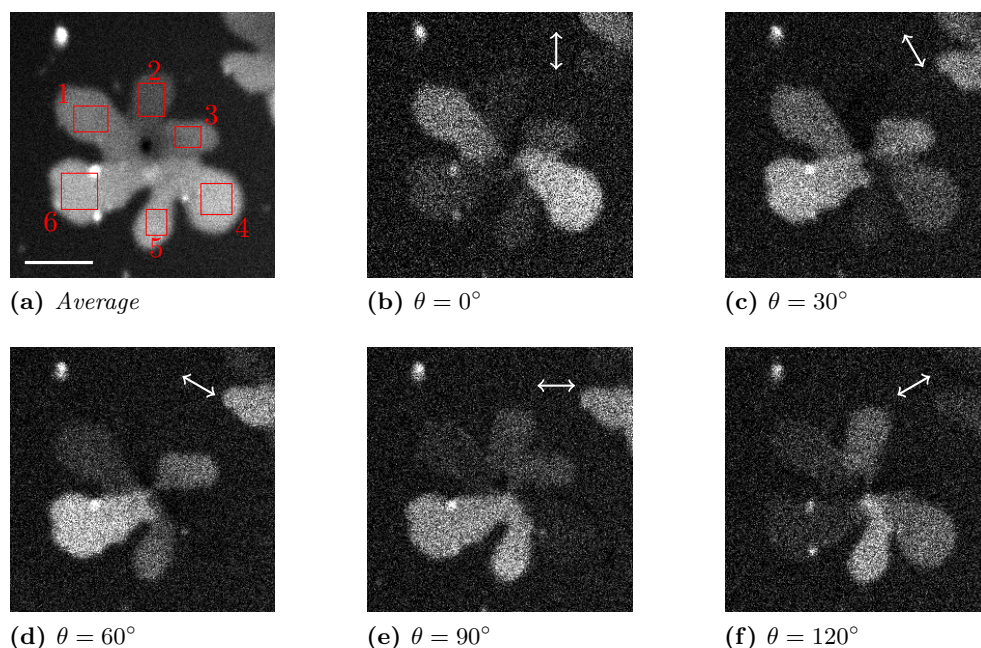
(a) *Average*   **(b)** $\theta = 0°$ **(c)** $\theta = 30°$

(d) $\theta = 60°$ **(e)** $\theta = 90°$ **(f)** $\theta = 120°$

Figure 5.3: *Domains light up when the polarization is altered. The direction of the electrical field of the photons are indicated by the arrow. $5\mu m$ scale bar inserted.*

it possible to discriminate between different membrane phases and the texture within a single phase.

In figure 5.2 at least two areas inside the gel domain with different fluorescence intensity can be located, the orientation of the fluorophore in these two areas must differ. For probing the orientation of the fluorophore, the direction of the linearly polarization is varied of the incoming excitation light while the sample are kept at a fixed orientation. When the direction of **E** is varied the azimuth angle ϕ will be changed to, inducing intensity variations in the fluorescent signal. These intensity variations are quantified by acquiring one image changing the polarization direction by $\Delta\phi = 10°$ acquire a new image and continue until images corresponding to a full rotation of the polarized light have been collected. On figure 5.3 an average image and five individual images from such a collection of images are shown. In the image sequence six distinct sub domains can be distinguished.

5.2   Fluorescence intensity variations

The fluorescence intensity in each of the six sub domains is seen to vary periodically with two intensity peaks during a full rotation. The mean intensity
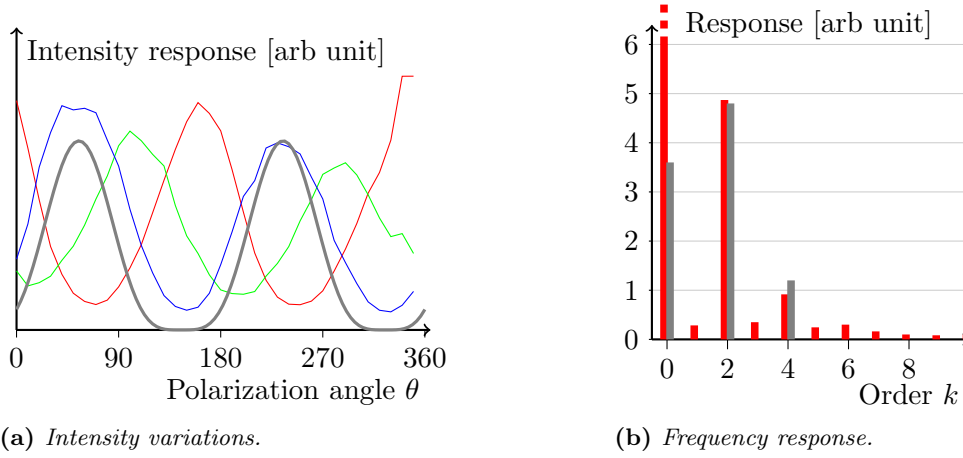
(a) *Intensity variations.*

(b) *Frequency response.*

Figure 5.4: *Observed variations in fluorescence intensity compared with the expected variations.*

of a region in the image sequence can be plotted as a function of the polarization angle, such a plot is shown on figure 5.4a. The red, green and blue lines corresponds to intensity variations in three distinct sub domains. The measured intensities can all be modelled as periodic functions with two intensity maxima during a full rotation.

The expected angular dependency on the fluorescence intensity is given by equation 5.1; for a fixed value of ρ this dependence is reduced to $\cos^4$ of the azimuth angle. If the lipid fluorophore is oriented along the θ_0 direction, the fluorescent intensity should vary as

$$\text{FI}(\theta) \propto \cos(\theta - \theta_0)^4 \tag{5.3}$$

Where θ are the orientation of the used polarization. On the figure, the expected fluorescence intensity is shown as a gray line, the used fluorophore orientation were $\theta_0 = 55°$. Except for horizontal and vertical offsets the shape of the expected fluorescence intensity is found to match the three measured intensity variations.

The similarity between the measured intensity variations and the expected $\cos^4$ dependence can also be depicted using Fourier decomposition. The $\cos^4$ variation can be written as

$$\cos^4 \phi = \frac{3}{8} + \frac{1}{2}\cos 2\phi + \frac{1}{8}\cos 4\phi \tag{5.4}$$

these coefficients ($\frac{3}{8}$, $\frac{1}{2}$ and $\frac{1}{8}$) can be compared to the coefficients obtained from the Fourier transform of a measured intensity variation. In figure 5.4b the two sets of coefficients are compared visually (scaled such that the $k = 2$ responses are identical). Neglecting the average term $k = 0$, strong responses

Domain	A	θ_0 [°]	I_{bg}
1	2.73	6.0	1.57
2	2.49	122.5	0.93
3	3.40	40.2	1.14
4	6.63	163.2	1.27
5	4.34	105.4	1.82
6	6.10	55.1	1.35

(a) *Fit to equation* (5.5).

Domain	I_0	θ_0 [°]	σ [°]
1	6.92	6.3	38.7
2	4.96	123.1	32.4
3	6.45	41.3	31.1
4	9.92	162.4	24.2
5	9.18	105.7	34.0
6	9.74	55.5	26.4

(b) *Fit to equation* (5.6).

Table 5.1: *Tilt orientation obtained by nonlinear fitting to the measured fluorescence intensity.*

for $k = 2$ and $k = 4$ are found for the measured intensity (red markings) indicating a periodic function with two maxima pr rotation. The same two responses $k = 2$ and $k = 4$ are found in the $\cos^4$ signal, with comparable response strengths.

5.3 Estimate of average fluorophore orientation using nonlinear fitting

The fluorophore orientation in each of the six sub domains seems to be homogeneous. We will try to estimate the average fluorophore orientation inside the six marked regions in figure 5.3a by performing a non linear fit. For each area equation 5.5 were fitted to the variation in average fluorescence intensity (see figure 5.4a). The function used for the fitting is a combination of the expected fluorescence intensity as a function of the polarization orientation and a background term.

$$\text{FI}_{\text{fit}}(\theta) = A \cdot \cos(\theta - \theta_0)^4 + I_{bg} \tag{5.5}$$

If a *least squares* fitting procedure like the Levenberg–Marquardt algorithm [63, 64] are used, the obtained fluorophore orientation for the six marked regions in figure 5.3a is shown in table 5.1a. The difference in orientation between two neighbour sub domains are close to but not exactly 60°. As the value of θ_0 have to be determined in the fitting procedure, nonlinear optimization techniques must be applied. The issue of such nonlinear techniques is that they require a suitable initial guess of the parameters that should be fitted; otherwise a local minima different from the best fit might be found resulting in flawed results.

The reason for including the background term is that the measured fluorescence signal could have been added to another static background signal. If all of the measured fluorescence intensity originates from the fluorophore, the

background term cannot be justified. For a sample where all the fluorophores are oriented in the direction θ_0 the fluorescence intensity will vary between no signal at all to the full signal by rotating the polarization orientation $90°$. If the fluorophore orientation is Gaussian distributed with mean θ_0 and standard deviation σ, the fluorescence intensity will follow the formula

$$
\begin{aligned}
F(\theta) = \frac{3I_0}{8} + \frac{I_0}{2} \cos(2\theta - 2\theta_0) \cdot \exp\left(-2\sigma^2\right) \\
+ \frac{I_0}{8} \cos(4\theta - 4\theta_0) \cdot \exp\left(-8\sigma^2\right)
\end{aligned}
\tag{5.6}
$$

where σ is the standard deviation of the fluorophore orientation measured in radians. The formula is derived in appendix A. By performing a non linear fit of function 5.6 to the measured fluorescence intensity, both the average fluorophore orientation and the standard deviation of the fluorophore distribution can be determined. In table 5.1b the obtained values are shown. The two nonlinear fits for equation (5.5) and (5.6) obtain similar fluorophore orientations. The determined standard deviation of the fluorophore orientation distribution were $\sim 30°$. Notice that this is an upper bound, if the orientation distribution of the fluorophore were wider that $\sigma \sim 30°$ it would not be able to generate the observed intensity variations. Another mechanism that could reduce the observed intensity variations is if the illuminating light is not linearly polarized. During the image acquisition the lipid bilayer were illuminated through a slice of mica, that was used as the solid support. This piece of mica will most likely have altered the polarization state of the illuminating light from a linear polarisation to an elongated elliptical state.

5.4 Estimate of fluorophore orientation using the Fourier transform

The average fluorophore orientation can also be determined using Fourier coefficients. The idea is to compute a discrete Fourier coefficient of order γ for all pixels in an image, where the set of values are the pixel intensities acquired with different polarization orientations.

$$
\tilde{I}_\gamma^{x,y} = \frac{1}{N} \sum_{n=0}^{N-1} I_n^{x,y} \exp\left(\frac{-i2\pi\gamma n}{N}\right)
\tag{5.7}
$$

The expected $\cos^4$ angle dependence on the fluorescent intensity can be rewritten using trigonometric identities, revealing the following

$$
\cos(\theta - \theta_0)^4 = \frac{3}{8} + \frac{1}{2} \cos(2\theta - 2\theta_0) + \frac{1}{8} \cos(4\theta - 4\theta_0)
$$

The discrete Fourier coefficients of order $k = 2$ and $k = 4$ will thus contain information on the fluorophore orientation θ_0. But how can this information be

extracted from $X_{k=2}$? Lets calculate $\tilde{I}^{x,y}_{\gamma=2}$ given that the intensity of pixel x, y varies like $\cos(2\theta - 2\theta_0)$ ($\theta = n\frac{2\pi}{N}$ to ensure a full rotation in N measurements)

$$I_n^{x,y} = \cos\left(\frac{4n\pi}{N} - 2\theta_0^{x,y}\right)$$

$$\tilde{I}^{x,y}_{\gamma=2} = \frac{1}{N} \sum_{n=0}^{N-1} \cos\left(\frac{4n\pi}{N} - 2\theta_0^{x,y}\right) \exp\left(\frac{-i2\pi\gamma n}{N}\right)$$

The cosine is expressed in terms of two complex exponentials and then some terms will cancel each other.

$$= \frac{1}{2N} \sum_{n=0}^{N-1} \left[\exp\left(\frac{i4n\pi}{N} - 2i\theta_0^{x,y}\right) + \exp\left(\frac{-i4n\pi}{N} + 2i\theta_0^{x,y}\right)\right] \exp\left(\frac{-i4\pi n}{N}\right)$$

$$= \frac{1}{2N} \sum_{n=0}^{N-1} \left[\exp\left(-2i\theta_0^{x,y}\right) + \exp\left(2i\theta_0^{x,y} + \frac{-i8n\pi}{N}\right)\right]$$

$$= \frac{1}{2N} \sum_{n=0}^{N-1} \exp\left(-2i\theta_0^{x,y}\right) + \frac{1}{2N} \sum_{n=0}^{N-1} \exp\left(2i\theta_0^{x,y} + \frac{-i8n\pi}{N}\right)$$

The second sum are zero, as it corresponds to integrating a periodic function over a whole number of oscillations.

$$= \frac{1}{2} \exp\left(-2i\theta_0^{x,y}\right)$$

If $\tilde{I}^{x,y}_{\gamma=2}$ have been calculated for a single pixel, the corresponding fluorophore orientation can be determined by

$$\theta_0^{x,y} = \frac{-1}{2} \arg\left(\tilde{I}_2^{x,y}\right) \tag{5.8}$$

where $\arg(c)$ is the argument of the complex number c.

On figure 5.5a small lines are superimposed as direction indicators (directors) on a background image. The image behind is an average of the analyzed image sequence. On the figure only a small part of the image is shown for visualizing the directors of single pixels. The length of the directors are proportional to the magnitude of $\tilde{I}_2^{x,y}$. This magnitude is also related to the certainty of the determined fluorophore orientation, a large value indicates a well defined direction whereas low values indicates a large uncertainty in the determined direction. Notice how the length of the directors are decreased as we go from being inside the gel domain (right side of 5.5b) to the fluid domain. The similar orientation (small deviations from the average direction) of the determined fluorophore orientation inside the gel domain indicates that the determined director orientations are accurate. If the whole image were
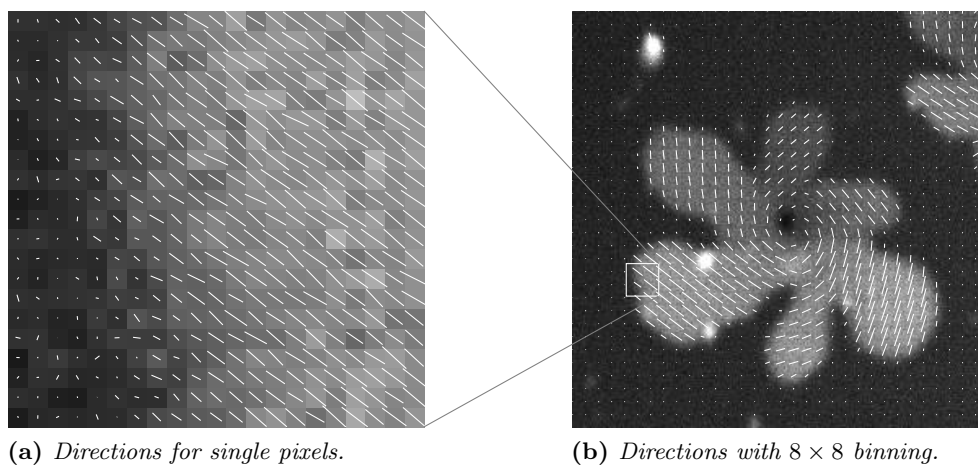
(a) *Directions for single pixels.*   (b) *Directions with 8×8 binning.*

Figure 5.5: *Superimposed directions.*

drawn with all the directors it would be impossible to locate the individual line segments. For presenting the calculated fluorophore orientation of the whole image in figure 5.5b, the number of directors have been reduced by binning. For each group of 8×8 pixels, the average value of $\tilde{I}_2^{x,y}$ are determined and the corresponding director is superimposed on the image. Six distinct sub domains can be located.

5.5 Director deviation estimates

The fluorophore orientation can be calculated from the second order discrete Fourier component $\tilde{I}_2^{x,y}$ using equation (5.8). The oriental homogeneity of the superimposed directors in figure 5.5a indicates that the determined orientation must be quite accurate, as they would otherwise have been more or less randomly oriented. For later analysis of the determined orientations it could be important to have an estimate of the intrinsic uncertainty in the determined orientation. One method for determining the standard deviation of the calculated orientation is to analyze a set of calculated orientations based on the same fluorophore orientation. If we assume that the fluorophore orientation inside a sub domain are exactly equal, a region of pixels inside such a sub domain can be analyzed and the determined fluorophore orientation of each pixel can be compared to the overall fluorophore orientation inside the region. A histogram of the determined fluorophore orientation for 1296 pixels is shown on figure 5.6. A large fraction $\sim 80\%$ of the determined orientation lie in the interval between $65°$ and $85°$, this indicates that the determined orientation is correct within $\pm 10°$. For a more quantitative description, the mean and standard deviation of the determined orientations have been computed. The
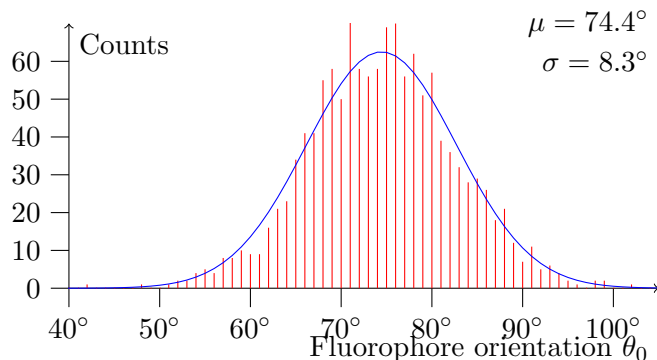
Figure 5.6: *Histogram of determined fluorophore orientations in a region inside a sub domain. The region marked 6 in figure 5.3a is the data source for this histogram.*

computed values $\mu = 74.4°$ and $\sigma = 8.3°$ have been used to superimpose a normal distribution on the histogram. The drawbacks of this method are that it can only be used to estimate the orientation distribution in an area with homogeneous fluorophore orientations and it gives no hint on how the orientation uncertainty depends on the parameters that can be influenced by the experimenter like exposure time and number of images with altered polarization orientations.

The width σ_{meas} of the measured fluorophore orientation distribution, can be expressed in terms of

$\sigma_{\mathbf{photon}}$ standard deviation of the determined orientation, which is caused by photon statistics, see next subsection

$\sigma_{\mathbf{fluoro}}$ standard deviation of the real fluorophore orientation distribution

using the formula (assuming gaussian error distribution)

$$\sigma^2_{\mathrm{meas}} = \sigma^2_{\mathrm{photon}} + \sigma^2_{\mathrm{fluoro}} + \ldots \tag{5.9}$$

Currently we do not know if there is other contributions to the uncertainty, this is marked by the . . . As we know that $\sigma_{\mathrm{meas}} = 8.3°$ from the measured orientation distribution, this must the upper limit for the uncertainty in the determined orientation caused by the measurement method. For estimating the magnitude of σ_{photon} and how it depends on the number of acquired images and the exposure time other methods must be applied.

5.5.1 Estimates from Monte Carlo simulations

The relation between the orientation uncertainty and the setting that can be influenced by the experimenter: signal strength and number of images acquired
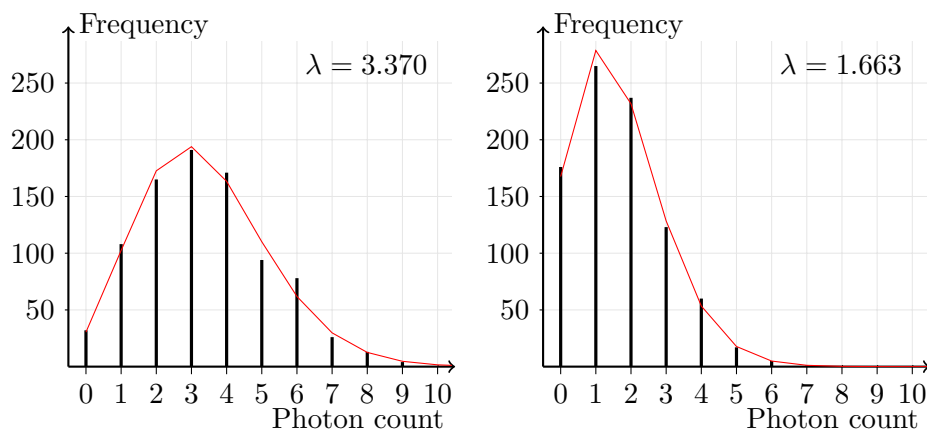
Figure 5.7: *Photon statistics compared to mathing Poisson distribution. The statistics are acquired from area 1 which is marked in figure 5.3 at polarization orientations $\theta = 0°$ and $\theta = 90°$.*

with different polarization orientations, can be examined using Monte Carlo simulation methods. Monte Carlo methods are based on performing a sequence of virtual experiments where the input are randomized and afterward analyze the distribution of the experimental outcome. The randomization in these virtual experiments is simulated through a random number generator that can draw values from a Poisson distribution with a known mean value. The Poisson distribution is chosen as photon emission follows this distribution. In figure 5.7 the observed photon statistics from region 1 in figure 5.3a is shown for two different orientations of the linearly polarized light. The black spikes are the measured frequencies. From the observations the average number of collected photons can be calculated, from this value combined and the total number of observations the expected Poisson distribution, drawn in red, can be compared to the observed frequencies. The observed photon statistics is seen to follow the Poisson distribution.

In the virtual experiments the following signal will be our reference signal:

$$\text{pureSignal}(\theta) = S \cdot \cos(\theta - \theta_0)^4 \tag{5.10}$$

where S is the strength of the artificial signal and θ_0 is the fluorophore orientation. This signal is plotted in figure 5.8 with a red curve, the values used to plot the curve are $S = 8$ and $\theta_0^{\text{orig}} = 40°$. The virtual experiment consists of sampling this signal at N evenly spread locations and then to estimate the fluorophore orientation. As the number of emitted photons follow a Poisson distribution, this distribution is used in the virtual experiments for introducing the random sampling that is required.

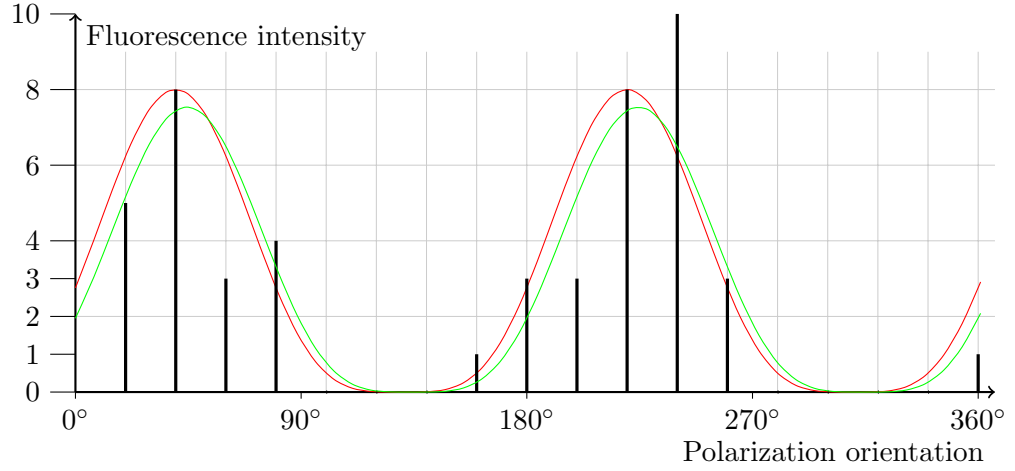In this example the signal is sampled at $N = 18$ locations. At the first

Figure 5.8: *Graphical representation of a simulated experiment in the Monte Carlo simulation. Red curve is the pure signal. Thick black lines are the measured fluorescence intensities. Green curve is the approximated pure signal which is determined from the measured values.*

sampling location, $\theta = 360°/18 = 20°$, the pure signal will be

$$8 \cdot \cos(20° - 40°)^4 = 6.2378 \tag{5.11}$$

The measured fluorescence intensity be a number drawn from a Poisson distribution with mean value 6.2378, in this example the drawn value were 5. For each of the N locations, such a sampling were performed and the result is shown in figure 5.8 as thick black lines. For reference the "measured" intensities were

5 8 3 4 0 0 0 1 3 3 8 10 3 0 0 0 0 1

From this sequence the second Fourier coefficient is calculated using equation (5.7)

$$\tilde{I}_{\gamma=2} = 0.0331 - 1.8838i \tag{5.12}$$

The fluorophore orientation can then be determined using equation (5.8) and the signal strength can be approximated by

$$\theta_0 = \frac{-1}{2} \arg\left(\tilde{I}_{\gamma=2}\right) = 44.4974° \tag{5.13}$$

$$S^{\mathrm{meas}} = 4 \cdot \left|\tilde{I}_{\gamma=2}\right| = 7.5365 \tag{5.14}$$

From these two values the reconstructed signal is plotted as the green curve in figure 5.8. Notice the phase difference between the red and green curves, this
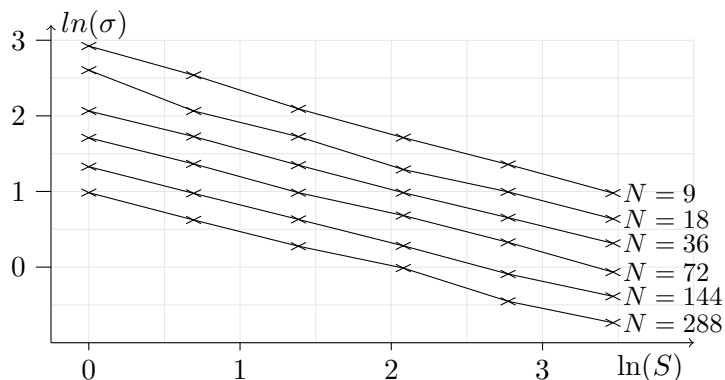
Figure 5.9: *How the uncertainty of the determined fluorophore orientation, σ, depends on the number of images, N and the signal strength, S. The plot indicates a power law relation between the three quantities, a linear fit reveals the relation $\sigma \sim 53°/\sqrt{N \cdot S}$.*

phase difference is the error in the determined fluorophore orientation, in this case it is $\theta_0 - \theta_0^{\mathrm{orig}} = 4.4974°$. By repeating this experiment 1000 times the uncertainty of the determined orientation can be estimated to $\sigma = 3.6°$.

A sequence of such simulations have been performed examining the impact of changing the number of observations N or the signal strength on the uncertainty. N values of 9, 18, 36, 72, 144 and 288 have been used in combination with signal strengths of 1, 2, 4, 8, 16 and 32. The functional dependency of N and S on σ have been visualized on figure 5.9. As expected the uncertainty σ will decrease if the signal strength S or the number of samples N increases. The straight lines in the plot, combined with the fact that a double logarithmic coordinate system were used, tells us that there is a power law relation between S, N and σ. By fitting a function of the form

$$\log(\sigma) = a \log(S) + b \log(N) + c \tag{5.15}$$

to the data, the following power law behaviour were found

$$\sigma(N, S) \simeq 53° \cdot N^{-0.52} \cdot S^{-0.52} \sim \frac{53°}{\sqrt{N \cdot S}} \tag{5.16}$$

As the signal strength S is the expected number of photons observed by a single pixel when the polarization orientation is parallel to the fluorophore orientation, S must be proportional to the exposure time. The total exposure time will thus be proportional to the product of N and S. The uncertainty is then inverse proportional to the square root of the total exposure time. The signal to noise ratio of numbers originating from a Poisson process are given by the square root of the expected number: $\sqrt{S}$. The uncertainty can then be

expressed as

$$\sigma(N, S) \sim \frac{53°}{\text{SNR}\sqrt{N}} \tag{5.17}$$

Finally the estimate of the deviation of the determined fluorophore orientation from a homogeneous patch and the Monte Carlo model can be compared. The standard deviation obtained from the homogeneous patch were $\sigma_{patch} = 8.3°$, this value should be compared to the estimate from the Monte Carlo simulation with $\sigma(N = 36, S = 10.5) = 2.7°$. The used signal strength is an estimate of the average number of photons observed in the examined area when it is at maximum intensity. The simulated deviation is significantly smaller than the one determined from the assumed homogeneous area, this could indicate that the assumption of a homogeneous fluorophore orientation in the selected area were invalid.

## 5.6 Color encoding instead of directors

In figure 5.5a the calculated direction were indicated for each pixel by superimposing small lines aligned in the determined fluorophore orientation. This works fine in small images where each director can be sufficiently large such that the directional information can be read precise and easily. For larger images where the orientation of each pixel should be visualized this approach becomes futile and alternatives must be sought.

As all the relevant information are stored in the second Fourier component calculated for all pixels, the real and imaginary values of this could be exported as images. Two such images are shown in figure 5.10. By combining the two images the boundaries of the six sub domains can easily be located, unfortunately it is very difficult to estimate the fluorophore orientation belonging to each domain. A first attempt to combine these two images could be in a color image where the red channel represents the real value and the green channel the imaginary value of $\tilde{I}_2$. Such an image is shown in figure 5.10c where the blue channel is set to zero, this introduces a yellow color in the image. This can be remove by setting the blue channel to 0.5, this is shown in figure 5.10d. Now only one image are required to identify all the six sub domains and the boundaries separating them. The color representation used in the last image show the perspective of encoding the orientation information in color codes. But can other more suitable color encoding be found?
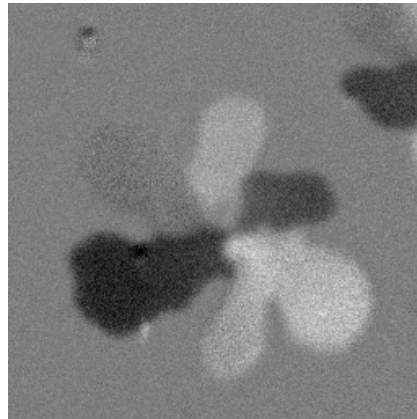
The information in $\tilde{I}_2$ consists of complex numbers. Any complex number can be expressed in either Cartesian or polar coordinates:
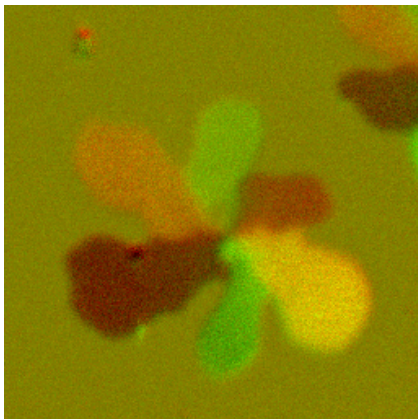
$$c = |c| \exp\left[i \arg(c)\right] \tag{5.18}$$

If $\tilde{I}_2$ is expressed in polar coordinates, the argument $\arg(\tilde{I}_2)$ contains information about the determined orientation and the modulus $|\tilde{I}_2|$ contains information about the certainty of the determined orientation.
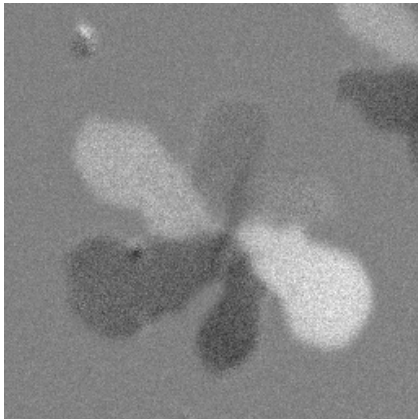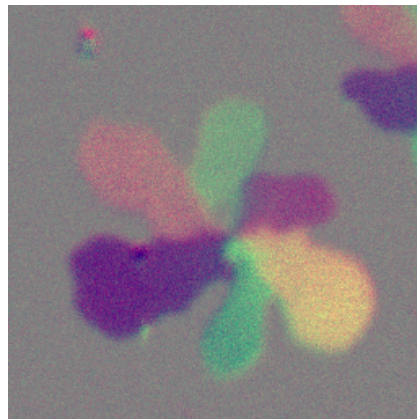
(a) *Real part of $\tilde{I}_2$*

(b) *Imaginary part of $\tilde{I}_2$*

(c) *Red channel is set to the real value and the green channel to the imaginary value of $\tilde{I}_2$. The blue channel is set to 0.*

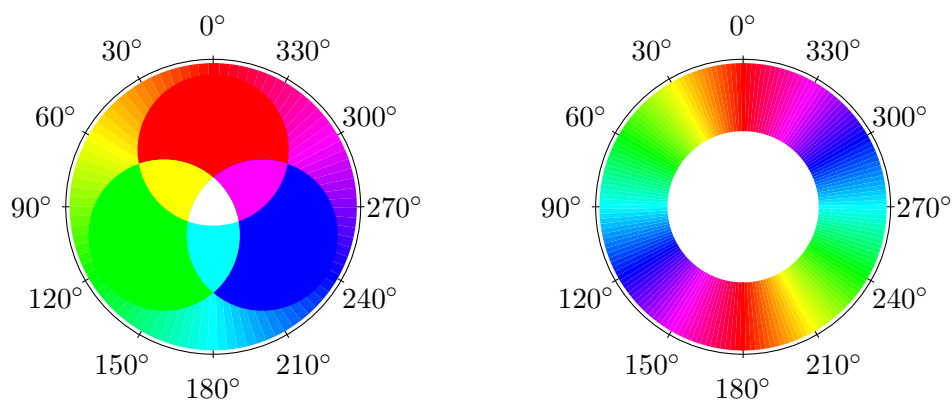**(d)** *Red channel is set to the real value and the green channel to the imaginary value of $\tilde{I}_2$. The blue channel is set to 0.5.*

Figure 5.10: *Visualizations of the real and imaginary part of $\tilde{I}_2$. (a) and (b) Dark regions corresponds to negative values whereas bright regions corresponds to positive values.*

(a) *Hue values and their relation to red, green and blue values.*

(b) *Direction encoding by modified hue.*

Figure 5.11: *(a) Additive mixing of the three primal colors generates a color circle where the color is varied gradually throughout the circle. The numbers along the perimeter is the hue value of the closest color. (b) How directions are encoded by colors.*

Color images can be represented in different color encodings with the red, green and blue (RGB) color model one of the best known. In RGB the color is encoded as the amount of red, green and blue light that should be mixed additively to obtain the color. A conceptually different color model is the hue, saturation and value color model, where the primary color (is the color primary red, green or blue) is described by *hue*, the saturation of the color (is it gray or a bright color) by *saturation* value and the lightness of the color by *value*. Hue is often encoded as an angle in the range of 0° to 359°, where values near 0° area primary red, the green colors are near 120° and the blue colors are near 240°. How colors and hue are related is visualized in figure 5.11a.

The HSV color encoding cannot be applied directly, as the color encoding of the directions 0° and 180° differs considerable, they are red and cyan, but they corresponds to the same fluorophore orientation. The solution is to let the hue values perform two full cycles during one rotation from 0° to 359°, this is visualized on figure 5.11b.

The orientation information can now be encoded as hue values, but what to do with the *saturation* and *value*? If the *value* is set to 1 and the saturation is set to the modulus of $\tilde{I}_2$, the color representation of the analyzed image sequence is shown on figure 5.12. With this color encoding of the orientation it is easy to locate the six sub domains, and the fluorophore orientation can be directly determined by comparing with figure 5.11b. This encoding of the orientation information is currently the best of the methods I have tested, as it is easy to estimate the accuracy and orientation of the determined orientation.
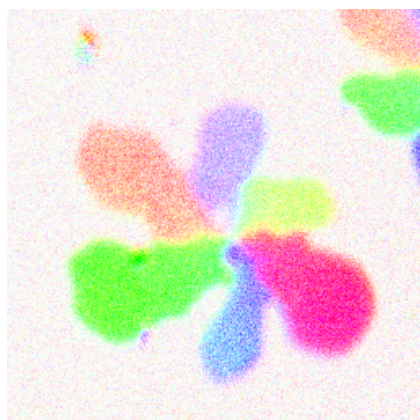
Figure 5.12: *The calculated orientations visualized with the HSV color model.*

5.7 Issues

When using the Fourier analysis based method for determining the fluorophore orientation, there is a few thing to keep in mind. If the sample is moved during acquisition of the image sequence, the input for the analysis is flawed and the determined fluorophore orientations might be severely flawed. Similar distortions can be seen if the domains in the imaged area is growing / changing shape. If the experimenter pays attention to these issues, most problems can be avoided.

5.8 Application of the analysis to other image sequences

During the first part of this chapter only one image sequence have been analyzed with the Fourier analysis. The analyzed image sequence were acquired while the sample were illuminated through a slice of mica, as mica disturbs the polarization state of transmitted light, this experimental setup might have caused some distortions in the measurements. In this section two additional image sequences are examined and this time we were aware of the issues of transmitting polarized light through mica. In these two experiments the supported bilayer were flipped such that the mica were above the supported bilayer, in this setup the sample is illuminated with linearly polarized light.

In figure 5.13 the result of the orientation analysis of the first image sequence is shown. In the image of the fluorophore orientations, six distinct sub domains can be resolved. The examined gel domain have a structure similar to the previously analyzed.

During analysis of the second image sequence some new observations were found. The analysis results is shown in figure 5.14. In the image two whole

(a) *Average image*

(b) *Fluorophore orientation*
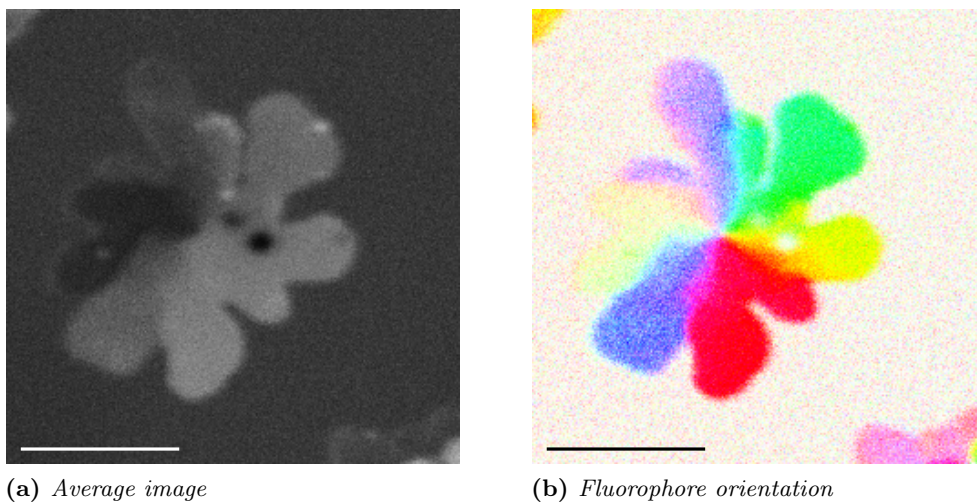
Figure 5.13: *Fluorophore orientation in a gel domain. 5µm scale bars.*

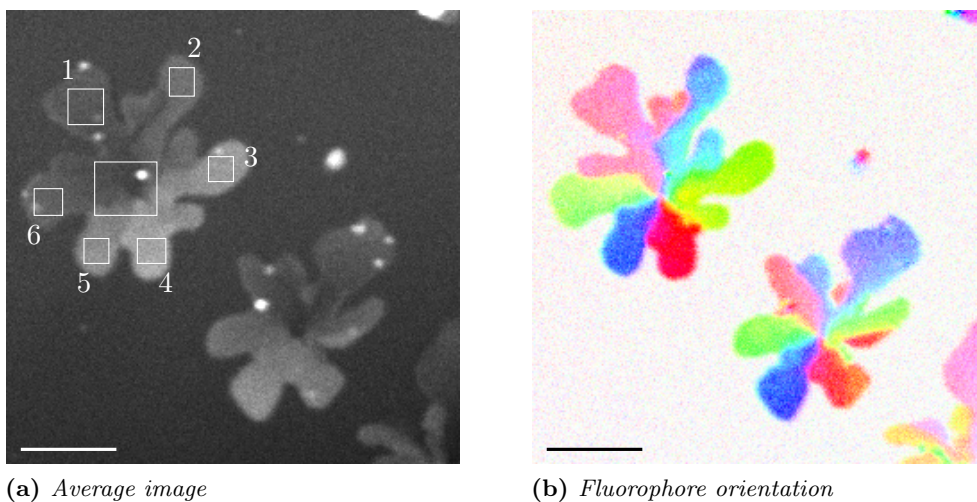**(a)** *Average image*

(b) *Fluorophore orientation*

Figure 5.14: *Fluorophore orientation in gel domains. Intensity variations in the marked regions are investigated later. 5µm scale bars*
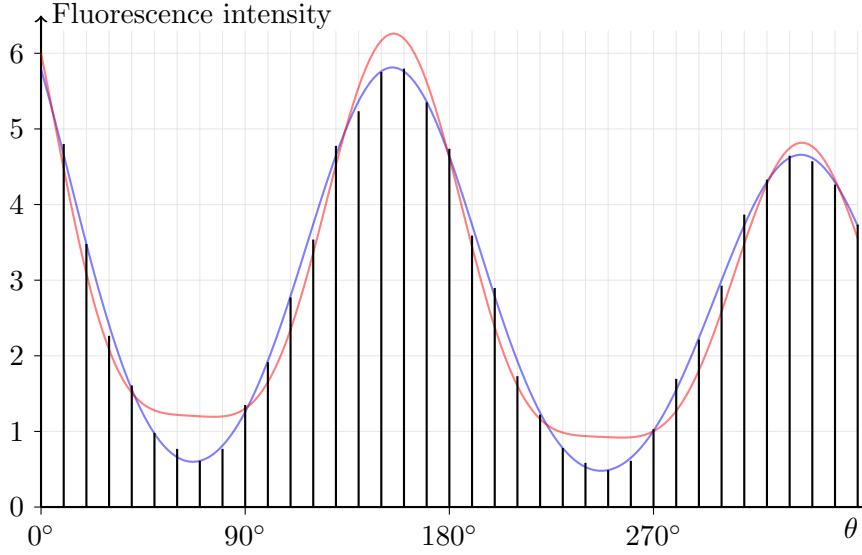
Figure 5.15: *Fits to the average fluorescence intensity of region 5 marked in figure 5.14. The black spikes are the actual measurements and the red and blue curves are the two fitted models (equation (5.19) and (5.20)).*

gel domains can be located, both gel domains have six major distinct sub domains. In addition the rightmost gel domain have two small sub domains, the two small red regions, one above and one to the right of the center. In figure 5.14a seven regions have been marked. In the six numbered regions the average fluorophore of the region have been analyzed as a function of the polarization angle. The measured fluorescence intensity variations in area 5 is shown in figure 5.15 as the solid spikes. Two functions have been fitted to the measured intensity variations, these fitted functions are drawn in red and blue in the figure. Both of the two fitted functions are based on the $\cos^4$ excitation probability which is relevant in two photon excitation. The first formula is the theoretic $\cos^4$ combined with an arbitrary offset or background. The observed fluorescence intensity is seen to decrease significantly over time (the first measurement were at $\theta = 0°$), this bleaching is modelled via an exponentially decreasing term $\exp(-\tau\theta)$ which is multiplied to the two other terms. The equation looks now like:

$$f(\theta) = \left(I_0 \cos(\theta - \theta_0)^4 + I_{bg}\right) \exp(-\tau\theta) \tag{5.19}$$

and is visualized in red in figure 5.15. The other formula is based on the assumption that the fluorophores is not perfectly aligned and that their orientation can be described by a normal distribution centered at θ_0 and width standard deviation σ. The equation is derived in appendix A. Again an exponentially

Domain	I_0	θ_0	I_{bg}	τ	rms	I_0	θ_0	σ	τ	rms
1	2.7	105.0	0.96	0.034	0.16	5.3	105.3	32.1	0.039	0.08
2	4.5	165.5	1.12	0.069	0.26	7.1	165.3	28.1	0.056	0.10
3	7.2	48.2	1.06	0.082	0.27	10.0	48.6	21.3	0.083	0.14
4	8.0	97.3	1.43	0.098	0.41	11.9	97.8	24.3	0.101	0.11
5	6.5	156.9	1.33	0.083	0.33	9.6	156.6	25.9	0.071	0.09
6	3.4	41.4	0.91	0.035	0.16	5.9	41.4	28.3	0.039	0.10

Table 5.2: *Parameters obtained by fitting equation (5.19) and (5.20) to the measured fluorescence intensity variations in the marked regions in figure 5.14a. The given root mean square (rms) values, are a measure of the average residual size. Large values indicates a bad fit.*

decaying factor is added. In figure 5.15 this equation is shown in blue.

$$g(\theta) = \left(\frac{3I_0}{8} + \frac{I_0}{2} \cos(2\theta - 2\theta_0) \cdot \exp\left(-2\sigma^2\right) \right.$$

$$\left. + \frac{I_0}{8} \cos(4\theta - 4\theta_0) \cdot \exp\left(-8\sigma^2\right) \right) \exp(-\tau\theta) \qquad (5.20)$$

If the two fitted functions are compared with the observed fluorescence intensity variations it is seen that the $f(\theta)$ curve is unable to follow the measured intensity as well as the $g(\theta)$ curve. The values obtained from fitting to the measured fluorescence intensity variations in the six regions are shown in table 5.2. In the table the first group of parameters (column 2-5) corresponds to equation (5.19) while the second group refers to equation (5.20). Both fitted functions finds similar fluorophore orientations, their determined θ_0 values differ less than 1° in all cases.

In addition to the average fluorophore orientation θ_0, the fit to equation (5.20) gives some information on the orientation freedom of the fluorophores. The determined value for the orientation standard deviation σ are in the range $21.3° \rightarrow 32.1°$. These values are a bit lower than the similar values from section 5.3, which were in the range $24.2° \rightarrow 38.7°$. This difference might be explained by the changed experimental conditions (whether the illuminating light is transmitted through mica).

In figure 5.14a the center of one of the gel domains were marked. The fluorophore orientations inside this marked region is visualized in figure 5.16. Notice how the fluorophores are points outwards and forms a spiral like structure.

5.9 Summary

Two photon polarization fluorescence microscopy have been used for gaining insight in how the fluorophore Laurdan is oriented inside gel domains. The
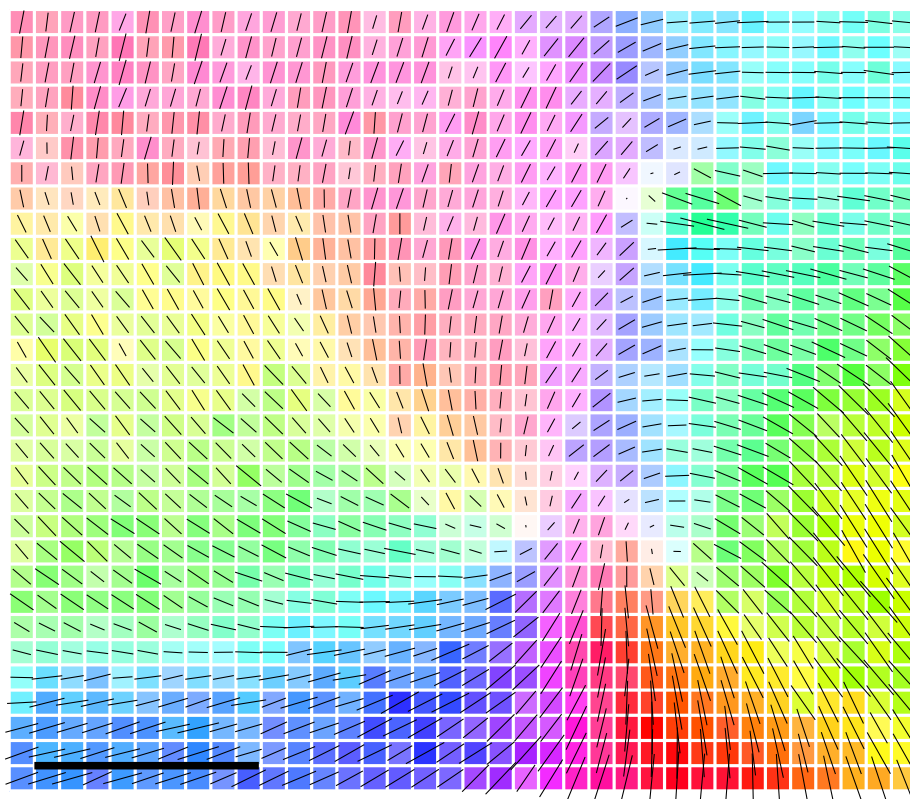
Figure 5.16: *The vortex at close range. 500nm scale bar.*

observed fluorophore orientations divides the examined gel domains into several sub domains (usually is one gel domain divided in six sub domains); in each of these sub domains the fluorophore orientation is approximately homogeneous. The observed fluorescence intensity variations caused by changes in the orientation of the polarized light cannot be explained if the fluorophore orientation distribution is wider than a normal distribution with standard deviation $\sigma \sim 30°$. The average fluorophore orientation if an area can be determined using Fourier analysis of the measured fluorescence intensity variations.

Chapter 6

# Analysis of ripple and stripe phases

This chapter has two logical sections a review of how the ripple and stripe phase domains have been investigated and a presentation of some new results acquired using one photon fluorescence microscopy.

6.1   Historical background

That the compartmentalizing structures in our cells are composed of lipids were known a century ago. How the lipids were organized inside the biological membranes were unknown but were studied with different methods. Fricke measured the capacitance over the lipid structure and estimated the structure thickness to $4nm$ [65]. The structure of the cellular membrane were discovered by Gorter and Grendel in 1925. In their experiment they extracted lipids from the membrane of red blood cells and measured the area of a mono layer of these lipids at an air water interface. They found that the covered area were twice the surface area of the red blood cells from which the lipids were extracted. Through this experiment they concluded that the cellular membrane consists of a lipid bilayer[66]. After this discovery the properties of the lipid bilayer have been investigated with many distinct methods. A systematic examination of lipid bilayers consists of two experimental steps, (1) the preparation of one or more lipid bilayers and (2) the actual investigation of the prepared bilayers. The first method for preparing lipid bilayers with a controlled lipid composition were developed by Langmuir and Blodgett [28]. As biological membranes consists of many different lipid types, a systematic search of all possible combinations would require a prohibitory high number of experiments; by studying bilayers composed of binary and ternary lipid mixtures this number of experiments could be drastically reduced.
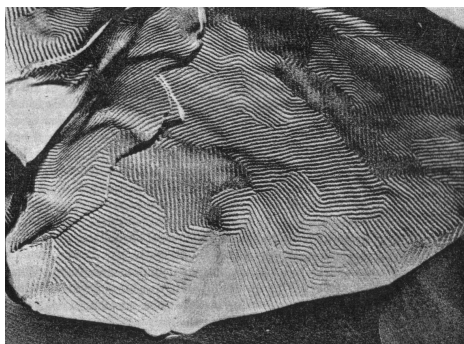
(a) *The ripple phase in a DLPC / DMPC bilayer visualized by Freeze fracture electron microscopy. Verkleij et. al [68].*
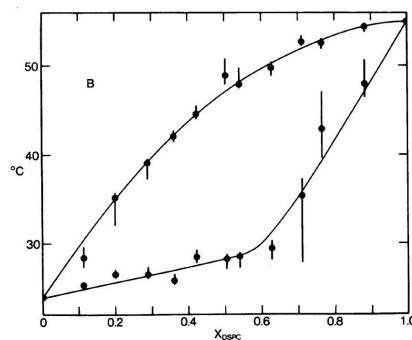
(b) *A phase diagram for DMPC / DSPC mixtures. Mabrey et. al[13].*

Figure 6.1: *Ripple phase domains visualized by freeze fracture electron microscopy and a phase diagram for DMPC / DSPC.*

6.1.1   Membrane phases

In the 70'es, the structure of lipid bilayers were investigated using several distinct methods including fluorescence microscopy[67], differential scanning calorimetry[13], freeze fracture electron microscopy[68] and small angle x-ray scattering (SAXS)[69, 70]. Through the use of these methods the phase behaviour of lipid bilayers were observed. It was found using SAXS that at high temperatures the lipids inside a bilayer would be in a *fluid* phase where the lipid molecules could move freely around in the bilayer, in the fluid state the acyl chains of the lipid molecules would be *melted* and were free to wriggle. At lower temperatures a lipid bilayer would solidify to a *gel* phase with the lipid molecules arranged in a hexagonal close packed structure, in this close packed structure the acyl chains would be fully stretched. In the temperature region between the fluid and gel phase regions, some lipid compositions could be in a third membrane phase, in which the membrane surface were rippled, in this phase the lipid molecules also formed a hexagonal closed packed structure. The bilayer structure of these ripples were investigated by freeze fracture electron microscopy.

An electron microscope cannot directly be used to examine a lipid bilayer in an aqueous solution, as the solution would evaporate in the vacuum inside the electron microscope. The freeze fracture electron microscopy technique is based on rapidly cooling the sample that should be examined to temperatures below $-100°C$, at these temperatures the diffusion of lipid molecules in the membrane would be negligible. The frozen membrane were then covered by a thin layer of metal atoms by evaporation deposition, the sample could now be imagined in the electron microscope. In a review of the results obtained using freeze fracture electron microscopy by Verkleij *et. al* several images of the

rippled phase were included[68]. The found ripples appeared as several straight lines placed in a parallel structure. Where areas of ripples with different orientations met, the ripples formed 60° or 120° angles, which could indicate a hexagonal ordering of the lipids in the ripple phase. Such an image is shown in figure 6.1a. The ripple phase were observed in several mixtures including pure 1,2-dilauroyl-sn-glycero-3-phosphocholine (DLPC), DMPC, DPPC, DSPC and POPC and in binary mixtures consisting of DLPC / DMPC and DMPC / 1,2-dimyristoyl-sn-glycero-3-phosphoethanolamine (DMPE) [68, 69].

Phase changes in lipid bilayers are directly related to conformational changes in the lipid tails and such conformational changes requires energy to proceed. The required amount of heat for raising the temperature of a sample by one degree is the heat capacity of the sample. Near a phase transition the heat capacity of the sample will increase significantly, as energy for the conformational changes are required. Differential scanning calorimetry is a method for measuring the heat capacity of a sample as a function of the temperature. DSC measurements of phosphatidylcholine lipids reveal two peaks in the thermogram, a pre and a main transition. The ripple phase occurs between the pre and main transition. Mabrey and Sturtevant used DSC to examine how the pre and main phase transition temperature were related to the lipid composition[13]. For a binary mixture, the phase transition temperatures can be plotted as a function of the molar fraction of one of the lipids in a phase diagram, such a phase diagram for DMPC / DSPC is shown in figure 6.1b.

6.1.2 Stable and metastable ripple phase

Tenchov *et. al* used DSC and time resolved small angle x-ray scatting techniques for examining DPPC lipid bilayers near the pre and main transitions [71]. The group found two distinct phases with ripple characteristics, a stable ripple phase and a metastable ripple phase. When raising the temperature of a sample from below the pre transition temperature to a temperature between the pre and main transition, the formed ripples where stable. Contrary if the sample temperature initially were above the main transition and the sample were cooled to just below the main transition, metastable ripples were formed.

The freeze fracture technique from 1972 were in 1996 combined with Scanning Tunneling Microscopy (STM) by Woodward *et. al* [72], which used the technique for examining the structure of rippled bilayers in DMPC. In the experiments both the stable and the metastable ripple phase were observed. The stable ripples were found to have an asymmetric sawtooth structure with a periodicity of $11nm$; the metastable ripples were symmetric and had a periodicity of $20nm$. A temperature dependence were found for the amplitude of the stable ripples; at temperatures near the main transition the peak to peak distance were $2.4nm$ and at temperatures near the pretransition the peak to peak distance were nearly zero.
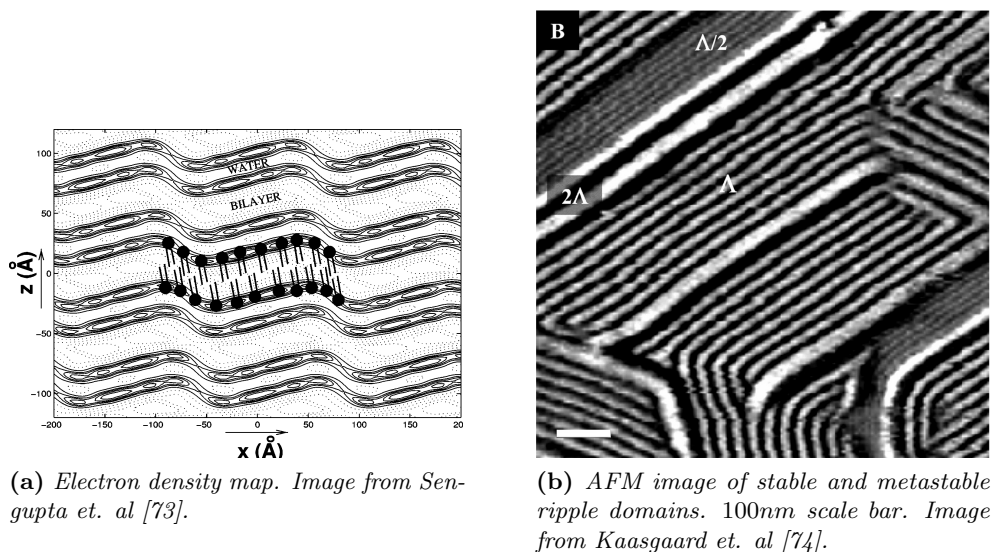
(a) *Electron density map. Image from Sengupta et. al [73].*

(b) *AFM image of stable and metastable ripple domains. 100nm scale bar. Image from Kaasgaard et. al [74].*

Figure 6.2: *The electron density map of the stable ripple phase and AFM image of stable and metastable ripple domains.*

Using data from a x-ray powder diffraction study [10] Sun *et. al* have calculated electron density maps [75] for the ripple phase in DMPC multilamellar bilayers. The asymmetric sawtooth like structure found by Woodward *et. al* were confirmed by the calculated models. Similar electron density models for DMPC, POPC, dihexadecyl phosphatidylcholine and DLPC were calculated by Sengupta *et. al* [73]. Sengupta *et. al* finds two characteristic ripple shapes, an asymmetric sawtooth like shape and a symmetric shape. The symmetric shape were linked to a metastable ripple phase while the asymmetric were linked to the stable ripple phase. The determined electron density map for the asymmetric ripples is shown in figure 6.2a.

Atomic force microscopy can be used to study the surface of supported lipid bilayers. Kaasgaard *et. al* used AFM to examine the ripple phase in DPPC lipid bilayers [74]. Depending on the thermal history the group found stable ripple phase or mixtures of stable and metastable ripple phase. In figure 6.2b one of their AFM images is reproduced, in the image three different ripple domains are found. A stable ripple domain denoted $\Gamma/2$, a metastable denotes Γ and an unnamed denoted 2Γ. Additionally they investigated the growth of stable ripple phase domains and found that the ripple domains grow by one ripple at a time indicating that ripple growth in the longitudinal direction are much faster than building ripples transversely.
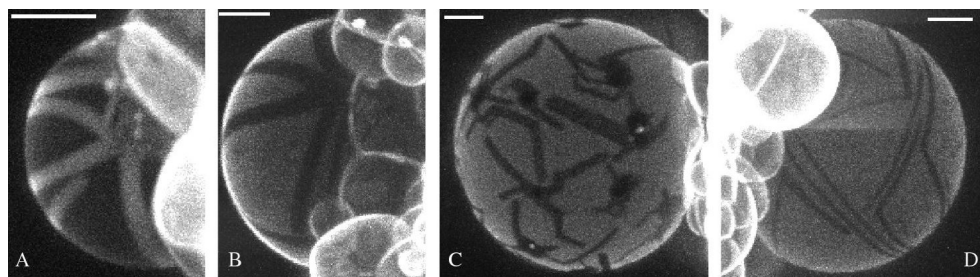
Figure 6.3: *Two–photon confocal microscopy of DLPC / DPPC 1:1 GUVs showing the stripe phase. Scale bars represent 5µm. Image from Beales et. al [77].*

6.1.3 Stripe phase

Giant unilammelar vesicles is a model system for the plasma membranes in animal cells. In GUVs the gel and fluid phases can coexist at a range of temperatures and lipid compositions; when fluid and gel phase domains coexist, the gel domains in general have rounded shapes. A phase with sharp / straight line edges were found in GUVs composed of DLPC / DPPC (1:1) in 1999[76]. This type of domains consisting of stripes with sharp edges and characteristic corner angles near 60° or 120° have been reported several times [22, 77]. The sharp edges and quantized corner angles indicates a strong molecular ordering in the stripe phase. Confocal microscopy of DLPC / DPPC (1:1) GUVs reveals that the fluorophore DiI is strongly aligned inside the stripe domains [78].

6.1.4 Simulations

Simulations of self aggregation of lipid molecules using molecular dynamics, where the motion of each atom is simulated, required access to large amounts of computing power. One of the first molecular dynamics simulations of lipids in a bilayer were [79]. In 2005 de Vries *et. al* [80] were able to run MD simulations on sufficiently large lipid bilayers modelling DPPC. Their simulation consisted of 256 DPPC lipid molecules and 23 water molecules for each of the lipid molecules. When the temperature were decreased from above the main transition to $10°C$, the internal structure of the lipid bilayer changed from a fluid like phase to a state with periodic variations in the bilayer thickness and with an asymmetric sawtooth like shape.

It was now possible to simulate the ripple structure, and [81] Sun and Gezelter started to investigate under which conditions rippled structures emerged. The work was based on a coarse grained lipid model consisting of a zwitterionic head group and an ellipsoid shaped body, see figure 6.4a. Their simulations revealed that the relative size of the head group and the strength of the head group dipole moment determined the observed phase, see figure 6.4b. Asym-
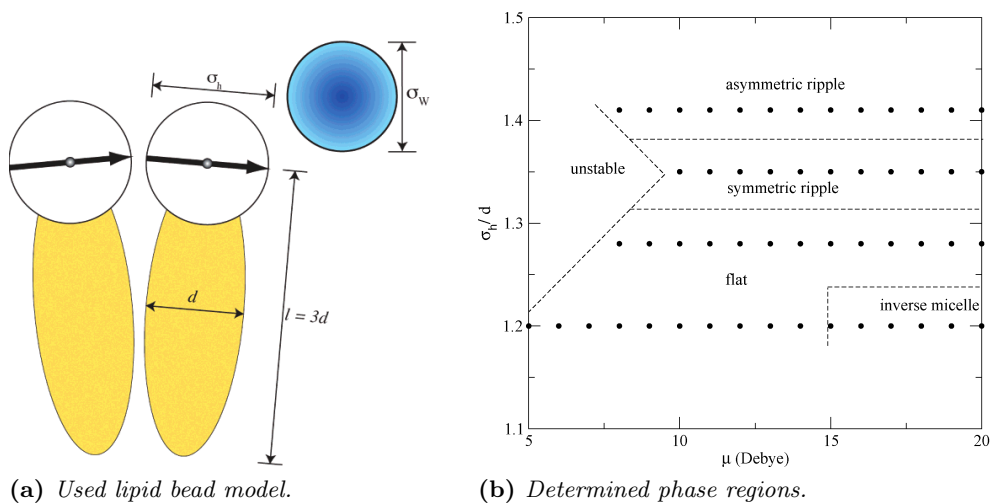
(a) *Used lipid bead model.*

(b) *Determined phase regions.*

Figure 6.4: *Lipid bead model used for exploring how the head group size and dipole moment affects the formed lipid bilayer. Images from Sun et. al [81].*

metric ripples were only found for large head groups, symmetric ripples and flat bilayers were observed when the head group size were reduced.

6.2 Coexistence regions

The model system that our experiments are based on is supported lipid bilayers prepared using the spin coating method. The prepared lipid bilayers are then examined using fluorescence microscopy. We wanted to examine coexisting phase domains in binary lipid bilayers. Using the JPK Biocell combined with a temperature controller the sample temperature can easily be set to a temperature in the range $15°C \rightarrow 55°C$. This temperature range will make it nearly impossible to work with lipids with main transition above $50°C$, as it would be difficult to perform thermal equilibration of the samples.

Observations during cooling Binary mixtures of DPPC and POPC have a large phase coexistence region with temperatures in the range that can be reached by the temperature controller. The main transition temperatures of DPPC and POPC are $42.7°C$ and $-3.4°C$ respectively, mixtures of these two lipids will have phase coexistence at temperatures between the two main transitions. DPPC / POPC lipid bilayers have been prepared with the following lipid molar ratios: 3:7, 5:5 and 7:3. The bilayers have been stained with DiI (0.5% mol) and examined using one photon fluorescence microscopy. Initially the lipid bilayers are equilibrated by maintaining a sample temperature above
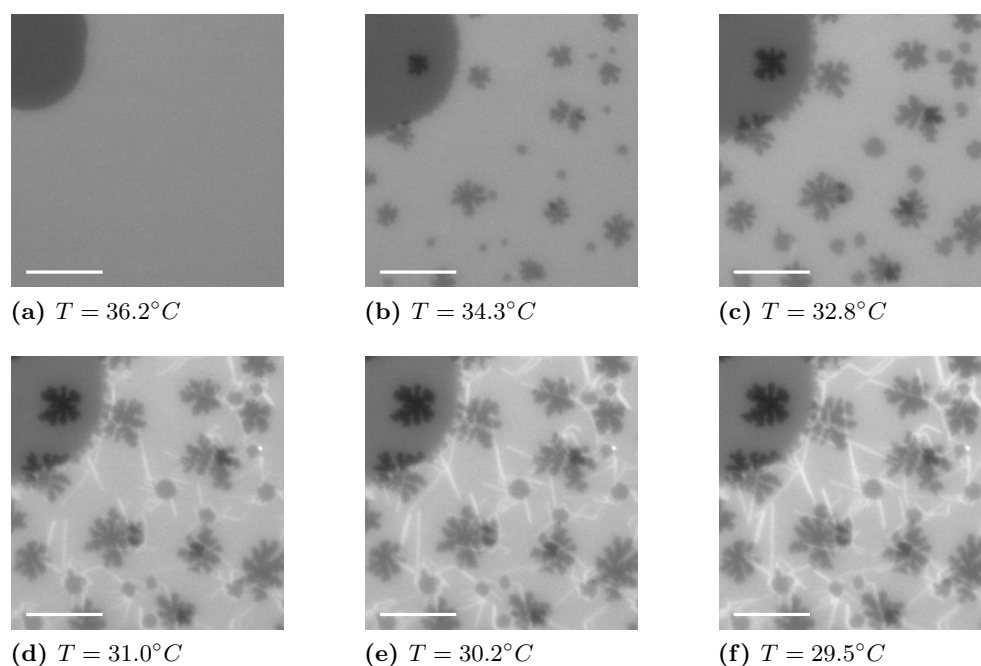
(a) $T = 36.2°C$ **(b)** $T = 34.3°C$ **(c)** $T = 32.8°C$

(d) $T = 31.0°C$ **(e)** $T = 30.2°C$ **(f)** $T = 29.5°C$

Figure 6.5: *How phase domains appear during cooling of DPPC / POPC (1:1) supported lipid bilayers. 20µm scale bars.*

$50°C$ for at least 15 minutes. Afterwards the temperature is decreased at a steady rate.

During cooling of the DPPC / POPC (1:1) sample nucleation of gel domains are seen in the first bilayer near $36°C$, later when the temperature reaches $33°C$ stripe domains nucleates in the second bilayer. Six images from this cooling sequence are shown in figure 6.5. Initially (a) two areas can be seen, a small dark region in the upper left corner in a large and brighter area. The small dark region is a region of the examined sample where there is only bilayer on top of the solid support; in the brighter area there are two lipid bilayers on top of the support. Both bilayers are in the fluid state. In the next image (b) gel domains have nucleated in both the first and second bilayer, the small round domains are gel domains in the second bilayer and the larger domains with the fractal shapes are in the first bilayer. The difference in gel domain shapes from the first to the second bilayer is an indication of the influence from the solid support. The influence of the solid support is strongly reduced from the first to the second bilayer. Bright stripes appear in image (d), the formed stripes have all straight line segments over long distances, this indicates a strong molecular ordering inside these domains.

6.3 How composition influences the phase behavior

When the composition of the lipid bilayer is altered the temperatures at which the domains of a new phase are nucleated will be changed; in general if the amount of POPC (low main transition temperature) is increased, the nucleation temperature will be lowered. The lipid composition can be changed by altering the molar fractions or replacing one of the lipids with another lipid. Four lipid combinations (DPPC / POPC, DPPC / POPG, DPPG / POPC and DPPG / POPG) have been used. For each of these lipid combinations three lipid solutions with different molar fractions were prepared, the used fractions were 3:7, 5:5 and 7:3. The phase behaviour of these twelve binary lipid mixtures have been examined. The negative charge in the anionic phosphoglycerols will be repelled from the negative charged mica support. This repulsion will increase the distance between the solid support and the lipid bilayer. This increased distance will reduce the perturbations from the solid support on the formed lipid bilayers.

DPPC / POPC mixtures The temperature of the observed domain nucleations are visualized as a function of the lipid composition in the binary mixture in figure 6.6a. Nucleation of gel domains in the first bilayer are marked by • and the nucleation of stripe domains are marked by ▽. For each conducted experiment the observed nucleation temperature is indicated. The black line connects the main phase transition temperatures of the two pure lipids.

The stripe shaped domains are located in all the examined bilayers except the first, which is strongly influenced by the solid support. In figures 6.6b, 6.6c and 6.6d images from the three different lipid fractions (7:3, 1:1 and 3:7) are shown. In all systems are gel domains found in the first bilayer and stripe domains is seen in the second bilayer. The contrast between the formed stripes and the fluid background is seen to depend on the lipid composition, higher fractions of POPC in the supported bilayer results in high contrast. The morphology of the formed stripes is seen to depend on the lipid composition. For high molar fractions of DPPC, very thick stripe phase domains are formed in the second lipid bilayer. When the fraction of DPPC is lowered, the formed stripe domains will be thinner. The stripe domains found in figure 6.6d is somewhat crippled.

DPPC / POPG mixtures The addition of negative charges to the lipid bilayer influences the phase behaviour of supported bilayers significant. The observed phase transition temperatures are shown in figure 6.7a. Images of the three mixtures are shown in figures 6.7b, 6.7c and 6.7d. In the conducted experiments only the first lipid bilayer have been imaged. During the hydration procedure all bilayers except the first were flushed away from the
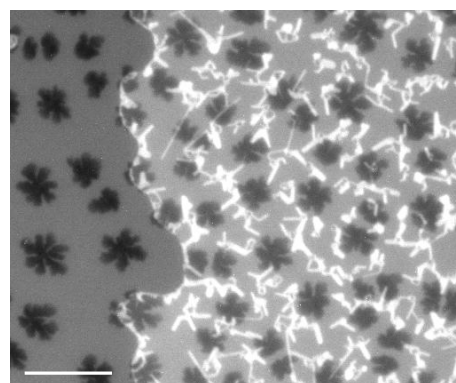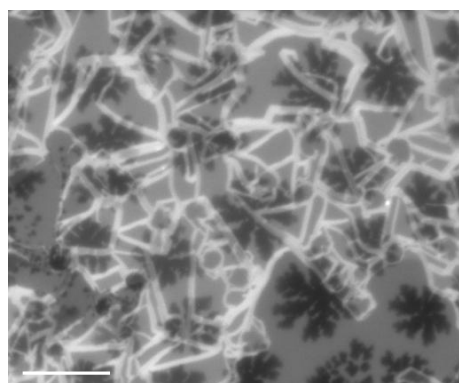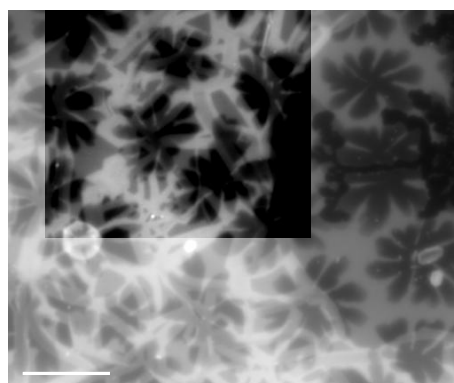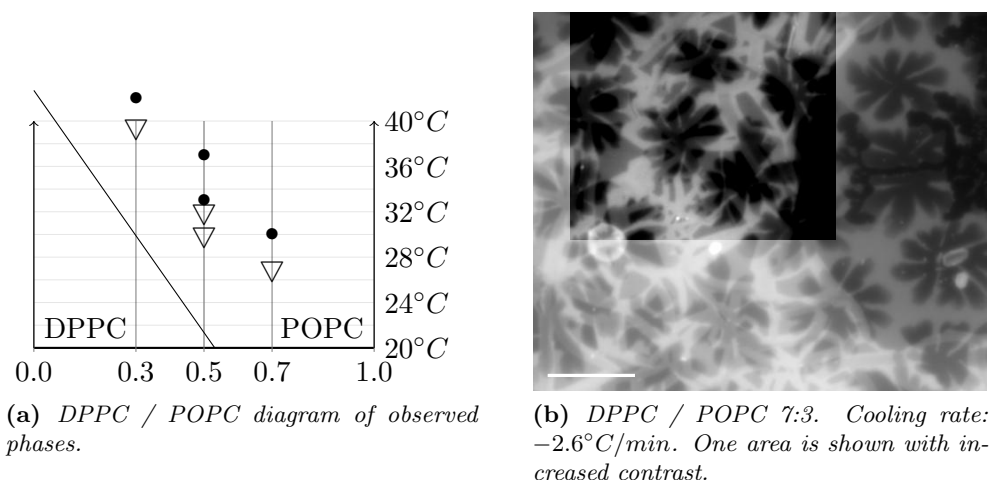
(a) *DPPC / POPC diagram of observed phases.*

(b) *DPPC / POPC 7:3. Cooling rate: $-2.6°C/min$. One area is shown with increased contrast.*

(c) *DPPC / POPC 1:1. Cooling rate: $-1.6°C/min$*

(d) *DPPC / POPC 3:7. Cooling rate: $-2.8°C/min$*

Figure 6.6: *DPPC / POPC mixtures. $20\mu m$ scale bars.*

solid support. The sample with most DPPC formed solid domains and some scattered bright domains, which might be stripe domains. In the equimolar mixture both fluid, stripe and gel domains can be observed simultaneously. No stripe formation were seen in the lipid mixture with excess POPG. The sample were cooled to $\sim 16°C$, but if the nucleation temperature, for stripe domains in this lipid mixture, is below the reached temperature no formation of stripe domains would take place.

DPPG / POPG mixtures The observed phase transition temperatures are shown in figure 6.8a. The observed phase transition temperatures seems wrong as they are quite different from the other observations (lower in temperature and no clear decreasing trend). Images of DPPG / POPG supported lipid bilayers are shown in figures 6.8b, 6.8c and 6.8d. The supported lipid bilayers

(a) *DPPC / POPG diagram of observed phases*

(b) *DPPC / POPG 7:3. Cooling rate: $-2.0°C/min$*

(c) *DPPC / POPG 1:1. Cooling rate: $-2.4°C/min$*
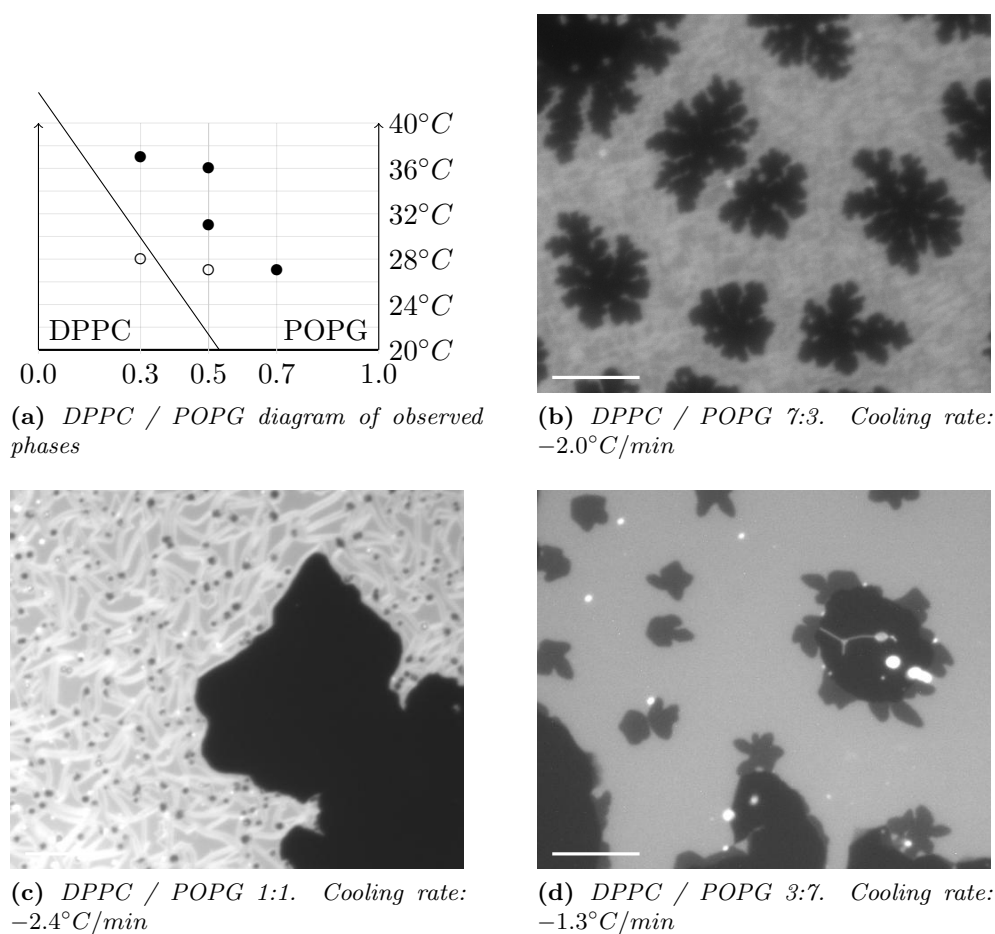

(d) *DPPC / POPG 3:7. Cooling rate: $-1.3°C/min$*

Figure 6.7: *POPG / DPPC mixtures. 20µm scale bars.*

composed of phosphoglyceroles were not able to produce domains with spikes. During cooling gel domains will nucleate and afterwards a rim will form around these gel domains.

DPPG / POPC   The observed phase transition temperatures are shown in figure 6.9a and images from the three different lipid compositions are shown in figure 6.9b, 6.9c and 6.9d. At high molar fractions of DPPG the formed domains have round boundaries. The equimolar mixture form round gel domains, around these gel domains stripe domains will nucleate and grow into the fluid membrane as spikes.

General observations   Well define stripe phase domains is only observed in bilayers composed of a large fraction of phosphocholines. Stripe phase occurs in the first lipid bilayer if the bilayer contains anionic lipids. If no net charge
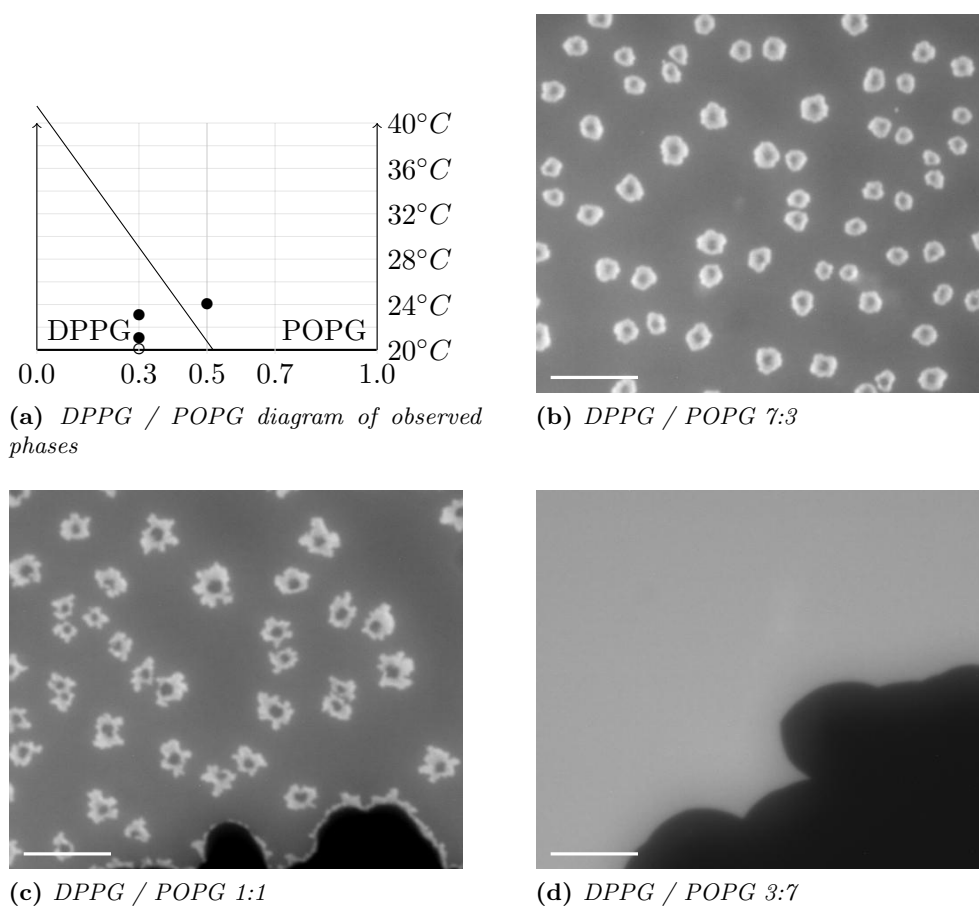
(a) *DPPG / POPG diagram of observed phases*

(b) *DPPG / POPG 7:3*

(c) *DPPG / POPG 1:1*

(d) *DPPG / POPG 3:7*

Figure 6.8: *DPPG / POPG mixtures. 20µm scale bars. The 7:3 molar mixture were cooled to 16°C but no nucleation were seen.*

is present in the lipid bilayers, the stripe phase is not seen in the first bilayer but in the rest.

6.4 Fluorophore anisotropy in fluid, stripe and gel domains

The well defined structure of the stripe domains (the long straight lines and the sharp edges), indicates that the lipid molecules inside the stripe phase must be in an ordered state. We are not able to directly measure how the lipid molecules are ordered, but some hints about the ordering can be gathered using polarized light. If the lipid molecules are ordered, this ordering could influence how a fluorophore like DiI will be aligned in the lipid bilayer. Such an ordering of the fluorescent molecules can be detected by the use of linearly polarized

(a) *DPPG / POPC diagram of observed phases*

(b) *DPPG / POPC 7:3. Cooling rate: -3.1°C/min*

(c) *DPPG / POPC 1:1. Cooling rate: -2.9°C/min*

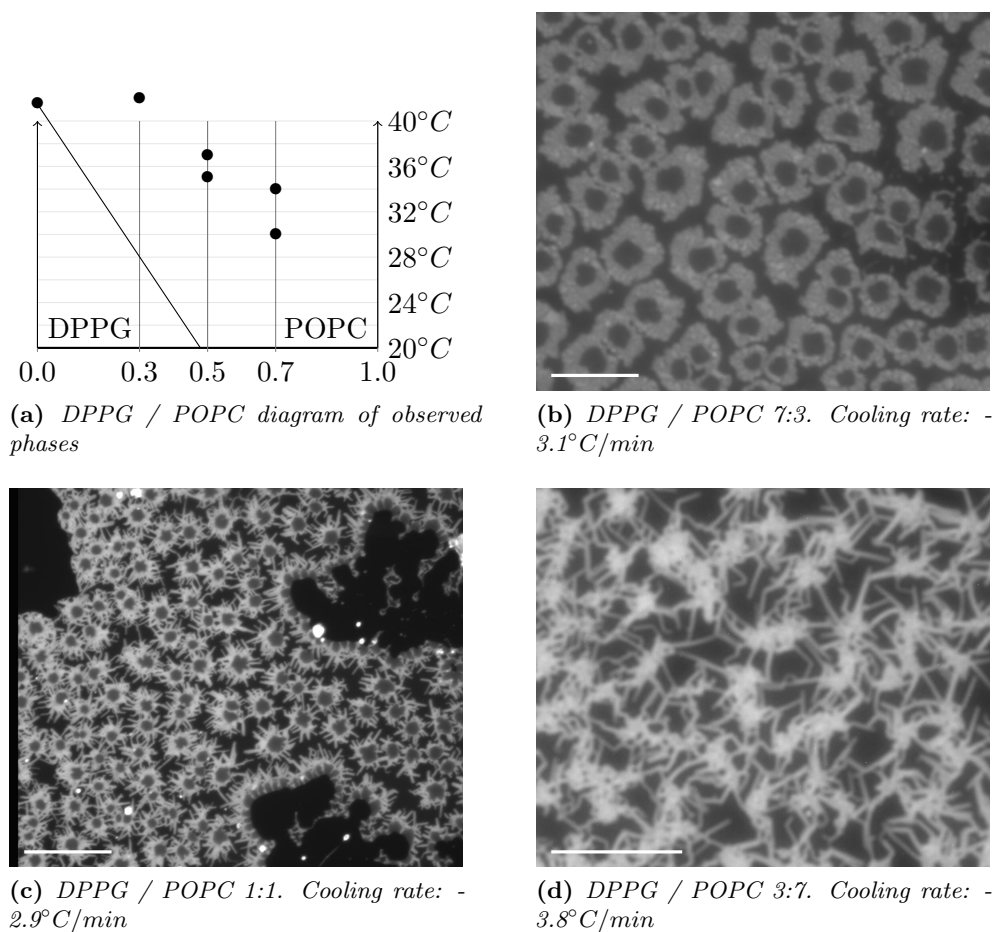**(d)** *DPPG / POPC 3:7. Cooling rate: -3.8°C/min*

Figure 6.9: *DPPG / POPC mixtures. 20µm scale bars.*

light. How a fluorescent molecule interacts with polarized light is determined by the *transition dipole*. In linearly polarized light the electrical field of the radiation can only be in a single plane / direction. The angle ρ between the electrical field of the incoming light and the transition dipole determines how probable it is to excite the fluorophore. For one photon microscopy the relation between the emitted intensity I and the angle ρ is given below:

$$I \propto \cos(\rho)^2 \tag{6.1}$$

The used fluorescence microscope have been equipped with a linearly polarization filter such that the excitation illumination can be linearly polarized in an arbitrary direction that lies in the image plane. The polarization response of the sample can then be determined by acquiring a sequence of images in which the direction of the linearly polarized light is gradually changed from image to image. If the acquired image sequence is analyzed using the method described
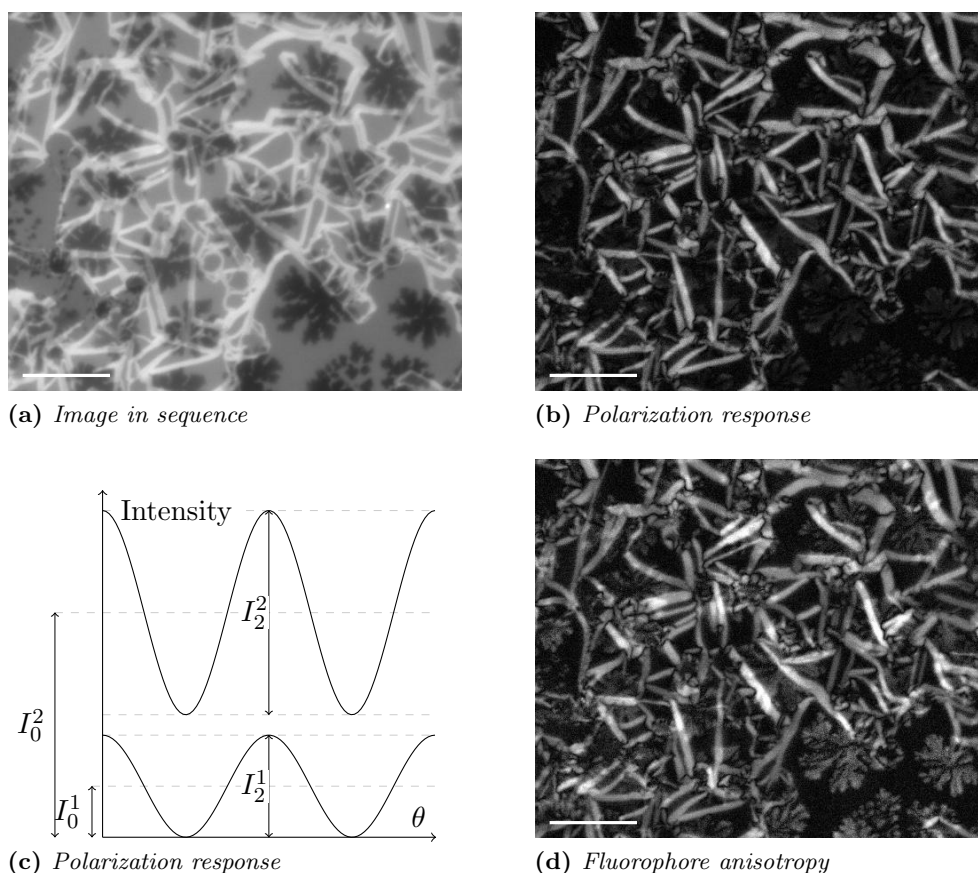
(a) *Image in sequence*

(b) *Polarization response*

(c) *Polarization response*

(d) *Fluorophore anisotropy*

Figure 6.10: *Image from a polarization sequence of a DPPC / POPC (1:1) supported lipid bilayer. From the image sequence the polarization response and fluorophore anisotropy have been calculated. 20μm scale bars.*

in chapter 5, the magnitude of the polarization induced intensity variations $|\tilde{I}_{\gamma=2}|$ can be visualized. A supported double lipid bilayer composed of an equimolar mixture of DPPC and POPC have been examined, at the acquisition time there were gel domains in both the first and the second bilayer and stripe domains in the second bilayer. In figure 6.10 the results of such a polarization analysis is visualized. 6.10a is one of the acquired images and can be used as a reference image for determining which structures that are at specific locations. In 6.10b is the observed polarization response visualized, notice the strong polarization response form the stripe domains that can be found in figure 6.10a. A closer inspection of the polarization response image reveals that the fluid background appear completely black, while the gel domains in the first bilayer have a small polarization response. What can be concluded from the observation that the polarization response in stripe domains is larger

than the polarization response in gel domains? It is not possible to conclude that fluorophores in stripe domains are more aligned than fluorophores in gel domains, as the polarization response depends on more than the fluorophore alignment. To understand why this is the case, two oscillating signals signals I^1 and I^2 have been compared compared in figure 6.10c. The two signals have the following functional dependence on θ:

$$I^1 = 1\cos(\theta)^2 \qquad\qquad I^2 = 1.2 + 2\cos(\theta)^2 \qquad (6.2)$$

The amplitude of the oscillations corresponds to the polarization response shown in figure 6.10b. It is easy to observe that I^2 have a larger amplitude than I^1, but this does not directly tell us how aligned the fluorophores are. If all the fluorophores are perfectly aligned, the fluorescence intensity will be zero when the electrical field of the illuminating light is orthogonal to the transition dipole in the fluorophore and maximal when they are parallel. If the fluorophores are randomly oriented the fluorescence intensity will be independent on the polarization orientation. If the fluorophore orientation is described by a Gaussian distribution with mean value θ_0 and standard deviation σ (value in radians), the fluorescence intensity will vary with the polarization orientation θ as follows:

$$E\left[F(\theta)\right] = \frac{I_0}{2} + \frac{I_0}{2}\cos(2\theta - 2\theta_0) \cdot \exp\left(-2\sigma^2\right) \qquad (6.3)$$

The formula is derived in appendix A. The polarization response scales linear with the signal strength I_0, which is proportional to the fluorophore concentration. The average fluorescence intensity during the full polarization sequence is also linear in the signal strength. By dividing the polarization response with the average fluorescence intensity, a measure of the relative intensity variations can be obtained, this value is denoted Ω.

$$\Omega = \frac{\left|\tilde{I}_{\gamma=2}\right|}{\tilde{I}_{\gamma=0}} \qquad (6.4)$$

The relative change in fluorescence intensity is a measure of the fluorophore anisotropy (how aligned are they). In figure 6.10d the fluorophore anisotropy is visualized. If the image of the fluorophore anisotropy is compared to an image from the polarization sequence (figure 6.10a), three things can be observed:

- Fluid domains have a low fluorophore anisotropy, this confirms that the fluid domains consist of randomly ordered lipids.

- Gel domains have a significant fluorophore anisotropy, but they are divided into sub domains separated by low anisotropy regions. Such sub domains are examined in chapter 5.
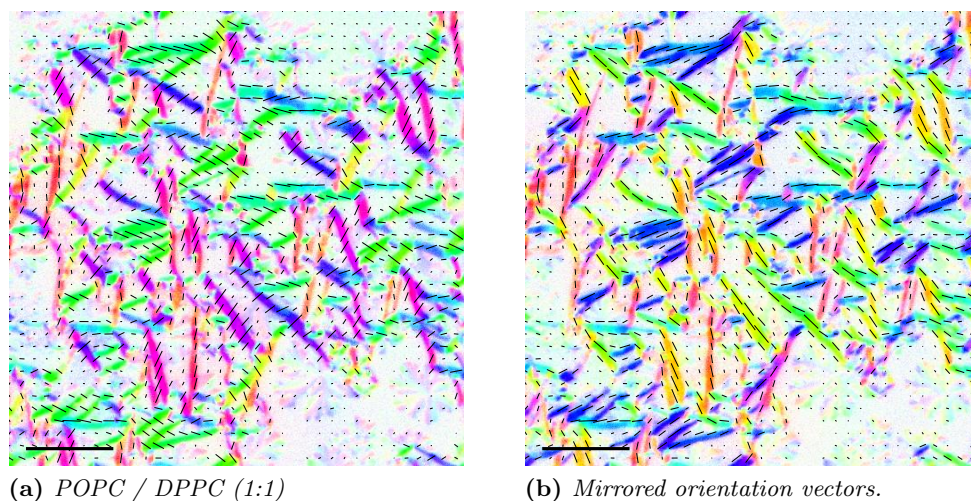
(a) *POPC / DPPC (1:1)* **(b)** *Mirrored orientation vectors.*

Figure 6.11: *Reversed direction of polarization. 20μm scale bars.*

- Stripe domains have a high fluorophore anisotropy, which indicates an ordered lipid structure.

The polarization analysis have shown that the fluorophore molecules are well aligned inside the stripe domains. The next task is then to determine how they are oriented relative to the stripe domains.

6.5 Fluorophore alignment in the stripe phase

Earlier we found that fluorophores embedded in the stripe phase are strongly oriented, as high anisotropies are observed. When the fluorophores have a high anisotropy, there must be a preferred orientation for the fluorophore, this preferred orientation can be determined using the method described in chapter 5.

The direction of the polarized light must be calibrated before performing the actual analysis. The calibration is done by setting the polarization filter at a known orientation, the polarized light is now passed through the objective and directed against the sample. Linearly polarized light is not able to pass through a linear polarization filter oriented orthogonal to the polarization orientation. Using this property and a linear polarization filter with a known polarization orientation, the polarization orientation of the illuminating light can be calibrated. The fluorophore orientation can now be calculated by using these calibrated angles, and are visualized on figure 6.11a. The superimposed black lines in the figure are directors that show in which direction the electrical field of the excitation light must be for producing the largest fluorescence intensity. In addition to the black lines, colors in the underlying image

represents the same information, red indicates the up / down direction and cyan the left / right direction. The first observation is that stripes with the same orientation have the same color, eg. all the cyan colored stripe domains are elongated in the left–right direction; that indicates that the fluorophore will be aligned either in the direction of the stripes or perpendicular to the stripe.

Systematic errors Unfortunately there is a problem with the calculated fluorophore orientations, this can be seen by comparing how the directors of cyan and green stripe domains are oriented relatively to the direction of the stripes. The directors in the cyan stripes are parallel to the elongated axis of the stripe domains, for the green stripes the directors are nearly perpendicular. By comparing stripes with the same color, it were observed that colors corresponding to perpendicular directions (red / cyan, blue / orange and green / magenta) had the same offset between the stripe direction and the orientation of the director. There were indeed a system in the found deviations, but which system. Figure 6.11b is based on the same sequence of polarization images as figure 6.11a, except that all the calculated orientations had been reflected along the y axis. Now all the directors were oriented parallel to the analyzed stripe domains and we just needed an explanation why this occurs. The next clue were found by analyzing several polarization image sequences acquired of lipid bilayers supported by mica or glass. The mirroring of the calculated directors were only observed in the samples where mica was used as the solid support. The determined fluorophore orientation in one of the samples with glass used as the solid support is shown in figure 6.12. The observed mirroring of the directors can be explained by the birefringent properties of mica, this is described in details in chapter 3. When linearly polarized light is passed through a birefringent material such as mica, the polarization state of the transmitted light can be altered significantly; if the slice of mica has the proper thickness it acts like a half wave plate and effectively mirrors the direction of polarization through one of the axes. Such a reflection of the polarization state will change an increase in polarization angle before the beam passes the slice of mica to a decrease in polarization angle of the transmitted beam.

Loss of information Another annoying effect of using a birefringent material like mica as a solid support are shown on figure 6.13 where the found orientations are encoded by colors. Image (a) mainly consists of two colors, blue and orange; in the used color encoding blue and orange corresponds to orthogonal directions, this indicates that the determined orientations are flawed. In image (b) the same effect is seen, only cyan and red direction encodings are found even if other stripe orientations can be seen. This effect is also caused by the birefringence of mica, in this case the slice of mica have a thickness giving it
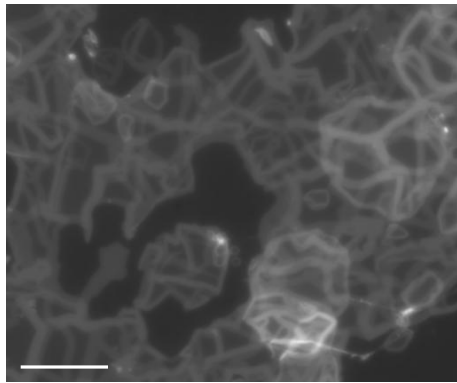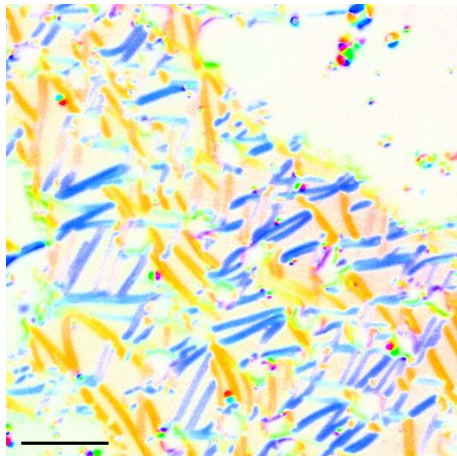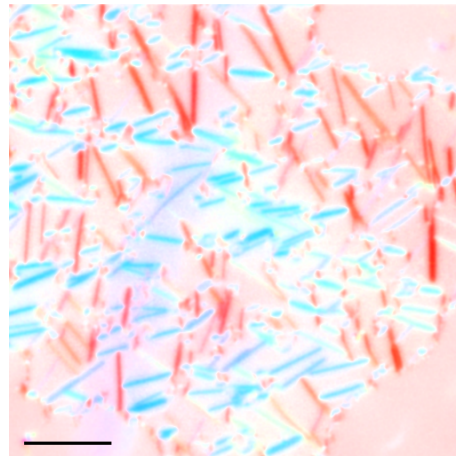
(a) *Average image*
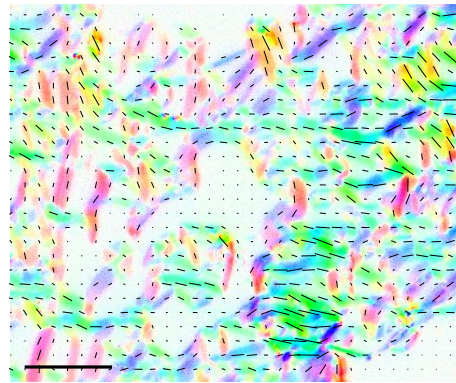
(b) *Fluorophore orientation*

Figure 6.12: *Control experiment using glass as the solid support. DPPC / POPC 1:1. 20μm scalebars.*

(a) *POPG / DPPC (1:1)*

(b) *POPG / DPPC (1:1)*

Figure 6.13: *Loss of direction, only showing two orthogonal orientations. 20μm scale bars.*

the optical properties of a quarter wave plate.

A detailed description of how polarized light is affected by passing through a piece of mica is given in section 3.2. Depending on the thickness of the mica slice, it might be possible to correct for the change in polarization state. If the piece of mica acts like a quarter wave plate it is not possible to recover enough information for determining the fluorophore orientation. Is the piece of mica thicker and acts like a half wave plate, the polarization state will be reflected along one of the optical axes in the mica crystal. This reflection of the polarization state can there be dealt with using the following equation:

$$\theta_{\text{corrected}} = -\theta_{\text{measured}} + \theta_{\text{offset}} \tag{6.5}$$

where θ_{offset} is determined by the orientation of the optical axes in the mica crystal. The value of θ_{offset} can be determined by measuring the polarization state of the linear polarized light used to illuminate the sample *after* it has passed the piece of mica and not before as the previously used calibration method did. This calibration have to be be done for all of the examined samples as each sample might be oriented differently leading to altering values of θ_{offset}.

6.6   Fluorophore alignment in gel domains

In chapter 5 the lipid tilt orientation in gel domains were examined using two photon microscopy with Laurdan as fluorophore. A supported lipid bilayer with the lipid composition: DPPC / POPC 7:3 have been examined with one photon microscopy. The sample were stained with DiI. 18 images were acquired with varying polarization orientations. In figure 6.14a the average image from the image sequence is shown. The polarization response and the fluorophore anisotropy are visualized in figures 6.14b and 6.14c. The gel domains have a significant fluorophore anisotropy. For visualizing the prefered fluorophore orientations inside the gel domains, the color encoding described in section 5.6 have been used with a minor modification. The fluorophore anisotropy were used as the color saturation value instead of the polarization response.

6.7   Ripple domains related to fluorophore anisotropy

By combining AFM and polarization fluorescence microscopy, we have studied how rippled domains produce a polarization response. The examined sample is a mica supported lipid bilayer composed of an equimolar mixture DPPG and POPC. In figure 6.15 the same area of the sample have been examined using polarization fluorescence microscopy and AFM. (A) is an image acquired by the fluorescence microscope, the red square indicates the area that were
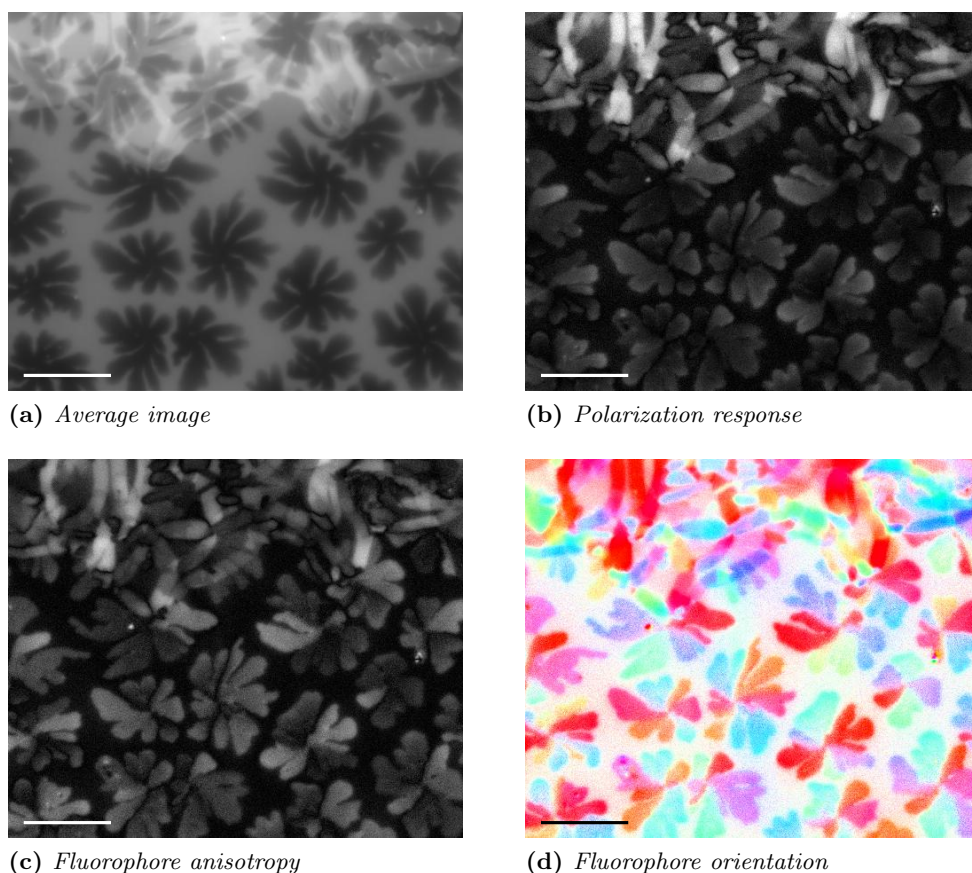
(a) *Average image*

(b) *Polarization response*

(c) *Fluorophore anisotropy*

(d) *Fluorophore orientation*

Figure 6.14: *Fluorophore orientation in gel domains visualized by one photon microscopy. DPPC / POPC 7:3. 20μm scale bar.*

examined by AFM, in (B) the green color indicates the fluorescence response and the underlying gray scale image is the acquired AFM image of the same area. In image (C) the measured fluorophore orientation is overlaid on the AFM image. In (C) only two distinct orientation are found (color encoded as green and magenta). Notice how the regions with ripple domains are covered by colored regions indicating the direction of the ripples. Polarization fluorescence microscopy can determine the orientation of ripples, which are smaller that the optical resolution limit!
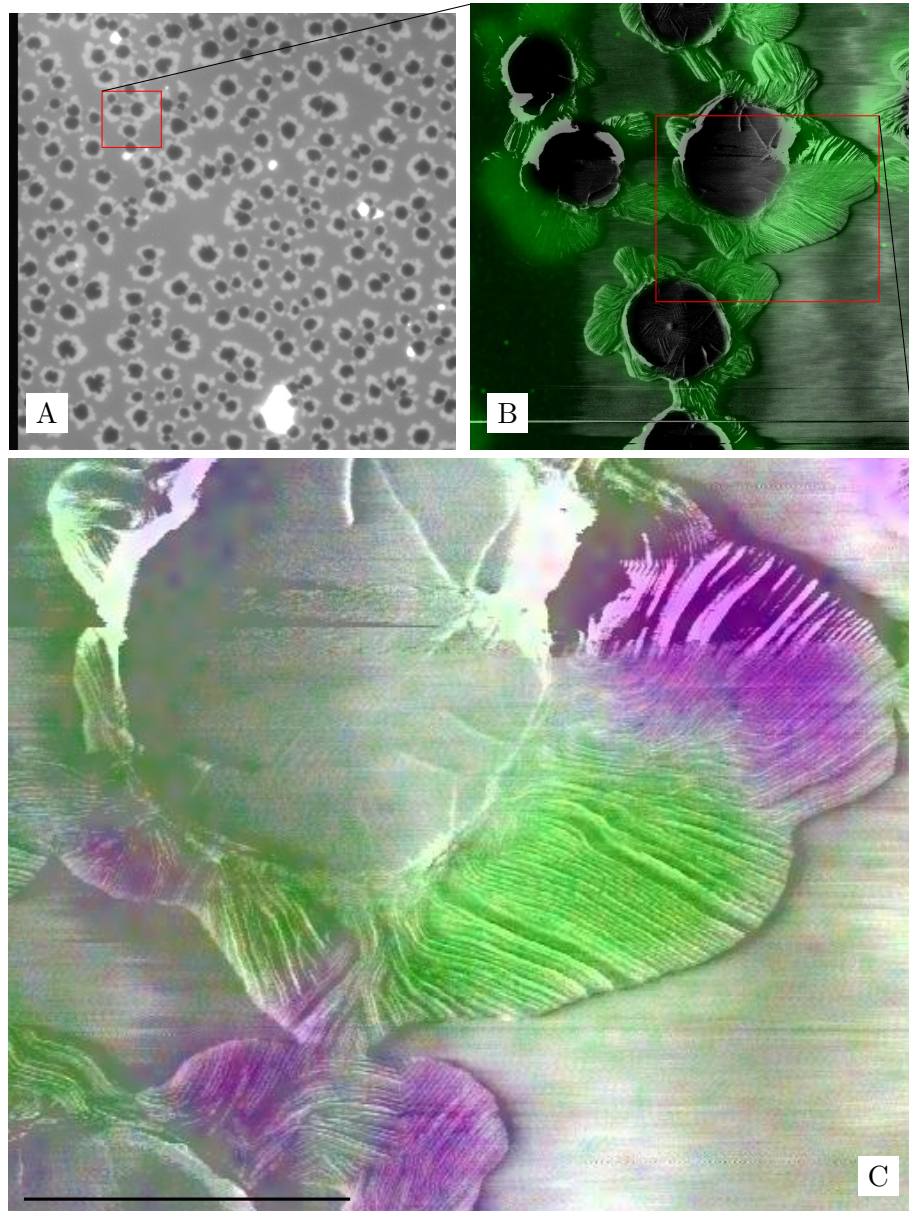
Figure 6.15: *DPPG / POPC (1:1). AFM image with the calculated directions superimposed. 5μm scale bar.*

(a) $T = 33.0°$ **(b)** $T = 31.8°$ **(c)** $T = 31.1°$

(d) $T = 30.7°$ **(e)** $T = 30.3°$ **(f)** $T = 29.8°$

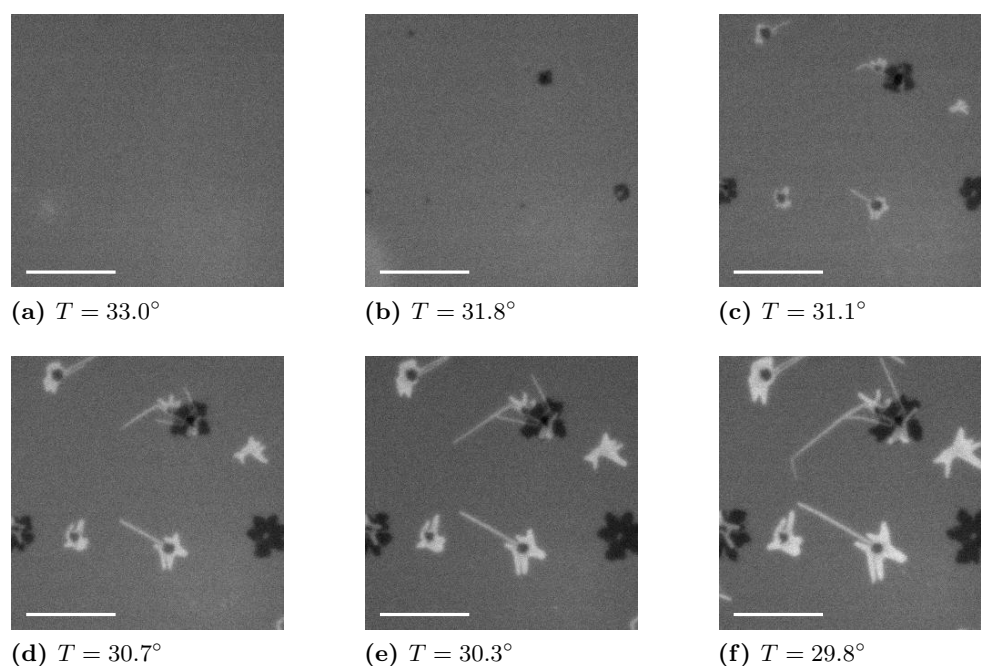**Figure 6.16:** *Growth of stripe phase domains in DLPC / DPPC 1:1 SLBs. 20µm scale bars inserted.*

6.8 Rate of growth for ripple domains

In colaboration with Uffe Bernchou, the growth of stripe domains were examined. A SLB composed of an equimolar mixture of DLPC and DPPC were prepared using spincoating. The sample were hydrated with buffer and afterwards equilibrated at a temperature of $55°C$ for half an hour. After equilibration the sample were flushed with additional buffer for removing all lipid bilayers except for the two layers closest to the solid support. At this time the sample were cooled at the rate $0.7°C/min$ until a temperature of $25°C$ were reached. During the cooling sequence several fluorescence images were acquired, six of these images are shown in figure 6.16. During cooling the following were observed: at $31.8°C$ gel domains are formed in both lipid bilayers, at $31.1°C$ brighter stripe domains are formed, these domains continues to grow throughout the image sequence. In the image sequence there are two distinct bright domains, a thin and rapid growing type and a more dense and slowly growing type. For quantifying the growth velocity of the different types, a Matlab program (described in section 4.3) have been developed. The program first locates end points of ripple domains and thereafter track the end points through the time sequence. For each tracked end point it was now possible to plot the grown distance as a function of time; for each particle the
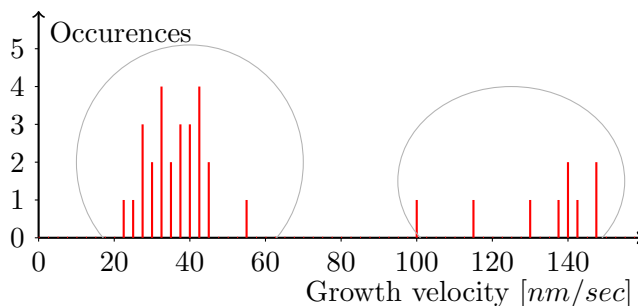
Figure 6.17: *Histogram of growth speed for ripple domains in DLPC / DPPC (1:1) lipid bilayers.*

growth velocity could now be determined by fitting a first order polynomial to the time and grown distance values. In figure 6.17 the determined growth velocities are plotted in a histogram. The main part of the tracked domains grew at a rate centered around $35nm/s$, the rest of the tracked domains grew much faster with rates above $100nm/s$.

The surface structure of the thin and thick stripe domains were examined using AFM, the findings are visualized in figure 6.18. The AFM images revealed that the molecular structure of the thin and thick stripe domains were different. The ripple repeat distance in the thin stripes were $13.5 \pm 0.2nm$ and the similar value for the thick stripes were $27.4 \pm 0.6nm$. By comparing these values to the known ripple repeat distances determined by Kaasgaard *et. al* [74], the membrane phase of the thin stripes were determined to be the stable ripple phase and the thick stripes were in the metastable ripple phase.

6.9   Summary

Domain formation during cooling of SLBs were monitored using fluorescence microscopy. Stripe domains were only observed in lipid bilayer closest to the solid support if the bilayer contained anionic lipids. The orientation of DiI, which has been used as fluorophore in the conducted experiments, can be measured using linearly polarized light and afterwards analyze the acquired images using the method based on Fourier analysis described in section 5.4. The use of mica as solid support in samples that should be examined with linearly polarized light can cause problems; two different distortions caused by the birefringent properties of mica were observed during the experiments.

(a) *Scale bar: 10µm*
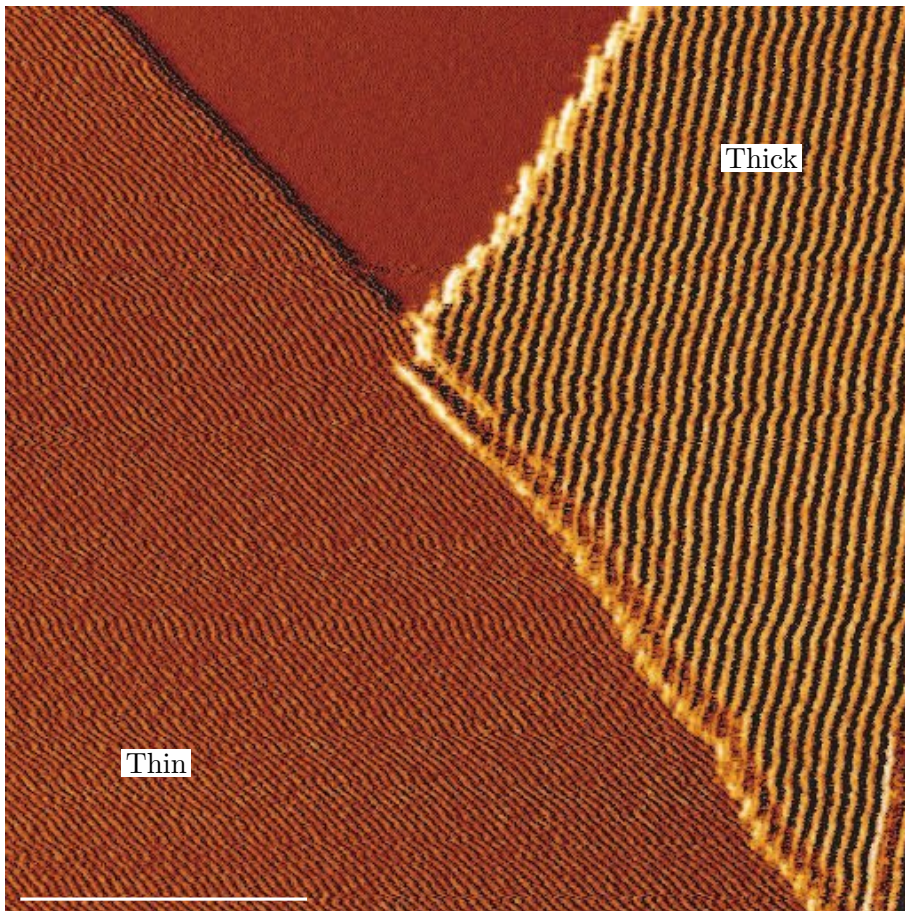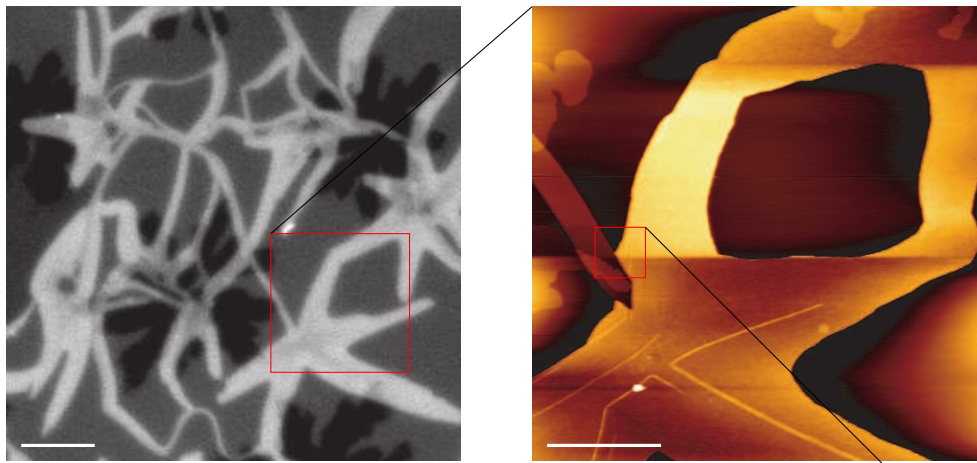
(b) *Scale bar: 5µm*

(c) *Scale bar: 500nm*

Figure 6.18: *Thin and thick stripe domain structure visualized by AFM.*

Chapter 7

Conclusion

The aim of the present thesis is to process and extract information from images obtained with fluorescence microscopy. Linearly polarized light has been used for measuring how fluorophores are aligned in gel and stripe domains. Images have been acquired with both one and two photon excitation. The two photon microscope were used for examining gel domains in an equimolar mixtures of DOPC and DPPC. The lipid bilayers were stained with the fluorophore Laurdan. In the examined gel domains, the fluorophore orientation divided the gel domain into several sub domains. Each sub domain contained similar aligned fluorophores. Analysis of the observed variations in fluorescence intensity, as the polarization orientation were changed, revealed a higher bound on the width of the fluorophore orientation distribution. The observed fluorescence variations can only be generated if the fluorophore distribution is more narrow than $\sim \pm 30°$. From a sequence of images acquired by varying the polarization orientation, the fluorophore orientation can efficiently be calculated using Fourier analysis. The obtained information from the Fourier analysis can be visualized using a suitable mapping to the Hue, Saturation and Value color model. How measurement uncertainties (photon statistics) affects the uncertainty of the determined fluorophore orientation were examined using Monte Carlo simulations. The simulations revealed a power law relation between the number of acquired images N, the signal strength S and the uncertainty in the determined fluorophore orientation σ. The found relation were $\sigma \sim \frac{53°}{\sqrt{NS}}$. Analysis of the determined fluorophore orientations inside one of the sub domains revealed a normal distributed fluorophore orientation distribution with standard deviation $\sigma = 8.3°$. This value is significantly higher than the uncertainty estimated by the Monte Carlo simulations for the used experimental conditions, $\sigma \sim 2.7°$. This difference indicates that the fluorophores in the analyzed area are not perfectly aligned.

Using one photon polarization microscopy, it was investigated how the fluorophore DiI_{C18} were aligned inside fluid, gel and stripe domains. Binary lipid mixtures consisting of DPPC / POPC, DPPC / POPG, DPPG / POPC and

DPPG / POPG were analyzed. In general the observed fluorophore anisotropy was low (effectively zero) for fluid domains but were significant for both gel and stripe domains. The conducted experiments revealed that the fluorophore orientation in gel domains divides the domain into a few (approximately six) sub domains. The high fluorophore anisotropy of stripe domains indicates that the fluorophores are well aligned inside this phase. It was found that the transition dipole of DiI is orientated along the stripes. The analysis of the fluorophore orientation in stripe domains revealed some systematic errors in the determined fluorophore orientation. Control experiments conducted with supported lipid bilayers on a glass support did not have these systematic errors, this increased the suspicion that the material used as solid support, mica, could influence the polarization state of light. Through the literature it was found that mica is a birefringent material. Calculations of how polarized light is transmitted through a slice of mica indicated that the birefringent properties of mica could explain the observed systematic errors. The thickness of the slice of mica used as solid support determined which kind of error that were present in the acquired images. In some samples it was now possible to correct for these systematic errors. The remaining samples, in which the orientation analysis had only found two distinct and orthogonal orientations, did not contain enough information to determine the fluorophore orientation; that this information were newer acquired could also be explained due to the birefringent properties of mica.

Preparation of samples for the one photon polarization fluorescence microscopy studies includes cooling of the sample from above the main transition temperature, to a temperature deep in the gel / fluid phase coexistence region. During the cooling of the sample, the temperature at which specific membrane phases nucleated were recorded. In all the examined binary lipid mixtures the formation of gel domains in the first lipid bilayer were observed. In two of the examined lipid mixtures, DPPC / POPG and DPPG / POPC, the formation of stripe domains in the *first* lipid bilayer was observed. The mixture of DPPG / POPG was not able to produce stripes, instead it formed round bright domains around the previously formed gel domains. The DPPC / POPC mixtures which were unable to form stripe domains in the first bilayer were able to form stripe domains in the subsequent bilayers.

Appendix A

Expected polarization dependence

The polarization response for a fluorophore with a fixed orientation θ_0 can be expressed like

$$F(\theta) = I_0 \cos(\theta - \theta_0)^2$$

for one photon excitation. If the fluorophore orientation is not constant but fluctuates around θ_0 with a standard deviation of σ how will the expected polarization response then be? In the following $E\left[f(\varepsilon)\right]$ denotes the expected value of the function $f(\varepsilon)$ when ε is normal distributed with zero mean and standard deviation σ.

$$E\left[F(\theta)\right] = E\left[I_0 \cos(\theta - \theta_0 - \varepsilon)^2\right]$$

$$= E\left[I_0\left(\frac{1}{2} + \frac{1}{2}\cos(2\theta - 2\theta_0 - 2\varepsilon)\right)\right]$$

Using the relation $\cos(A+B) = \cos(A)\cos(B) - \sin(A)\sin(B)$ the variable ε have been isolated from the other orientation variables θ and θ_0.

$$E\left[F(\theta)\right] = E\left[I_0\left(\frac{1}{2} + \frac{1}{2}\cos(2\theta - 2\theta_0)\cos(2\varepsilon) - \sin(2\theta - 2\theta_0)\sin(2\varepsilon)\right)\right]$$

then factors that are independent on ε have been moved outside the expectation value.

$$E\left[F(\theta)\right] = \frac{I_0}{2} + \frac{I_0}{2}\cos(2\theta - 2\theta_0)E\left[\cos(2\varepsilon)\right] - \frac{I_0}{2}\sin(2\theta - 2\theta_0)E\left[\sin(2\varepsilon)\right]$$

$$\text{(A.1)}$$

Before we can continue, the expected value of $\cos(\varepsilon)$ and $\sin(\varepsilon)$ must be determined. The expected value of the function $f(\varepsilon)$, were ε is taken from a random distribution with the probability density function $p(\varepsilon)$, is defined as

$$E\left[f(\varepsilon)\right] = \int_{-\infty}^{\infty} f(\varepsilon)p(\varepsilon)d\varepsilon$$

A. Expected polarization dependence

The expected value of the sine function of a random variable drawn from a normal distribution with zero mean will then be

$$E\left[\sin(\varepsilon)\right] = \int_{-\infty}^{\infty} \sin(\varepsilon) \frac{1}{\sigma\sqrt{2\pi}} \exp\left(\frac{-\varepsilon^2}{2\sigma^2}\right) d\varepsilon = 0$$

As the integral of an odd function over a symetric interval is zero, the expected value of $\sin(\varepsilon)$ will also be zero. The expected value of the cosine function is not zero and some math are required for the calculations.

$$E\left[\cos(\varepsilon)\right] = \int_{-\infty}^{\infty} \cos(\varepsilon) p(\varepsilon) d\varepsilon$$

The cosine function is replaced by the corresponding tayler expansion

$$= \int_{-\infty}^{\infty} \sum_{m=0}^{\infty} \frac{(-1)^m \varepsilon^{2m}}{(2m)!} p(\varepsilon) d\varepsilon$$

$$= \sum_{m=0}^{\infty} \frac{(-1)^m}{(2m)!} \int_{-\infty}^{\infty} \varepsilon^{2m} p(\varepsilon) d\varepsilon$$

The integral is the even central moments of the normal distribution, which have the value[82]:
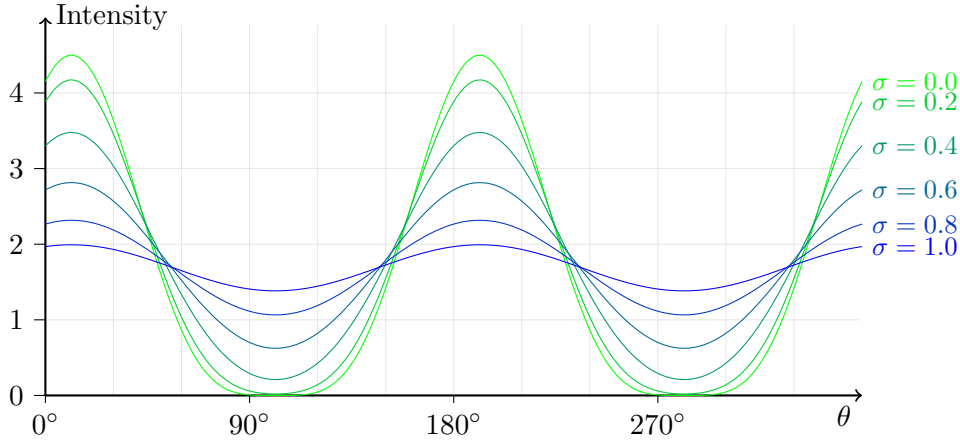
$$\int_{-\infty}^{\infty} \varepsilon^{2m} p(\varepsilon) d\varepsilon = \frac{(2m)!}{2^m m!} \sigma^{2m}$$

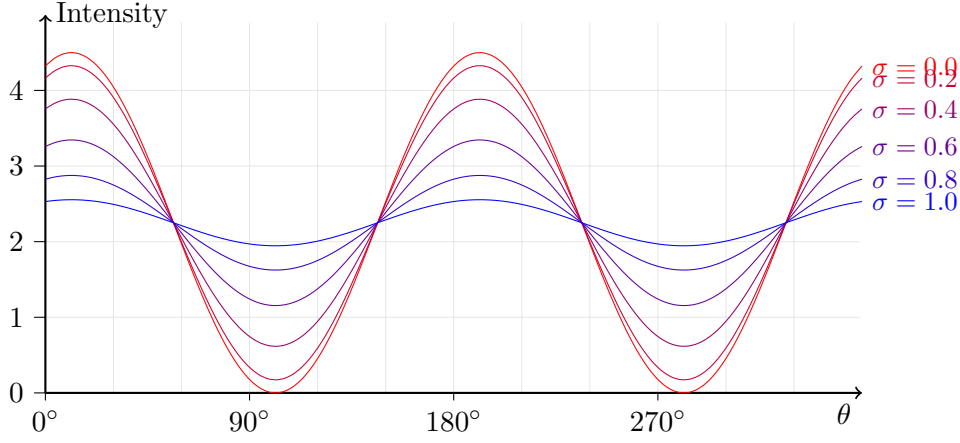Using this expression we can continue the derivation of the expected cosine value

$$E\left[\cos(\varepsilon)\right] = \sum_{m=0}^{\infty} \frac{(-1)^m}{(2m)!} \frac{(2m)!}{2^m m!} \sigma^{2m}$$

$$= \sum_{m=0}^{\infty} \frac{1}{m!} \left(\frac{-\sigma^2}{2}\right)^m$$

$$= \exp\left(-\sigma^2/2\right)$$

We can now continue on the derivation of $E\left[F(\theta)\right]$. The expected value of the sine and cosine functions have been inserted in A.1 which yields

$$E\left[F(\theta)\right] = \frac{I_0}{2} + \frac{I_0}{2}\cos(2\theta - 2\theta_0) \cdot \exp\left(-(2\sigma)^2/2\right) - \frac{I_0}{2}\sin(2\theta - 2\theta_0) \cdot 0$$

$$= \frac{I_0}{2} + \frac{I_0}{2}\cos(2\theta - 2\theta_0) \cdot \exp\left(-2\sigma^2\right) \tag{A.2}$$

(a) *Expected two photon polarization response*

(b) *Expected two photon polarization response*

Figure A.1: *Expected polarization response*

For two photon excitation the similar expression will be

$$
\begin{aligned}
E\left[G(\theta)\right] &= I_0 \cos(\theta - \theta_0 - \varepsilon)^4 \\
&= I_0 \left(\frac{3}{8} + \frac{1}{2}\cos(2\theta - 2\theta_0 - 2\varepsilon) + \frac{1}{8}\cos(4\theta - 4\theta_0 - 4\varepsilon) \right) \\
&= \frac{3I_0}{8} + \frac{I_0}{2}\cos(2\theta - 2\theta_0) \cdot \exp\left(-2\sigma^2\right) \\
&\qquad + \frac{I_0}{8}\cos(4\theta - 4\theta_0) \cdot \exp\left(-8\sigma^2\right)
\end{aligned}
\tag{A.3}
$$

The dependence of the sigma value is visualized in figure A.1.

Bibliography

[1] (2009-03-14). URL `http://en.wikipedia.org/wiki/File:Animal_cell_structure_en.svg`.

[2] (2009-03-14). URL `http://commons.wikimedia.org/wiki/File:Popc_details.svg`.

[3] Mueller, P., Rudin, D. O., Tien, H. T. & Wescott, W. C. Reconstitution of excitable cell membrane structure in vitro. *Circulation* **26**, 1167–1171 (1962).

[4] Bangham, A. D. & Horne, R. W. Negative staining of phospholipids and their structural modification by surface active agents as observed in the electron microscope. *Journal of Molecular Biology* **8**, 660–668 (1964).

[5] Lipid (2009). URL `http://en.wikipedia.org/wiki/Lipid`.

[6] Gray, G. M. & Yardley, H. J. Lipid compositions of cells isolated from pig, human, and rat epidermis. *J Lipid Res* **16**, 434–440 (1975).

[7] Evans, D. F. & Wennerström, H. *The colloidal domain* (Wiley-VCH, 1999), second edition edn.

[8] Ipsen, J. H., Karlström, G., Mourtisen, O., Wennerström, H. & Zuckermann, M. Phase equilibria in the phosphatidylcholine-cholesterol system. *Biochimica et Biophysica Acta (BBA) - Biomembranes* **905**, 162 – 172 (1987).

[9] Mouritsen, O. G. *Life - as a matter of fat* (Springer-Verlag, 2005).

[10] Wack, D. C. & Webb, W. W. Synchrotron x-ray study of the modulated lamellar phase $p_{\beta'}$ in the lecithin-water system. *Phys. Rev. A* **40**, 2712–2730 (1989).

[11] Chen, S. C. & Sturtevant, J. M. Thermotropic behavior of bilayers formed from mixed-chain phosphatidylcholines. *Biochemistry* **20**, 713–718 (1981).

[12] Berg, J. M., Tymoczko, J. L. & Stryer, L. *Biochemistry* (W. H. Freeman and Company, 2007), sixth edn.

[13] Mabrey, S. & Sturtevant, J. M. Investigation of phase transitions of lipids and lipid mixtures by sensitivity differential scanning calorimetry. *Proc Natl Acad Sci U S A* **73**, 3862–3866 (1976).

[14] Heimburg, T. *Thermal Biophysics of Membranes* (Wiley–VCH, 2007). URL `http://eu.wiley.com/WileyCDA/WileyTitle/productCd-3527404716.html`.

[15] Clerc, S. G. & Thompson, T. E. Permeability of dimyristoyl phosphatidylcholine/dipalmitoyl phosphatidylcholine bilayer membranes with coexisting gel and liquid-crystalline phases. *Biophysical Journal* **68**, 2333–2341 (1995).

[16] Sinensky, M. Homeoviscous adaptation–a homeostatic process that regulates the viscosity of membrane lipids in escherichia coli. *Proceedings of the National Academy of Sciences of the United States of America* **71**, 522–525 (1974).

[17] Fidorra, M., Duelund, L., Leidy, C., Simonsen, A. C. & Bagatolli, L. A. Absence of fluid-ordered/fluid-disordered phase coexistence in ceramide/popc mixtures containing cholesterol. *Biophys J* **90**, 4437–4451 (2006).

[18] Singer, S. J. & Nicolson, G. L. The fluid mosaic model of the structure of cell membranes. *Science* **175**, 720–731 (1972).

[19] Simons, K. & Ikonen, E. Functional rafts in cell membranes. *Nature* **387**, 569–572 (1997).

[20] Gombos, I., Steinbach, G., Pomozi, I., Balogh, A., Vámosi, G., Gansen, A., László, G., Garab, G. & Matkó, J. Some new faces of membrane microdomains: a complex confocal fluorescence, differential polarization, and fcs imaging study on live immune cells. *Cytometry A* **73**, 220–229 (2008).

[21] Anderson, R. G. W. & Jacobson, K. A Role for Lipid Shells in Targeting Proteins to Caveolae, Rafts, and Other Lipid Domains. *Science* **296**, 1821–1825 (2002).

[22] Bagatolli, L. A. & Gratton, E. Two photon fluorescence microscopy of coexisting lipid domains in giant unilamellar vesicles of binary phospholipid mixtures. *Biophys J* **78**, 290–305 (2000).

[23] Simonsen, A. C. *Handbook of Modern Biophysics*, chap. Spatiotemporal organization of spin-coated supported model membranes, 141–170 (Springer, 2009).

[24] Müller, D. J., Amrein, M. & Engel, A. Adsorption of biological molecules to a solid support for scanning probe microscopy. *J Struct Biol* **119**, 172–188 (1997).

[25] Özder, S., Köysal, O., San, S. E. & Ecevit, F. N. Determination of the refractive index dispersion of thick films by continuous wavelet transform. *Thin Solid Films* **458**, 257 – 262 (2004).

[26] Simonsen, A. C. Activation of phospholipase a2 by ternary model membranes. *Biophys J* **94**, 3966–3975 (2008).

[27] Langmuir, I. The constitution and fundamental properties of solids and liquids. ii. liquids.1. *Journal of the American Chemical Society* **39**, 1848–1906 (1917).

[28] Blodgett, K. B. Films built by depositing successive monomolecular layers on a solid surface. *Journal of the American Chemical Society* **57**, 1007–1022 (1935).

[29] Brian, A. A. & McConnell, H. M. Allogeneic stimulation of cytotoxic t cells by supported planar membranes. *Proc Natl Acad Sci U S A* **81**, 6159–6163 (1984).

[30] Richter, R. P., Bérat, R. & Brisson, A. R. Formation of solid-supported lipid bilayers: an integrated view. *Langmuir* **22**, 3497–3505 (2006).

[31] Simonsen, A. C. & Bagatolli, L. A. Structure of spin-coated lipid films and domain formation in supported membranes formed by hydration. *Langmuir* **20**, 9720–9728 (2004).

[32] Mennicke, U. & Salditt, T. Preparation of solid-supported lipid bilayers by spin-coating. *Langmuir* **18**, 8172–8177 (2002).

[33] Meyerhofer, D. Characteristics of resist films produced by spinning. *Journal of Applied Physics* **49**, 3993–3997 (1978).

[34] Yang, J. & Appleyard, J. The main phase transition of mica-supported phosphatidylcholine membranes. *The Journal of Physical Chemistry B* **104**, 8097–8100 (2000).

[35] (2007). URL `http://www.fz-juelich.de/inb/inb-1/Two-Photon_Microscopy/`.

[36] Göppert-Mayer, M. über elementarakte mit zwei quantensprüngen. *Annalen der Physik* **401**, 273–294 (1931).

[37] Abella, I. D. Optical double-photon absorption in cesium vapor. *Phys. Rev. Lett.* **9**, 453–455 (1962).

[38] Axelrod, D. Carbocyanine dye orientation in red cell membrane studied by microscopic fluorescence polarization. *Biophys J* **26**, 557–573 (1979).

[39] Gullapalli, R. R., Demirel, M. C. & Butler, P. J. Molecular dynamics simulations of dii-c18(3) in a dppc lipid bilayer. *Phys Chem Chem Phys* **10**, 3548–3560 (2008).

[40] Stevens, B. C. & Ha, T. Discrete and heterogeneous rotational dynamics of single membrane probe dyes in gel phase supported lipid bilayer. *J Chem Phys* **120**, 3030–3039 (2004).

[41] Invitrogen. Product spectra - dii/lipid (2009-03-09). URL http://www.invitrogen.com/site/us/en/home/support/Product-Technical-Resources/Product-Spectra.282lip.html.

[42] Klausner, R. D. & Wolf, D. E. Selectivity of fluorescent lipid analogues for lipid domains. *Biochemistry. 1980 Dec 23;19(26):6199-203.*. **19**, 6199–6203 (1980).

[43] Sanchez, S. A., Tricerri, M. A., Gunther, G. & E. Gratton, E. Laurdan generalized polarization: from cuvette to microscope. *Modern Research and Educational Topics in Microscopy* 1007 (2007).

[44] Murphy, D. B. *Fundamentals of Light microscopy and Electronic imaging* (Wiley–LISS, 2001).

[45] Binnig, Quate & Gerber. Atomic force microscope. *Phys Rev Lett* **56**, 930–933 (1986).

[46] Leidy, C., Kaasgaard, T., Crowe, J. H., Mouritsen, O. G. & Jorgensen, K. Ripples and the formation of anisotropic lipid domains: Imaging two-component supported double bilayers by atomic force microscopy. *Biophys. J.* **83**, 2625–2633 (2002).

[47] Magonov, S. N. & Whangbo, M.-H. *Surface Analysis with STM and AFM* (VCH, 1996).

[48] Villarrubia, J. S. Algorithms for scanned probe microscope image simulation, surface reconstruction, and tip estimation. *J Res Natl Inst Stand Technol* **102**, 102–425 (1997).

[49] Tada, K., Goto, M., Tamai, N., Matsuki, H. & Kaneshina, S. Thermotropic and barotropic phase transitions of dilauroylphosphatidylcholine bilayer. *Chem Phys Lipids* **153**, 138–143 (2008).

[50] Kaneshina, S., Ichimori, H., Hata, T. & Matsuki, H. Barotropic phase transitions of dioleoylphosphatidylcholine and stearoyl-oleoylphosphatidylcholine bilayer membranes. *Biochimica et Biophysica Acta (BBA) - Biomembranes* **1374**, 1 − 8 (1998).

[51] Wiedmann, T., Salmon, A. & Wong, V. Phase behavior of mixtures of dppc and popg. *Biochim Biophys Acta* **1167**, 114–120 (1993).

[52] Severcan, F. & Dorohoi, D.-O. Ftir studies of temperature influence on the dppg model membrane. *Journal of Molecular Structure* **887**, 117 – 121 (2008).

[53] Ceppi, P., Colombo, S., Francolini, M., Raimondo, F., Borgese, N. & Masserini, M. Two tail-anchored protein variants, differing in transmembrane domain length and intracellular sorting, interact differently with lipids. *Proc Natl Acad Sci U S A* **102**, 16269–16274 (2005).

[54] Rochford, K. *Encyclopedia of Physical Science and Technology, Third Edition, Volume 12*, chap. Polarization and Polarimetry (Academic Press, 2001).

[55] Reitz, J. R., Milford, F. J. & Christy, R. W. *Foundations of electromagnetic theory* (Addison-Wesley, 1993), fourth edition edn.

[56] Dougherty, E. R. *An Introduction to Morphological Image Processing* (SPIE Optical Engineering Press, 1992).

[57] Soille, P. *Morphological Image Analysis* (Springer, 2003), second edn.

[58] Nagle, J. F. & Tristram-Nagle, S. Structure of lipid bilayers. *Biochim Biophys Acta* **1469**, 159–195 (2000).

[59] Bagatolli, L. A. To see or not to see: lateral organization of biological membranes and fluorescence microscopy. *Biochim Biophys Acta* **1758**, 1541–1556 (2006).

[60] Gaus, K., Gratton, E., Kable, E. P. W., Jones, A. S., Gelissen, I., Kritharides, L. & Jessup, W. Visualizing lipid structure and raft domains in living cells with two-photon microscopy. *Proc Natl Acad Sci U S A* **100**, 15554–15559 (2003).

[61] Katsaras, J., Yang, D. S. & Epand, R. M. Fatty-acid chain tilt angles and directions in dipalmitoyl phosphatidylcholine bilayers. *Biophys J* **63**, 1170–1175 (1992).

[62] Parasassi, T., Gratton, E., Yu, W. M., Wilson, P. & Levi, M. Two-photon fluorescence microscopy of laurdan generalized polarization domains in model and natural membranes. *Biophys J* **72**, 2413–2429 (1997).

[63] Levenberg, K. A method for the solution of certain non-linear problems in least squares. *The Quarterly of Applied Mathematics* **2**, 164–168 (1944).

[64] Marquardt, D. An algorithm for least-squares estimation of nonlinear parameters. *SIAM Journal on Applied Mathematics* **11**, 431–441 (1963).

[65] Fricke, H. The electric capacity of cell suspensions. *Physical review* **21**, 708–709 (1923).

[66] Gorter, E. & Grendel, F. On bimolecular layers of lipoids on the chromocytes of the blood. *The Journal of Experimental Medicine* **41**, 439–443 (1925).

[67] Yguerabide, J. & Stryer, L. Fluorescence spectroscopy of an oriented model membrane. *Proc Natl Acad Sci U S A* **68**, 1217–1221 (1971).

[68] Verkleij, A. J. & Ververgaert, P. H. J. T. The architecture of biological and artificial membranes as visualized by freeze etching. *Annu. Rev. Phys. Chem.* 101–122 (1975).

[69] Janiak, M. J., Small, D. M. & Shipley, G. G. Temperature and compositional dependence of the structure of hydrated dimyristoyl lecithin. *Journal of Biological Chemistry* **254**, 6068–6078 (1979).

[70] Tardieu, A., Luzzati, V. & Reman, F. C. Structure and polymorphism of the hydrocarbon chains of lipids: a study of lecithin-water phases. *Journal of molecular biology* **75**, 711–733 (1973).

[71] Tenchov, B. G., Yao, H. & Hatta, I. Time-resolved x-ray diffraction and calorimetric studies at low scan rates. *Biophysical Journal* **56**, 757–768 (1989).

[72] Woodward & Zasadzinski. Amplitude, wave form, and temperature dependence of bilayer ripples in the p beta ' phase. *Phys Rev E Stat Phys Plasmas Fluids Relat Interdiscip Topics* **53**, R3044–R3047 (1996).

[73] Sengupta, K., Raghunathan, V. A. & Katsaras, J. Structure of the ripple phase of phospholipid multibilayers. *Phys. Rev. E* **68**, 031710 (2003).

[74] Kaasgaard, T., Leidy, C., Crowe, J. H., Mouritsen, O. G. & Jorgensen, K. Temperature-controlled structure and kinetics of ripple phases in one- and two-component supported lipid bilayers. *Biophys. J.* **85**, 350–360 (2003).

[75] Sun, W. J., Tristram-Nagle, S., Suter, R. M. & Nagle, J. F. Structure of the ripple phase in lecithin bilayers. *Proc Natl Acad Sci U S A* **93**, 7008–7012 (1996).

[76] Korlach, J., Schwille, P., Webb, W. W. & Feigenson, G. W. Characterization of lipid bilayer phases by confocal microscopy and fluorescence correlation spectroscopy. *Proc Natl Acad Sci U S A* **96**, 8461–8466 (1999).

[77] Beales, P. A., Gordon, V. D., Zhao, Z., Egelhaaf, S. U. & Poon, W. C. K. Solid-like domains in fluid membranes. *J. Phys.: Condens. Matter* **17**, S3341–S3346 (2005).

[78] Li, L. & Cheng, J.-X. Coexisting stripe- and patch-shaped domains in giant unilamellar vesicles. *Biochemistry* **45**, 11819–11826 (2006).

[79] Scott, H. L. Modeling the lipid component of membranes. *Current Opinion in Structural Biology* **12**, 495 – 502 (2002).

[80] de Vries, A. H., Yefimov, S., Mark, A. E. & Marrink, S. J. Molecular structure of the lecithin ripple phase. *Proc Natl Acad Sci U S A* **102**, 5392–5396 (2005).

[81] Sun, X. & Gezelter, J. D. Dipolar ordering in the ripple phases of molecular-scale models of lipid membranes. *J Phys Chem B* **112**, 1968–1975 (2008).

[82] (2009-03-14). URL `http://en.wikipedia.org/wiki/Normal_distribution`.